André Richter

Laser parameters and performance of Pr^{3+}-doped fluorides operating in the visible spectral region

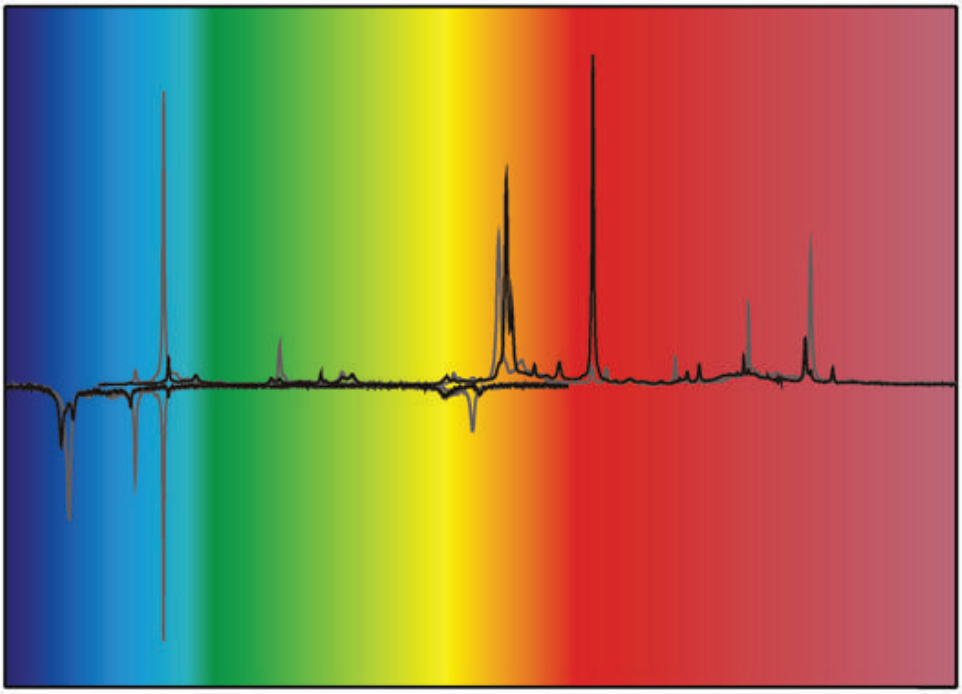

Cuvillier Verlag Göttingen

Laser parameters and performance of Pr^{3+}-doped fluorides operating in the visible spectral region

Dissertation

zur Erlangung des Doktorgrades

des Department Physik

der Universität Hamburg

vorgelegt von
André Richter
aus Hamburg

Hamburg
2008

Bibliografische Information der Deutschen Nationalbibliothek
Die Deutsche Nationalbibliothek verzeichnet diese Publikation in der Deutschen Nationalbibliografie; detaillierte bibliografische Daten sind im Internet über http://dnb.ddb.de abrufbar.
1. Aufl. - Göttingen : Cuvillier, 2008
Zugl.: Hamburg, Univ., Diss., 2008

978-3-86727-584-2

Gutachter der Dissertation:	Prof. Dr. G. Huber
	Prof. Dr. M. Tonelli
Gutachter der Disputation:	Prof. Dr. G. Huber
	Prof. Dr. K. Sengstock
Datum der Disputation:	02.04.2008
Vorsitzender des Prüfungsausschusses:	Dr. K. Petermann
Vorsitzender des Promotionsausschusses:	Prof. Dr. J. Bartels
Dekan der Fakultät für Mathematik, Informatik und Naturwissenschaften:	Prof. Dr. A. Frühwald

Nonnenstieg 8, 37075 Göttingen
Telefon: 0551-54724-0
Telefax: 0551-54724-21
www.cuvillier.de

1. Auflage, 2008
Gedruckt auf säurefreiem Papier

978-3-86727-584-2

Abstract

André Richter: *Laser parameters and performance of Pr^{3+}-doped fluorides operating in the visible spectral region*

This work deals with the fabrication and characterization of the Pr^{3+}-doped fluoride crystals $LiYF_4$, $LiLuF_4$, BaY_2F_8, and KY_3F_{10}. The crystals were grown by the Czochralski method in the facilities in Hamburg and Pisa and feature optical quality sufficient for efficient laser oscillation. First steps of optimization of the growth facility in Hamburg were performed successfully in the framework of this thesis.
Room temperature optical spectroscopy revealed efficient cross-relaxations between the dopant ions in all investigated fluoride materials. Modelling of the decay curves of the $^3P_0$ energy state discovered a mixture of exchange induced and dipole-dipole induced interactions resulting in fast quenching processes. Typical interaction distances were estimated to be 9 Å in case of exchange and 70 Å in case of dipole-dipole interaction.
Detailed low temperature studies of $LiYF_4$ and $LiLuF_4$ revealed more than 5 ion classes. Besides the Pr^{3+}-ions on regular Y^{3+}/Lu^{3+}-sites, a second ion class which is not subject to cross-relaxation processes has been found. It corresponds to an irregular lattice site. Investigations of different dopant concentrations discovered clustering of Pr^{3+}-ions even at low concentration levels. Additionally, Pr^{3+}-ions performing efficient energy transfer were found. These ions contribute strongly to the population of the energy level $^1D_2$ under $^3P_0$-excitation.
Pr^{3+}-laser experiments were performed in continuous wave and Q-switched operation. In continuous wave mode, slope efficiencies of 0.56 were obtained from longitudinally pumped Pr^{3+}-doped fluoridic crystals under optically pumped semiconductor laser excitation. These were the highest slope efficiencies reported for Pr^{3+}-doped fluorides so far. At an absorbed pump power of 1.4 W, laser output powers of 600 mW were obtained in the green and red spectral range, while the orange transition features reduced output powers and efficiencies. From spectroscopic investigations a reabsorption processes at the corresponding laser wavelength could be clearly identified. Intracavity second harmonic generation of the laser radiation at ≈640 nm resulted in generation of continuous wave UV radiation at 320 nm for the first time. Up to 360 mW of UV radiation could be achieved with a conversion efficiency of 0.61 and an overall optical-to-optical efficiency of 0.22. Active Q-switching experiments resulted in pulse energies of ≈60 µJ at pulsewidths of 108 ns. They represent the first reported data of an actively Q-switched Pr^{3+}-laser operated on a visible laser transition.
In the framework of this thesis GaN laser diodes pumping of Pr^{3+}-lasers was demonstrated successfully for the first time. Up to 208 mW of output power and slope efficiencies of 0.46 could be demonstrated at the 640 nm laser transition. In case of Pr^{3+}:$LiYF_4$, about 70 mW in the green, 40 mW in the orange, 185 mW in the red, and 135 mW in the near infrared spectral region were demonstrated for the first time. By intracavity frequency doubling more than 42 mW of UV radiation at 320 nm were obtained from the GaN-based laser diode pumped Pr^{3+}:$LiLuF_4$-laser.

Kurzfassung

André Richter: *Laserparameter und -charakterisierung Pr^{3+}-dotierter Fluoride im sichtbaren Spektralbereich*

Die Arbeit beschäftigt sich mit der Herstellung und Charakterisierung Pr^{3+}-dotierter $LiYF_4$-, $LiLuF_4$-, BaY_2F_8- und KY_3F_{10}-Kristalle. Diese wurden nach der Czochralski-Methode in Hamburg und Pisa hergestellt und wiesen eine für Laserexperimente ausreichende optische Qualität auf. Erste Optimierungsschritte der Kristallzuchtanlage in Hamburg wurden im Rahmen dieser Arbeit erfolgreich durchgeführt.
Spektroskopische Untersuchungen bei Raumtemperatur weisen auf effiziente Kreuzrelaxationsprozesse zwischen den Pr^{3+}-Ionen hin. Unter der Annahme, dass der Energietransfer sowohl auf dipol-dipol Wechselwirkung als auch auf Austauschwechselwirkung basiert, konnten die effektiven Wechselwirkungsreichweiten abgeschätzt werden. Diese belaufen sich auf 9 Å im Falle der Austauschwechselwirkung und 70 Å im Falle der elektrostatischen Wechselwirkung.
Im Rahmen detailierter Tieftemperaturuntersuchungen an $LiYF_4$ und $LiLuF_4$ wurden mehr als 5 Ionenklassen entdeckt. Neben dem regulären wurde ein weiterer Gitterplatz gefunden, auf dem Pr^{3+}-Ionen bei 10 K keine Kreuzrelaxationen zeigen. Dieser weist jedoch eine gestörte Symmetrie auf. Messungen an Konzentrationsreihen deuten auf Clustereffekte für Ionen auf diesem Gitterplatz selbst bei geringen Konzentrationen hin. Eine weitere Klasse von Pr^{3+}-Ionen, zwischen denen effizienter Energieaustausch stattfindet, konnte nachgewiesen werden. Diese trägt zur Besetzung des $^1D_2$-Zustandes unter $^3P_0$-Anregung bei.
Laserexperimente wurden im Dauerstrich- und gütegeschalteten Betrieb durchgeführt. Im Dauerstrichbetrieb konnten differentielle Wirkungsgrade von bis zu 0.56 unter Anregung mit einem optisch gepumpten Halbleiterlaser erzielt werden. Diese stellen die höchsten erreichten Wirkungsgrade direkt gepumpter Pr^{3+}-dotierter Fluoride dar. Bei einer absorbierten Leistung von 1,4 W konnten auf den Laserübergängen im grünen und roten Spektralbereich bis zu 600 mW erreicht werden, wogegen der Übergang im orangefarbenen Spektralbereich eine geringere Effizienz aufwies. Spektroskopische Untersuchungen zeigen einen Reabsorptionsprozess auf dieser Laserwellenlänge. Resonatorinterne Frequenzverdopplung der 640 nm-Strahlung ermöglichte erstmals die Erzeugung von UV-Strahlung im Dauerstrichbetrieb bei 320 nm. Bis zu 360 mW konnten mit einer Konversionseffizienz von 0.61 und einer optisch-zu-optischen Effizienz von 0.22 erzielt werden. Erstmalig durchgeführte Experimente zur aktiven Güteschaltung ergaben für den Laserbetrieb bei 640 nm Pulsenergien von $\approx 60\,\mu J$ bei einer Pulsdauer von 108 ns.
Im Rahmen der Arbeit konnten erstmals auch GaN-Laserdioden erfolgreich zur Anregung von Pr^{3+}-Lasern eingesetzt werden. Für den roten Laserübergang wurden ein differentieller Wirkungsgrad von 0.46 und Ausgangsleistungen von 208 mW erzielt. Im Falle von Pr^{3+}:$LiYF_4$ wurden 70 mW im grünen, 40 mW im orangefarbenen, 185 mW im roten und 135 mW nahen dem infraroten Spektralbereich unter Laserdiodenanregung gezeigt. Mittels resonatorinterner Frequenzverdopplung sind im Dauerstrichbetrieb 42 mW UV-Strahlung bei 320 nm mit einem Pr^{3+}:$LiLuF_4$-Laser erreicht worden.

Contents

1 Introduction

In the beginning of the 20th century, several scienists investigated the nature of light and matter as well as the interaction between these two fundamental components. With the help of the quantum theory several aspects in this field could be explained in a sufficient way. Based on this theory Einstein predicted the realization of lasers[1] in 1916 [Ein16]. However, it was more than 40 years later when Maiman demonstrated laser oscillation for the first time [Mai60]. He used a flashlamp as pump source for a ruby (Cr^{3+}:Al_2O_3) laser rod. Soon afterwards, other transition metal ions as well as rare earth ions were investigated with respect to their laser performance. While the transition metal ions offer a wide laser tunability range of several hundreds of nanometers, the optical transitions of rare earth ions feature spectrally narrow optical transitions. With the development of laser diodes (LDs) of suitable wavelength, highly efficient and compact diode-pumped solid-state lasers (DPSSLs) could be realized.

The trivalent praseodymium ion (Pr^{3+}) offers several transitions in the visible spectral range from blue to near IR. Thus, with Pr^{3+}-lasers operated at visible transitions, it is easy to achieve UV radiation only by a single step of second harmonic generation (SHG), making these lasers interesting for several biotechnological and medical applications. The fundamental radiation in the visible spectral range is interesting for display applications, too. While the first Pr^{3+}-based laser was a flashlamp pumped Pr^{3+}:$CaWO_4$ under cryogenic temperatures [Yar62], Pr^{3+}-lasers to date oscillate at ambient temperatures and the flashlamps are substituted by laser systems. Direct pumping of Pr^{3+}-lasers operating at room temperature was realized with Ar-ion lasers or the radiation obtained by intracavity SHG of a Nd^{3+}:$Y_3Al_5O_{12}$ laser operated at the ground state transition [San94b, Heu99]. These pumping systems did not match the absorption lines of Pr^{3+} well and thus resulted in moderate efficiencies. Furthermore, the pump sources were bulky or complex. Suitable laser diodes based on GaN emitting in the blue spectral region are commercially available since about 2003. Just one year later, a GaN-LD-pumped Pr^{3+}-laser was realized for the first time by our group [Ric04b]. These laser diodes enable quite cheap and compact laser set-ups as well as improved efficiencies. A second option for even higher efficiencies are frequency doubled optically pumped semiconductor lasers (OPSLs) operating at suitable wavelengths.
This work deals with the fabrication, spectroscopic investigations and laser performance of Pr^{3+}-doped fluoride single crystals. The first chapter deals with the crystal growth process by the method of Czochralski. Besides the discussion of the challenges of crystal growing, detailed physical properties of the fluoride materials will be given herein. The

[1] LASER: light amplification by stimulated emission of radiation

next chapter focuses on the spectroscopic investigations performed both at room temperature and cryogenic temperatures of 10 K. Different mechanisms regarding microscopic energy transfer between adjacent Pr^{3+}-ions will be discussed and evaluated. The last chapter contains the results of the performed laser experiments. The Pr^{3+}-laser performance under OPSL-pumping and GaN-LD pumping will be presented both in continuous wave and Q-switch mode. Furthermore, the experiments and results from intracavity second harmonic generation will be discussed. To conclude, a summary and an outlook will be given.

2 Crystal Growth

This chapter focuses on the crystal growth of Pr^{3+}-doped fluoride single crystals. In Section 2.1 the growth process and the Czochralski growth setup used in this work is described while structural and optical properties of the crystalline materials will be presented in Section 2.2. Afterwards, some challenges which occurred during the crystal growth process will be highlighted and possible solutions will be discussed in Section 2.3. Finally, a summary will be given in Section 2.4. Further details of the Czochralski growth process can be found in the book by Wilke and Bohm [Wil88].

2.1 The Crystal Growth Procedure

Weighting and Prefluorination

In the beginning of the crystal growth procedure, the raw materials, usually 4N or 5N fluoride powders, are weighted according to the stoichiometry of the crystalline material and subsequently mixed in ambient atmosphere. This mixture is treated by a pre-fluorination process.

Using prefluorinated materials has several advantages. First of all, the amount of oxygen impurities is reduced significantly. Secondly, the mixed powders have already reacted and exhibit a polycrystalline structure of the desired material. Thus improved handling conditions are achieved in this way, because the desired structures are generally not hygroscopic in contrast to some of the starting materials like potassium fluoride (KF). And at last, the surface-to-volume ratio is reduced leading to a smaller amount of contaminations during the following steps. Thus, an increased crystal quality can be expected.

The pre-fluorination process takes place in a set-up consisting of two connected furnaces. A bowl made of glassy carbon and filled with the mixed powders is placed in the main furnace, while the auxiliary furnace contains a crucible filled with 12 g of potassium hydrogen fluoride (KHF_2). The main furnace is evacuated to $5{\cdot}10^{-2}$ mbar and subsequently filled with a 5N nitrogen atmosphere. Finally a constant gas flow of N_2 of 6 l/h is set. This gas flows from the inlet through the auxiliary furnace, the main furnace and through an aqueous solution of sodium hydroxide. Then, the main furnace is heated up to the melting point of the desired crystalline material and the auxiliary furnace slightly below the decomposition temperature of KHF_2 of about 400°C. When the main furnace temperature reaches the melting point, the auxiliary furnace is heated up slightly above 430°C. Now, KHF_2 decomposes according to

$$\mathrm{KHF_{2(s)}} \rightarrow \mathrm{KF_{(s)}} + \mathrm{HF} \uparrow \tag{2.1}$$

and HF gas is produced. The gas is transported by the nitrogen gas flow into the main furnace and reacts with any metal oxide (M_2O, MO, M_2O_3) compounds within the melt forming the corresponding fluoride compounds and water, that is for example:

$$M_2O + 2HF \rightarrow 2MF + H_2O \tag{2.2}$$

In an aqueous solution of sodium hydroxide the excess HF molecules are neutralized as follows:

$$HF_{(g)} + NaOH_{(aq)} \rightarrow NaF_{(aq)} + H_2O \tag{2.3}$$

After 4 hours the prefluorination process is terminated, both furnaces are cooled down to ambient temperatures and the prefluorinated materials are removed from the furnace.

Crystal Growth

After the pre-fluorination process, the crystal growth process can be started. Figure 2.1 shows the setup used for growing fluoride single crystals by the Czochralski method. It consists of a conical crucible with 35 mm outer diameter and 38 mm in height, placed in a larger crucible (49 mm in height, 50 mm in diameter), which is filled with 2-mm diameter pellets for thermal insulation. The crucibles and the pellets are made of glassy carbon. This crucible system is mounted on a carbon-made pedestal. A carbon heat shield placed on top of the inner crucible completes the growth setup. The RF-coil surrounding the crucibles provides the power for heating the outer and inner crucible as well as the materials in the inner crucible. Due to the weak electric conductivity of carbon ($\sigma_C = 1.28 \times 10^5$ S/m, [ECTI]) the skin depth is $\delta \approx 3.8$ mm and the RF field is not significantly reduced by the 1.85 mm thick walls of the outer crucible. The remaining RF power is coupled into the inner crucible and heats the materials inside. A nickel wire is used as seed.

Prior to each growth run, the furnace with the prepared growth setup is evacuated to $6 \cdot 10^{-2}$ mbar and filled twice with 5N argon gas slightly above standard atmospheric pressure. This procedure results in an oxygen partial pressure below 10^{-2} mbar. During the crystal growth run, the prepared Argon atmosphere slightly above standard atmospheric pressure remains in the chamber. In the next step, the fluoride materials are heated to the melting point. Then, the seed wire is lowered close to the melt surface to adjust the temperature of the wire. After 20 minutes, the wire, rotating with 9 rpm, is dipped into the melt to initiate the process of crystallization. In case of crystallization, the rotating wire is pulled up with a pulling speed of 0.85 mm/h. The amount of crystallizing material is controlled by manually adjusting the melt temperature. Carbon contaminations on the melt surface induce a locally distorted temperature profile. Because of these conditions,

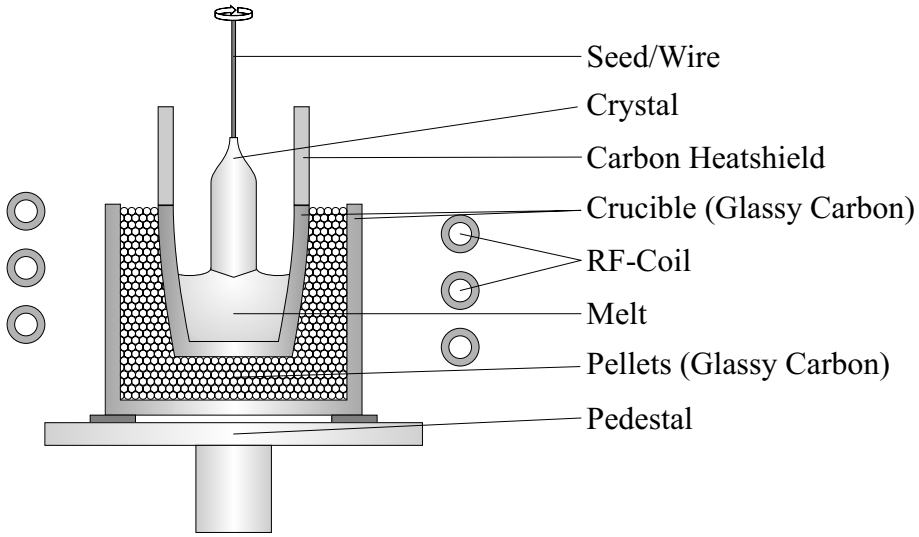

Figure 2.1: Schematic set-up of the Czochralski growth apparatus (modified from [Hen01])

the first part of the grown crystal is polycrystalline and features a large diameter. By increasing the melt temperature, the diameter is reduced until grain selection leads to single crystalline growth. Now the melt temperature is reduced again to increase the diameter, resulting in a bottleneck-shaped structure. When the desired diameter is reached, the thermal conditions are carefully adjusted to obtain a constant diameter of the crystal. After growing a certain amount of material, the growth procedure is stopped by removing the grown crystal from the melt. To reduce thermal stress in the grown crystal, the temperature is reduced slowly. After 4 hours ambient temperature is reached and the growth chamber is evacuated to $6{\cdot}10^{-2}$ mbar and refilled with argon gas once again so that all fluoride compounds existing in the gas phase are removed.

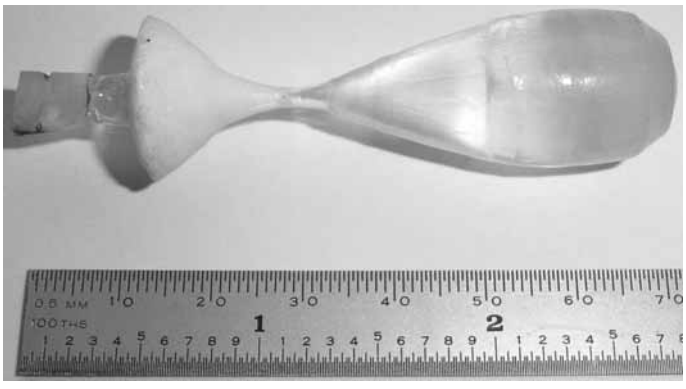

Figure 2.2: As-grown Pr(0.45at.%):$LiLuF_4$-crystal boule

	$LiYF_4$	$LiLuF_4$	BaY_2F_8	KY_3F_{10}
Growth location	Hamburg	Hamburg (Pisa)	Pisa	Hamburg (Pisa)
Initial melt composition (mol%)	LiF-YF_3 53%-47%	LiF-LuF_3 50%-50%	BaF_2-YF_3 33%-67%	KF-YF_3 25%-75%
Melting point T_m(°C)	830	850	960	1030
Melt specification	incongruent	congruent	congruent	congruent
Rotation speed (rpm)	9	9 (5)	5	10 (5)
Pulling speed (mm/h)	0.85	0.85 (1)	0.5	0.85 (1.00)

Table 2.1: Material and growth parameters applied for growing of fluoride crystals by the Czochralski method ([Tho61, Sob82, Har83, Cha93])

Figure 2.2 shows a photograph of a grown Pr^{3+}(0.45at.%):$LiLuF_4$ single crystal. The shape results from the procedure described above.

Table 2.1 shows the melt and growth parameters used for the different growth runs as well as their thermal properties. The BaY_2F_8 crystals were provided by the University of Pisa. Both KY_3F_{10}- and $LiLuF_4$-single crystals were grown in Hamburg as well as in Pisa.

2.2 Crystal Structures

In general, fluoride crystals offer low phonon energies compared to oxide crystals resulting in lower nonradiative decay rates induced by lattice vibrations. Another advantage of fluoride crystals for laser applications is the negative refractive index change with increasing temperature which partially compensates the thermal lensing during high power laser operation and thus partially preserves the beam quality. This section summarizes important properties of the host crystals investigated in the context of this work.

2.2.1 Lithium-Yttrium-Fluoride

Lithium-Yttrium-Fluoride ($LiYF_4$ or YLF) is a well-known fluoride host crystal for laser applications. It is commercially available and can be doped with various rare earth ions. Room temperature laser oscillation of several rare earth ions in this host was demonstrated to date [Ehr79, Gra93, Jen96].

Crystal system	tetragonal
Space group (Schönfließ)	$I4_1/a$ (C_{4h}^6)
Site symmetry of Y^{3+}	S_4
Formula units per unit cell Z	4
Lattice constants (Å)	a = 5.160 c = 10.850
Coefficient of thermal expansion α (K^{-1})	13.3×10^{-6} along $\vec{a}$ 8.3×10^{-6} along $\vec{c}$
Thermal conductivity k (W/(m·K))	6
Refractive indices ($\lambda = 639.5\,\mathrm{nm}$)	$n_o = 1.453$ $n_e = 1.475$
$\frac{\partial n}{\partial T}$ (K^{-1})	-4.3×10^{-6} ($\vec{E} \| \vec{a}$) -2.0×10^{-6} ($\vec{E} \| \vec{c}$)
Effective phonon energy $\hbar\omega_{\mathrm{eff}}$ (cm^{-1})	460
Density ρ (g/cm^3)	3.99
Mohs hardness	4-5

Table 2.2: Structural and optical properties of YLF [Tho61, Sve88, Kam93a, Zha94]

Table 2.2 gives some structural and optical parameters of this fluoride crystal. YLF forms a tetragonal crystal with the $CaWO_4$ (Scheelite)-structure (Space group $I4_1/a$). The unit cell is shown in Figure 2.3(a). Trivalent rare earth dopant ions typically substitute the Y^{3+}-ions in this material. Each Y^{3+}-site is surrounded by 6 fluorine ions forming

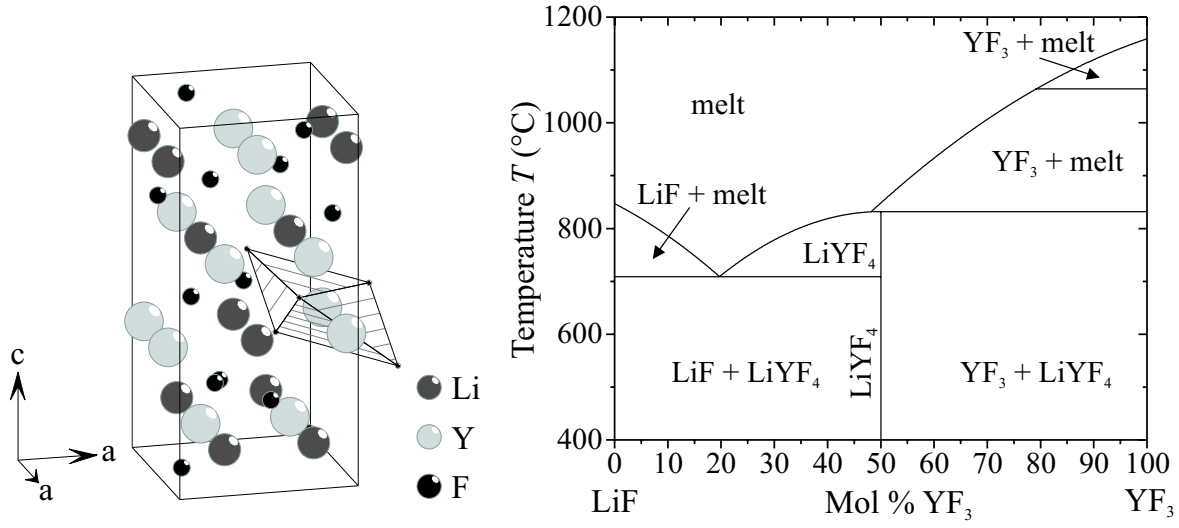

(a) (b)

Figure 2.3: (a) Sketch of the unit cell of YLF with the polyhedron defined by the surrounding fluoride ligands of an Y^{3+}-ion is highlighted [Tho61]. (b) The phase diagram of the binary system LiF-YF_3 [Tho61].

an octahedron. However, Burkhalter mentioned the formation of lattice distortions by microtwinning[1] in undoped YLF single crystals [Bra91, Bur01]. In contrast to a single site for rare earth dopant ions, Barthem reported on Nd^{3+}-ions occupying different sites in this host material observed in low temperature optical measurements [Bar86]. This can be explained by comparing the different ionic radii of the rare earth dopant ions (R_{Pr} = 1.14 Å) and the regular lattice ion Y^{3+} (R_Y = 1.04 Å) [Kam90]. The incorporated rare earth ions induce local stress in the crystal lattice. For stress compensation, lattice defects are produced in the surroundings and clustering of the dopant ions may occur, resulting in a variety of distorted lattice sites. A second consequence of the different ionic radii is the effective segregation coefficient[2] k_{eff}. Microprobe measurements at the University of Hamburg as well as ICP-OES[3]-measurements in Berlin at the Institut für Kristallzüchtung (IKZ) resulted in a value of 0.22.

Figure 2.3(b) displays the phase diagram of YLF. Due to incongruent melting behaviour, crystal growth of YLF by the Czochralski method is performed with a slight shift in stoichiometry to avoid YF_3-inclusions in the grown crystal. The starting composition is the peritectic one with YF_3:LiF = 47:53. As can be seen in the phase diagram, the growth

[1]Microtwinning denotes the formation of microscopic crystallites by a reflection or a rotation of the surrounding crystal structure

[2]The segragation coefficient is defined as the ration between the concentration of a component in the solid material c_s and the concentration of the same component in the liquid phase c_l: $k_{eff} := \frac{c_s}{c_l}$

[3]ICP-OES: inductively coupled plasma optical emission spectroscopy

temperature must be changed from 850°C in the beginning to 709°C due to the shift of the melt composition during growth. When the eutectic point at 709°C is reached, LiF is incorporated into the YLF single crystal reducing the optical and structural quality. At this point, the growth process is terminated.

YLF single crystals feature a large anisotropy. Thus, the cross-sections of absorption and emission are polarization dependent, favouring polarized lasers as pump sources. The resulting laser emission from Pr^{3+}:YLF crystals is strongly polarized as well. Polarized laser radiation is necessary for several nonlinear processes such as second harmonics generation (SHG).

2.2.2 Lithium-Lutetium-Fluoride

Lithium-Lutetium-Fluoride ($LiLuF_4$ or LLF) single crystals are isomorphic to YLF resulting in comparable structural and optical properties. Some of them are listed in Table 2.3.

Crystal system	tetragonal
Space group (Schönfließ)	$I4_1/a$ (C^6_{4h})
Site symmetry of Lu^{3+}	S_4
Formula units per unit cell Z	4
Lattice constants (Å)	a = 5.123 c = 10.520
Thermal conductivity k (W/(m·K))	6
Refractive indices ($\lambda = 632.8\,\mathrm{nm}$)	$n_o = 1.468$ $n_e = 1.494$
Effective phonon energy $\hbar\omega_{\mathrm{eff}}$ (cm^{-1})	<450
Density ρ ($\mathrm{g/cm}^3$)	6.186
Mohs hardness	3.5 - 4.5

Table 2.3: Structural and optical properties of LLF [Kam93b, Web03]

LLF features a slightly smaller lattice constant, higher indices of refraction as well as a higher mass density. In analogy to YLF, trivalent rare earth ions enter the Lu^{3+}-sites in LLF (Figure 2.4(a)). In case of 6-folded coordination, Lu^{3+}-ions posess an ionic radius of 1.00 Å. Thus, large ions like Pr^{3+} are most likely inducing more stress to the lattice structure of LLF than of YLF. Additionally, the difference in the ionic radii affects the segregation coefficient k_{eff} as well: For Pr^{3+} in LLF, the value is in between 0.1 and 0.2. The Pr^{3+}-concentration in these samples was measured by ICP-OES and by AAS[4], respectively.

[4]AAS: atomic absorption spectroscopy

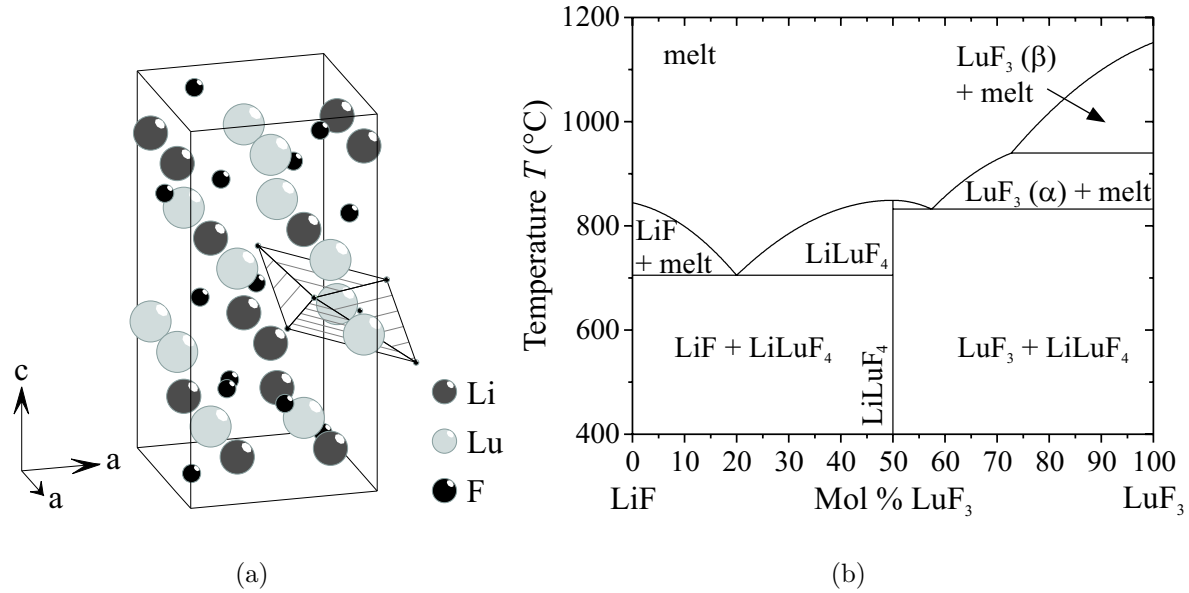

(a) (b)

Figure 2.4: (a) Unit cell of LLF. The polyhedron composed by the fluoride ligand locations of a Lu^{3+}-ion is highlighted [Kam93b]. (b) Phase diagram of the LiF-LuF_3 system [Har83].

Concerning the crystal growth by the Czochralski method, LLF has some advantages in comparison to YLF. Figure 2.4(b) shows the phase diagram of the system LiF-LuF_3. The melting temperature of LLF is 830°C at a stoiciometric melt composition. LLF exhibits a clear monotectic melting behaviour which favours the growth of LLF single crystals with high optical quality, because during the growth run no shift in the stoichiometry of the melt occurs.

2.2.3 Barium-Yttrium-Fluoride

Rare earth doped Barium-Yttrium-Fluoride (BaY_2F_8 or BYF) single crystals as active laser media have been demonstrated several times [Joh74, Kam86]. Because of the monoclinic crystal structure this optically biaxial crystal is not as widespread as YLF. A brief overview of the properties is given in Table 2.4.

Figure 2.5(a) shows the unit cell of BYF, which contains 2 formula units. Rare earth dopant ions substitute the Y^{3+}-ions in the lattice. The polyhedron of the Y^{3+}-ligands exhibits a low level of symmetry and consists of 10 fluorine ions. The ionic radii of Pr^{3+} and Y^{3+} could not be found for this coordination number. However, according to the segregation coefficient k_{eff} of 0.4 to 0.5, their ratio is certainly closer to one than in case of YLF.

According to the phase diagram given in Figure 2.5(b), BYF melts congruently at a tem-

Crystal system	monoclinic
Space group (Schönfließ)	C2/m (O_h^5)
Site symmetry of Y^{3+}	C_2
Formula units per unit cell Z	2
Lattice constants (Å)	a = 6.935 b = 10.457 c = 4.243 $\beta = 99.4°$
Coefficient of thermal expansion α (K^{-1})	17×10^{-6} along $\vec{a}$ 18.7×10^{-6} along $\vec{b}$ 19.4×10^{-6} along $\vec{c}$
Thermal conductivity k (W/(m·K))	6
Refractive indices ($\lambda = 632.8$ nm)	$n_x = 1.5142$ $n_y = 1.5232$ $n_z = 1.5353$
Phonon energy $\hbar\omega_{eff}$ (cm^{-1})	350
Density ρ (g/cm^3)	4.97 - 5.806
Mohs hardness	4-5

Table 2.4: Structural and optical properties of BYF [Gui93, Ton99, DeS00, Web03]

perature of 960°C enabling the growth of large boules with high optical quality. BYF combines some beneficial properties for laser host materials: a low phonon energy which practically disables phonon-induced nonradiative decay, narrow and strong polarized emission and absorption bands as well as a good capability for growth of high quality single crystals with high dopant concentrations.

2.2.4 Pottassium-Yttrium-Fluoride

Potassium-Yttrium-Fluoride (KY_3F_{10} or KYF) single crystals form a Fluorite-type cubic lattice. The unit cell, which is displayed in Figure 2.6(a), consists of 8 formula units in a volume of $(11.536\,Å)^3$. Rare earth ions replace Y^{3+}-ions, which are surrounded by 8 fluorine ions forming antiprisms. One antiprism is shown in Figure 2.6(a) as well. Due to the different ionic radii of Pr^{3+} (1.28 Å) and Y^{3+} (1.16 Å), the segregation coefficient k_{eff} differs from one. It was determined by ICP-OES- and AAS-measurements to be $k_{eff} = 0.5$. Recent structural and optical investigations on Pr^{3+}:KYF revealed a partially disordered structure [Bra07].

The phase diagram of the binary system KF-YF_3 is displayed in Figure 2.6(b). KYF melts

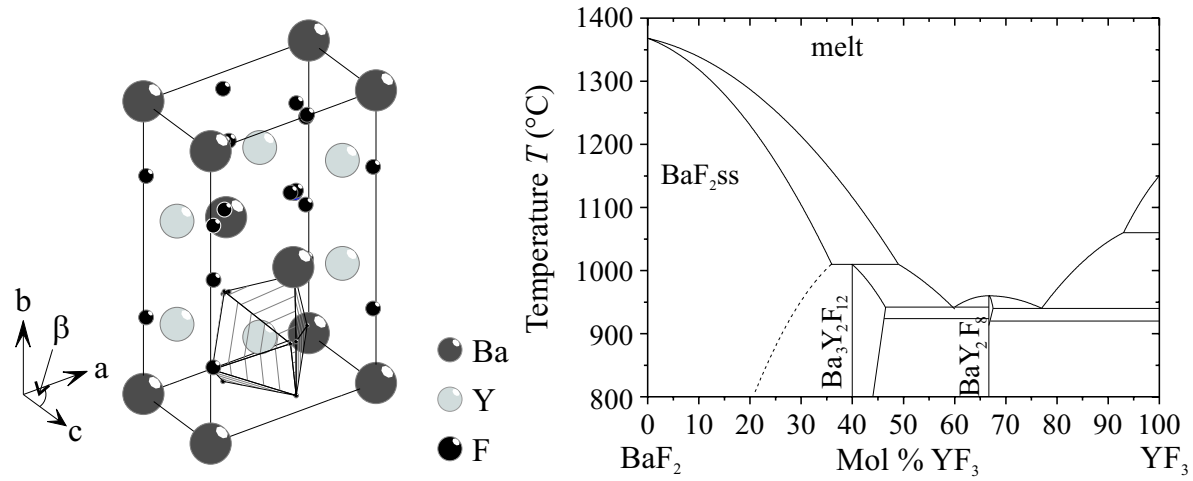

(a) (b)

Figure 2.5: (a) View at the unit cell of BYF. The polyhedron defined by the surrounding fluoride ligands of an Y^{3+}-ion is marked [Gui93]. (b) Phase diagram of the system BaF_2-YF_3 [Sob82].

congruently at a temperature of 1030°C and does not feature any phase transition below the melting point. The growth of large single crystalline boules of KYF with high optical quality is feasible.

KYF is a promising host material for diode pumped solid state lasers (DPSSLs), because optical absorption and emission have a broad band structure and are polarization-independent. Simultaneously, the peak cross-sections are reduced in comparison to the single crystalline materials discussed before.

Crystal system	cubic
Space group (Schönfließ)	Fm-3m (C_{2h}^3)
Site symmetry of Y^{3+}	C_{4V}
Formula units per unit cell (Z)	8
Lattice constant (Å)	a = 11.536
Coefficient of thermal expansion α (K^{-1})	1.45×10^{-5}
Refractive index n ($\lambda = 600\,\mathrm{nm}$)	1.4856
Effective phonon energy $\hbar\omega_{\mathrm{eff}}$ (cm^{-1})	420
Density ρ (g/cm^3)	4.312
Mohs hardness	4.5

Table 2.5: Structural and optical properties of KYF [Pie74, Mor82, Abd87, Web03]

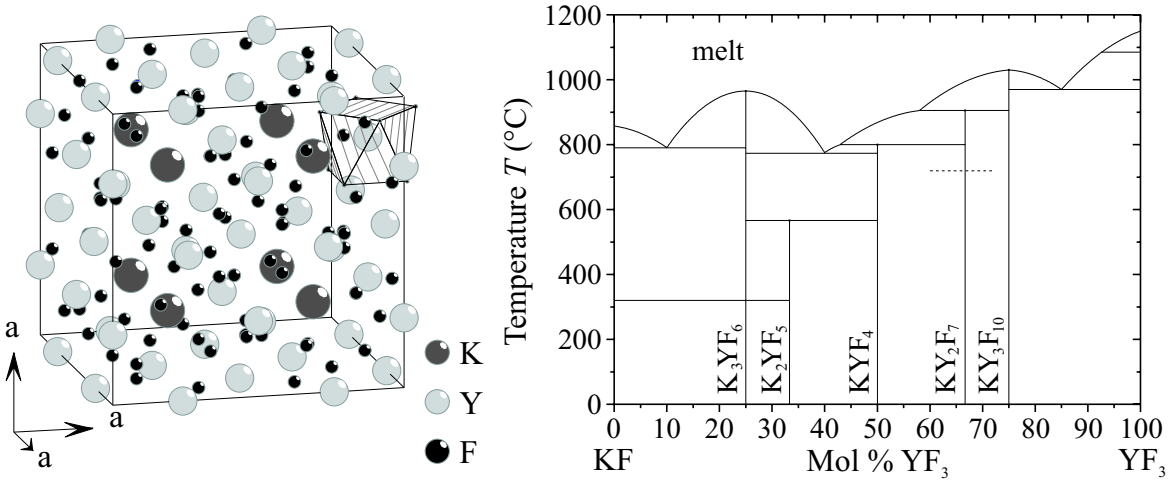

(a) (b)

Figure 2.6: (a) Unit cell of KYF. The polyhedron defined by the surrounding fluoride ligands of an Y^{3+}-ion is highlighted. [Pie74] (b) Phase diagram of the binary system KF-YF_3 [Abd87]

2.3 Improvement of the Crystal Growth Setup

Crystals for laser applications need to fulfill certain structural requirements leading to an enhanced optical quality of the material. Thus, it is crucial to suppress the generation of grain boundaries, bubbles, cracks, stress, and inclusions of different phases inside the crystal boule. To achieve an enhanced quality, the crystal growth procedure, the crystal growth setup, and the different material specifications have to be considered.

In the following paragraphs several challenges of the crystal growth process and their influence on the crystal quality will be discussed. A more detailed overview of the difficulties of crystal growth can be found in the book by Wilke and Bohm [Wil88].

2.3.1 Cracking of Single Crystalline Material during the Growth Process

Single crystalline material may crack along the growth axis beginning a few millimeters above the crucible edge. The reason for this behaviour is a high thermal gradient of a few hundreds of centigrades per centimetre above the crucible. This leads to thermal stress and induces cracking along the growth axis. Using an appropriate passive heat shield the axial thermal gradient can be reduced to approximately $80\,\mathrm{K\,cm^{-1}}$. Application of an active heat shield reduces the gradient even more. Klimm has estimated a thermal gradient of only $30\,\mathrm{K\,cm^{-1}}$ using an afterheater system [Kli00]. In the setup used in this work, a carbon heat shield (cf. Figure 2.1) was mounted on top of the inner crucible, which led to uncracked single crystals.

2.3.2 Impurities on the Surface of the Melt

Carbon particles contaminate the surface of the melt at the beginning of the growth procedure. Because these particles support polycrystalline growth if they get into contact with the growing crystal, seeded crystal growth is almost impossible. The different carbon-made compounds of the growth setup produce the contaminating particles. The minority is caused by those compounds made of glassy carbon. To reduce the carbon contaminations, the whole set-up might be modified by using glassy carbon components only or platinum components. Furthermore, an additional cleaning process would enhance the growth conditions. For example, Bensalah et *al.* remove the carbon particles after a first melt run in the growth chamber [Ben04]. In this case, the contaminations are already on top of the the solidified material and are easily scraped off. The crystal growers from Pisa remove the contaminations prior to crystal growth by dipping a platinum net into the melt which collects the carbon particles at the surface of the melt. After purification, the net is exchanged by the seed crystal and the crystal growth process is initiated.

Additionally, solidified material accumulates on the surface. This material begins melting at slightly higher temperatures. The nature of the solidified material is unknown. Pos-

sible reasons might be the temperature profile at the upper corner of the crucible or the formation of hydrogenated or oxidized fluoride compounds due to remaining contaminations of water vapour or oxygen in the atmosphere. Water vapour contaminations might be removed by heating the crucible while evacuating the growth chamber [Pam75]. This procedure is mentioned in the paper of Bensalah [Ben04]. In case of YLF, the temperature was set to 700°C for 12 hours. Further improvements in reducing the content of water vapour in the growth atmosphere can be achieved by insertion of P_2O_5 in the growth chamber during a growth run.

Regarding both challenges, a compromise was made in this work. To remove the impurities, a polycrystalline, cap-like shape was grown at the beginning. This cap collects almost all contaminations (carbon particles as well as unwanted oxyfluoride materials) and leaves excellent growth conditions for single crystalline material behind. This approach prevents on the one hand oriented crystal growth, but on the other hand shortens the time of the whole growth procedure.

2.3.3 Evaporation of Melt Compounds

After a certain number of crystal growth runs white powders cover the interior of the chamber and the components. It is most likely that the white powders are volatile compounds like LiF which evaporate from the melt surface at the border of the crucible during the growth process [Kli00]. This evaporation process affects the melt composition by changing the stoichiometry. Thus, generation of inclusions of different phases in the crystal are observed during the growth process (see next section). To reduce the amount of evaporating raw materials, the time of 'overheating' must be reduced. This results in smaller shifts of the melt composition. For compensation, the initial melt composition can be adjusted accordingly. In this way, the optimal stoichiometry is established during the growth process. LiF-evaporation during growth was considered by adding (1-2) mol.% of LiF in excess to the starting compounds.

2.3.4 Macroscopic Defects

At a certain point of the growth process of Pr-doped YLF and LLF, inclusions appear. Parasitic phases begin to crystallize in the core region and increase in diameter until reaching the surface, forming a pine tree shape as shown in Figure 2.7.

This process is the result of constitutional supercooling. Constitutional supercooling was first reported by Rutter [Rut53] and predominantly occurrs in melts containing a component with $k_{\text{eff}} \ll 1$. Figure 2.8(a) and (b) shows the concentration profile $c^{\text{L}}(z)$ of the component as well as the melt temperature profile $T^{\text{L}}(z)$. The index L denotes the liquid phase, L_0 denotes the conditions at the crystal interface and L_∞ denotes the conditions far away from the interface region. Due to the low segregation coefficient, PrF_3 is accumulating in front of the crystal interface leading to the concentration distribution depicted in

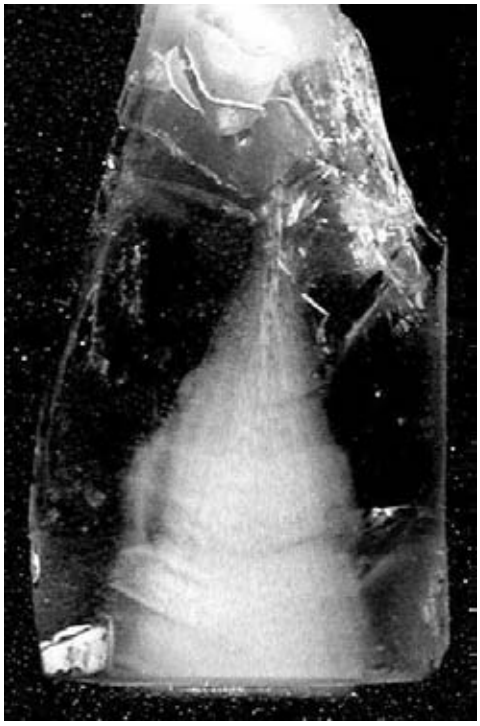

Figure 2.7: Photograph of the cross-section of a single crystal featuring constitutional supercooling

Figure 2.8(a). As a consequence the melt temperature $T^{\mathrm{L}}(z)$ is reduced with respect to the corresponding liquidus curve as displayed in Figure 2.8(b). Under growth conditions, the temperature of the crystallized material and the melt is equal at the interface. Assuming a linear increase of the melt temperature with respect to the distance from the interface, the axial temperature gradient $G_{\mathrm{T}} = \partial T/\partial z$ can be defined. Constitutional supercooling occurs if the gradient G_{T} (see dashed line in Figure 2.8(b)) is lower than the gradient defined by $\frac{\partial T^{\mathrm{L}}}{\partial z}|_{z=0}$. Under these conditions, the melt temperature is below the liquidus temperature in a certain volume below the interface (striped area in Figure 2.8(b)) and the formation of secondary nuclei leads to a fast crystallization process of the concentrated compound. After this process, the stoichiometry of the melt is restored and the crystal will continue growing, starting again to accumulate the less soluable compound in front of the interface. Depending on the thermal conditions during the growth, constitutional supercooling generates different shapes of phase inclusions like small particles or equidistant striations inside the growing materials. In the latter case, it is possible to determine the profile of the interface easily by studying the shape of the striations. The pine tree shaped striations in Figure 2.7 might be a result of changing thermal conditions during the growth process. In the beginning the axial thermal gradient is high enough to suppress supercooling, while later on this gradient is reduced. The reason for the depicted shape is the result of different axial thermal gradients at the crystal interface. Due to

the thermal conductivity of the solid and liquid phase, the gradient is lower in the core region than at the surface. Additionally the atmosphere above the melt surface is heated by the crucible walls resulting in further reduction of the axial thermal gradients during the growth leading to an increased area where constitutional supercooling occurs.

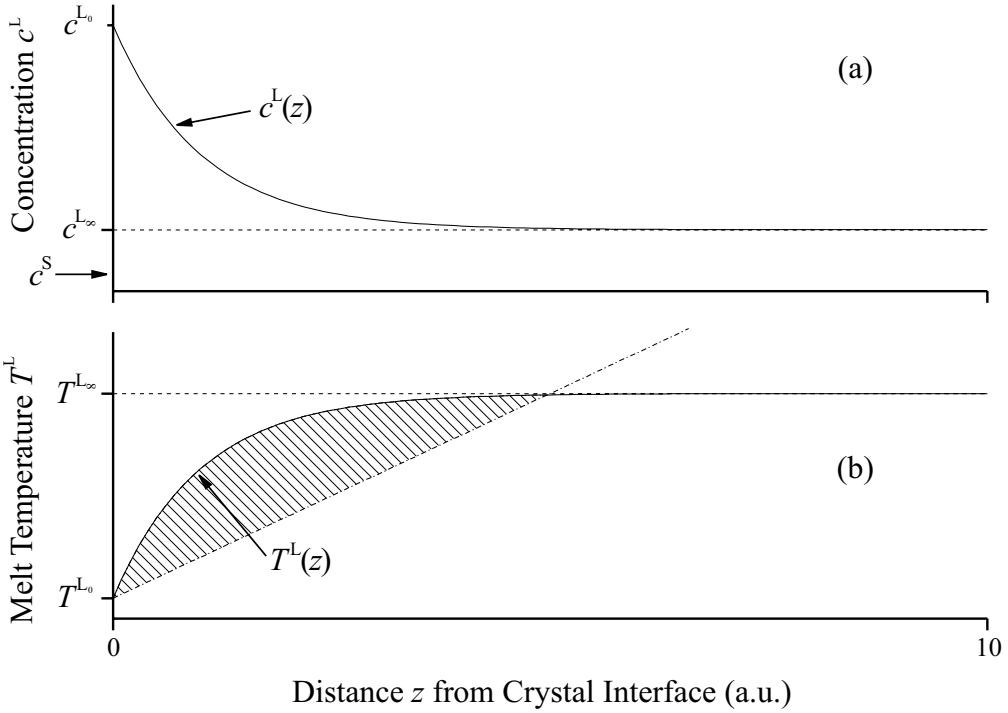

Figure 2.8: (a) Concentration distribution and (b) Corresponding liquidus temperature as well as the temperature distribution causing constitutional supercooling (dashdotted line and striped area) from [Wil88]

To suppress constitutional supercooling, it is necessary to avoid accumulation of one component in front of the crystal interface and to increase the axial thermal gradient. The former is obtained by applying lower pulling rates so that the convection of the melt results in a more homogeneous melt composition or by applying higher rotation rates of the growing crystal. However, by increasing the rotation rate, the convection scheme and heat distribution in the melt are affected. In case of a slowly rotating crystal, the flow shown in Figure 2.9(a) produces a convex crystal interface. By increasing the rotation rate above a critical value, which is dependent of the viscosity of the melt, both, the flow direction and the temperature profile are inverted in the upper region of the melt due to the centrifugal force at the crystal interface (Figure 2.9(b)). In consequence the shape of the interface changes from convex to concave and the direction of crystallization is inverted. Under these conditions, cellular growth benefits precipitations and the core region becomes strongly distorted. The critical rotation rate can be calculated if the geometry and the viscosity of the system is known, but no publications regarding the

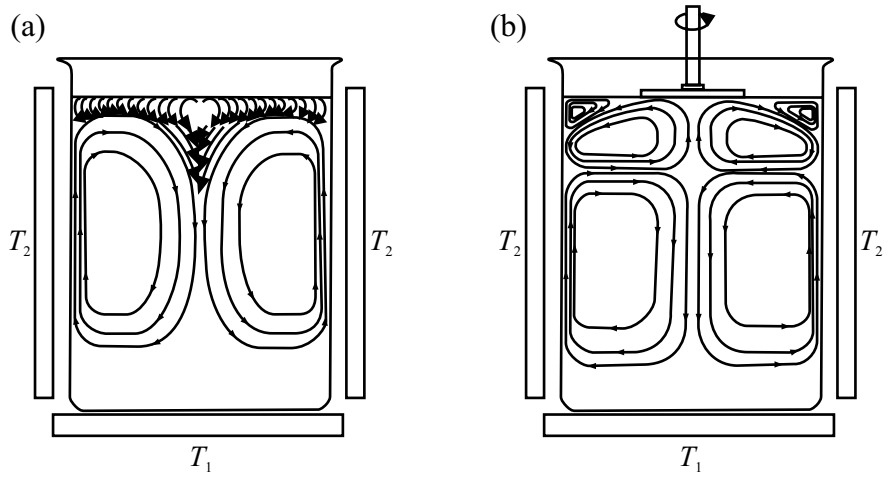

Figure 2.9: Convection of a model liquid inside a crucible ($T_2 > T_1$) (a) without crystal (b) with fast rotating crystal [Mil81, Mil82]

melt viscosity of the binary fluorides of interest have been found. Thus, further increase in the crystal quality of Pr^{3+}:LLF and Pr^{3+}:YLF can be reached by reducing the pulling speed. To increase the axial thermal gradient, the thermal conditions can be adjusted by increasing the distance between heat shield and inner crucible. However, the gradient should not result in cracked single crystals. The radial thermal conditions can be modified by applying a larger ratio between the diameters of the crucible and the growing crystal.

2.4 Summary

In summary, the results of the fluoride crystal growth of YLF, LLF, and KYF were presented in this chapter. The optical quality was sufficient for realizing efficient lasing of these materials (cf. Sections 4.4 and 4.5). Further improvements in crystal quality should be obtainable by reducing the carbon contaminations, an additional heating process during the evacuation process and application of a reduced rotation rate. Furthermore, modifications of the axial temperature gradient reduce the effect of constitutional supercooling.

3 Spectroscopic Investigations on Praseodymium doped Fluorides

3.1 Theoretical Aspects

This section focuses on the basic theoretical background for the spectroscopic experiments in this work. After a general introduction to the trivalent rare earth ions, in particular Pr^{3+}-ions, and their energy level structure in a crystal field, a more detailed description of the interionic energy transfer processes based on the model of Förster [För48] and Dexter [Dex53] induced by different mechanisms will be presented. A more generalized overview on the field of rare earth spectroscopy can be found in the book of Henderson and Imbusch [Hen89].

3.1.1 Rare Earth Ions

The term rare earths (REs) usually refers to the lanthanides, which are the elements lanthanum (atomic no. 57) through lutetium (atomic no. 71) and the chemically similar elements scandium (atomic no. 21) and yttrium (atomic no. 39). The following discussion, however, will only address the lanthanides.

The electron configuration of the lanthanides is $[Xe](4f)^n(5d)^x(6s)^2$. Here $x = 1$ in case of lanthanum ($n = 0$), gadolinium ($n = 7$), and lutetium ($n = 14$) and $x = 0$ for $n = 2$ through $n = 13$ for cerium through ytterbium. In ionic crystals the rare earths are usually incorporated as stable trivalent ions. The electron configuration for the trivalent lanthanides is $[Xe](4f)^{n+x-1}$.

The spectroscopic properties of the trivalent rare earth ions are dominated by transitions form $4f$ states to $4f$ and $5d$ states. Due to the completely filled $5s$ and $5p$ shells the $4f$ electrons are well shielded from influences of the crystal field [Bur62, Ray63, Ste66]. This results in a low variation of the $4f$ states in different local environments and narrow transition linewidths compared to those observed in transition metals, divalent rare earth ions and RE^{3+} $5d$-states [Hen89]. Furthermore, with rising atomic numbers, the strength of this shielding decreases [Ste66, Erd72].

The average distance of the $4f$ electrons to the nucleus as well as the radius of the trivalent ion decreases throughout the lanthanide row due to the stronger attraction of the electrons by the nucleus. This lanthanide contraction effects the ion in the crystal field. Generally,

the $4f$ electrons of smaller ions are less affected by the crystal field of the host material than larger ions in the same host as their mean distance to the neighbouring ions is larger [Ray63, Ste66, Erd72].

The Free Ion

In order to calculate the energy level scheme of the rare earth ions, the Hamiltonian of the system must be determined and the Schrödinger equation must be solved. Since no analytical solution can be found for systems with more than one electron, the system is first reduced to a radial, effective central field without electron-electron interaction in the so-called central field approximation. The resulting Hamiltonian $\widehat{H}_0$ is then corrected by additional perturbation terms of first order for the non-radial Coulomb interaction between the electrons, $\widehat{H}_{\mathrm{ee}}$, and the spin-orbit coupling of the electrons, $\widehat{H}_{\mathrm{so}}$. Further corrections for configurational-, spin-spin-, orbit-orbit-, and hyperfine interaction are ignored, since their influence is small compared to the crystal field interaction which will be introduced later.

In the central field approximation the Hamiltonian of an N-electron system is

$$\widehat{H}_0 = \sum_{i=1}^{N}(-\frac{\hbar^2}{2m_{\mathrm{e}}}\Delta_{r_i} + V(r_i)) \tag{3.1}$$

where $(-\hbar^2\Delta_{r_i}/(2m_{\mathrm{e}}))$ describes the kinetic energy and $V(r_i)$ the potential energy of the i-th electron at the distance r_i from the nucleus. This Hamiltonian can be separated and the solution Ψ_0 of the time-independent Schrödinger equation with the energy eigenvalues E_0

$$\widehat{H}_0\Psi_0 = E_0\Psi_0 \tag{3.2}$$

is the product of the eigenstates of the single electron wave functions $|n_i l_i m_l m_s\rangle$:

$$\Psi_0 = \prod_{i=1}^{N} |n_i l_i m_l m_s\rangle \,. \tag{3.3}$$

Here, n_i denotes the principal quantum number and l_i the orbital angular momentum of the i-th electron. The energy eigenvalues depend only on n_i and l_i. In this model, the magnetic quantum numbers m_l and spin quantum numbers m_s are degenerated.

According to the Pauli exclusion principle, the total wave function Ψ_0 has to be completely anti-symmetric, since two electrons cannot share the same single particle state. This is ensured by writing the total wave function as Slater determinant of the single particle wave functions.

A self-consistent central potential can be determined iteratively by the Hartree-Fock-method. Starting with a chosen potential the calculated potentials converge by successive iteration with the Hartree-Fock-equations towards the self-consistent potential $V(r)$ of the system.

The first perturbation term which will be considered in Schrödingers equation is the non-radial part of the Coulomb interaction $\widehat{H}_{\mathrm{ee}}$ between the individual electrons

$$\widehat{H}_{\mathrm{ee}} = \sum_{i<j=1}^{N} \frac{e^2}{(4\pi\epsilon_0)\,|\vec{r}_i - \vec{r}_j|} - \sum_{i=1}^{N} \left(\frac{Ze^2}{(4\pi\epsilon_0) r_i} - V(r_i) \right) \tag{3.4}$$

with the elementary charge e, the atomic number Z, the permittivity of free space ϵ_0, and the distance $|\vec{r}_i - \vec{r}_j|$ between the electrons in question. The electron-electron interaction causes a splitting of the $4f^n$-state in distinct LS-levels, where the total orbital angular momentum is $L = |\vec{L}|$ with $\vec{L} = \sum_i \vec{l}_i$, and $S = |\vec{S}|$ is the total spin with $\vec{S} = \sum_i \vec{s}_i$. The resultant wave functions are described with the quantum numbers L, S, M_L, and M_S. The energy splitting of the LS-terms is typically of the order of $10^4\,\mathrm{cm}^{-1}$ (see Figure 3.1).

The second necessary perturbation term of the central field approximation is the spin-orbit interaction

$$\widehat{H}_{so} = \sum_{i=1}^{N} \frac{1}{2m^2c_0^2} \cdot \frac{1}{r_i} \cdot \frac{dV(r_i)}{dr_i} \cdot (\vec{l_i} \cdot \vec{s_i}). \tag{3.5}$$

There, c_0 denotes the vacuum speed of light.

Further splitting of the energy levels depends on the coupling of the electrons. If $\widehat{H}_{\mathrm{so}}$ is weak compared to $\widehat{H}_{\mathrm{ee}}$, the LS- (or Russel-Saunders-) coupling is valid. In this case, the total orbital angular momentum and the total spin are coupled to form the total angular momentum $\vec{J} = \vec{L} + \vec{S}$. The influence of the spin-orbit interaction leads to a splitting of the LS-terms into J-manifolds. In the case of very heavy elements the spin-orbit interaction is strong and the angular momentum of the electrons $\vec{j_i} = \vec{l_i} + \vec{s_i}$ are coupled together to the total angular momentum $\vec{J} = \sum_i \vec{j_i}$. In case of lanthanides the influence of both perturbation terms is of comparable magnitude. Therein, the intermediate coupling is valid. The eigenstates are linear combinations of several LS-states of the same total angular momentum J and different ${}^{2S+1}L$-manifolds can energetically overlap in their J-components. The state is identified by the LS-state with the strongest influence. The total angular momentum J, however, remains to be a good quantum number. The eigenstates are designated after the quantum numbers L, S, and J. These ${}^{2S+1}L_J$-states are $(2J+1)$-fold degenerate in M_J [Hen89]. The energetic splitting of the ${}^{2S+1}L_J$-terms is typically in the range of $10^3\,\mathrm{cm}^{-1}$ (see Figure 3.1).

Rare Earth Ions in a Crystal Field

When a RE-ion is incorporated into a crystal lattice, it is subject to the electrostatic field of the ligands[1]. The crystal field potential can be introduced as an additional perturbation term to the free ion Hamiltonian. The potential of the crystal field can be written as:

$$\widehat{H}_{\mathrm{cf}} = \sum_{k,q} B_q^k C_q^{(k)}. \tag{3.6}$$

The $C_q^{(k)}$ are tensor operators and the crystal field parameters B_q^k are adjustable parameters [GW96].

The crystal field has two effects on the energy level structure of a free ion: It induces a red-shift on the free ion levels (the so-called nephelauxetic effect) and can be explained by a reduction of the free-ion parameters [Jør77]. The second effect of the crystal field on the free ion is breaking the M_J-degeneracy of the $^{2S+1}L_J$-manifolds. The Stark splitting of the manifolds is usually in the order of some $100\,\mathrm{cm}^{-1}$ (see Figure 3.1). In case of ions with an even number of electrons, the manifolds are split into $(2J+1)$ levels [Mes90], while for odd numbers of electrons the Kramers-theorem has to be considered and the $^{2S+1}L_J$-manifolds split only in $(2J+1)/2$ Stark-levels and a degeneracy of 2 is still left.

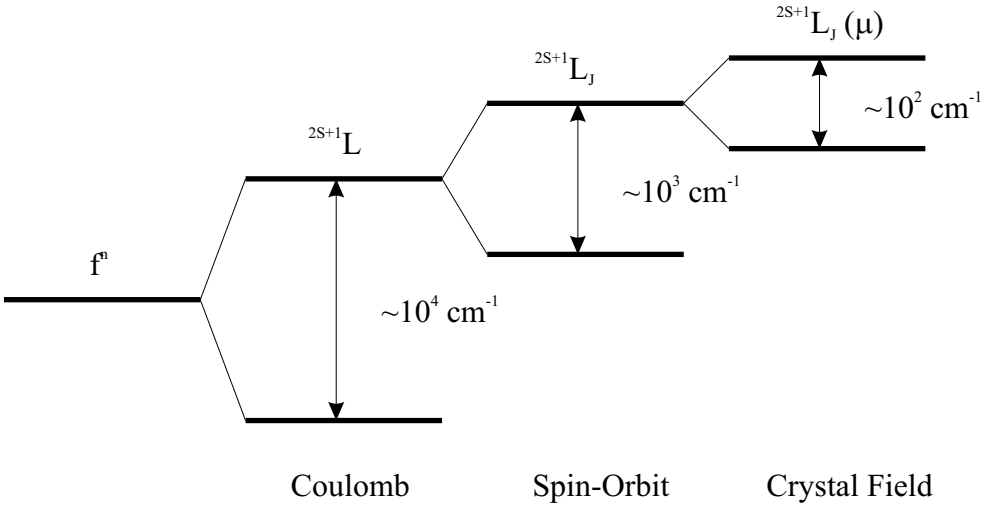

Figure 3.1: Principle overview of the influence of the different perturbation terms on the energy level splitting and labeling

[1] ligands: neighbouring ions

The Trivalent Praseodymium Ion

Praseodymium is the third lightest element of the lanthanides with the atomic number of Z=59. In dielectric crystals, praseodymium is preferably incorporated in its trivalent state (Pr^{3+}). In the trivalent state Pr^{3+}-ions have two $4f$-electrons which can occupy 13 energy states inside the $4f$-orbitals. According to Hund's rules [MK85], the $^3H_4$-state resembles the ground state. Figure 3.2 (left) gives an overview on the energy level splitting of the $4f^2$ and the $4f5d$ states of the trivalent praseodymium ion. Directly below the $4f5d$ states at about 46.000 cm^{-1} lies the highest $4f^2$ energy level $^1S_0$ [Loh65]. On the right side of Figure 3.2 an enlargement of the lower 12 energy levels of the $4f^2$-states including the Stark splitting is shown. The energy levels below the $^3F_4$ are thermally coupled resulting in very low effective lifetimes [Est79, Koc90]. The energy levels above 45.000 cm^{-1} are of any concern regarding the investigated laser processes in the investigated fluoride compounds. By excitation of the ^3P_J-manifold, several radiative transitions in the visible spectral range from the blue to the near infrared spectral range occur. The $4f$-$4f$-transitions of Pr^{3+} offer cross-sections of several 10^{-19} cm^2 in anisotropic crystals [Osi03b, Ric04b].

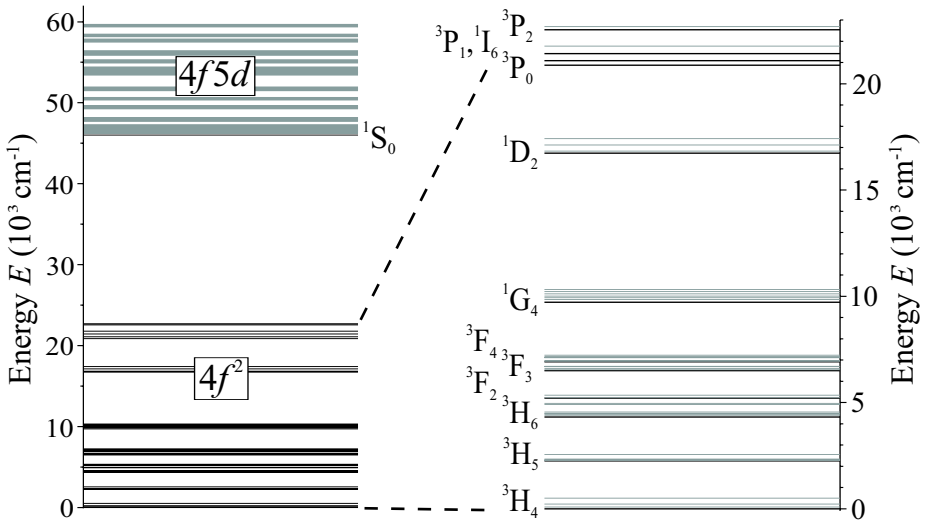

Figure 3.2: Energy level scheme of the $4f^2$- and $4f5d$-states of Pr^{3+} in YLF [Ada85, Lar00]

3.1.2 Energy Transfer

Intraionic Processes

Ions which interact with photons or phonons are involved in intraionic processes. These processes can be classified in radiative and nonradiative transitions. The first one describes interactions with photons only, while the latter one involves phonon-assisted transitions.

Radiative Transitions

The basic radiative transitions are ground-state absorption (GSA), stimulated emission, and spontaneous emission.

Absorption processes occur if the photon energy equals the energy difference between two energy levels. Depending on the initial energy state, GSA or excited state absorption (ESA) can occur. If the light intensity is sufficiently small, Beer-Lambert's law describes the absorption process and the intensity of the transmitted light passing a sample of thickness z light follows the exponential law

$$I(z) = I_0 \cdot \exp(-\alpha z). \tag{3.7}$$

I_0 is the initial intensity and the parameter α denotes absorption coefficient. The absorption cross-section σ_a can be calculated from the absorption coefficient if the dopant concentration N is known using Equation 3.8.

$$\sigma_\mathrm{a}(\lambda) = \frac{\alpha(\lambda)}{N} \tag{3.8}$$

Analogous to the GSA, ESA can occur. ESA on either the excitation wavelength or the wavelength of the laser transition can reduce the laser efficiency by depopulation of the upper laser level. On the other hand, ESA can be used to populate highly located energy levels allowing laser operation from those levels.

Spontaneous emission denotes the relaxation process of an excited ion by emitting a photon. The probability of emitting a photon for a given time interval dt and a given transition $|\psi_i\rangle \rightarrow |\psi_j\rangle$ is given by

$$dP_{ij} = \frac{dt}{\tau_{ij}} = A_{ij} dt \tag{3.9}$$

A_{ij} denotes the Einstein-parameter [Ein16]. The temporal behaviour of the fluorescence intensity follows an exponential decay curve. The radiative decay rate of state $|\psi_i\rangle$ is given by summation over all lower lying energy states $|\psi_k\rangle$

$$A_i = \sum_k A_{ik} = \sum_k \frac{1}{\tau_{ik}} \tag{3.10}$$

and the radiative lifetime of state $|\psi_i\rangle$ is

$$\tau_{\mathrm{R},i} = \frac{1}{A_i}. \tag{3.11}$$

The branching ratio β_{ij} describes the fraction of the decay channel $|\psi_i\rangle \rightarrow |\psi_j\rangle$ with respect to all radiative decays from state $|\psi_i\rangle$

$$\beta_{ij} = \frac{A_{ij}}{\sum_k A_{ik}}. \tag{3.12}$$

Stimulated emission on the transition $|\psi_i\rangle \rightarrow |\psi_j\rangle$ occurs if a photon with the same amount of energy is interacting with an ion in state $|\psi_i\rangle$. In this case, a second photon featuring the same energy, polarization and phase is emitted in the same direction as the initial photon. This is the crucial process for laser oscillation, because by stimulated emission of radiation, gain is generated. The transition probability is proportional to the corresponding emission cross-section. By using the principle of reciprocity [Ein16], the emission cross-section can be determined from the cross-sections of absorption in case of equal degeneracies of the involved states.

If a fluorescence photon is absorbed again by the same class of ions the process is called reabsorption. Reabsorption can become a significant process if the overlap of the absorption and emission is large. In particular, reabsorption is a well-known loss process for ground state lasers. Furthermore, it can prolong the measured lifetime of an excited state compared to the real lifetime of the level, which is the so-called radiation trapping process.

Nonradiative Transitions

Multi-phonon-relaxation is the transition of an excited state into a lower one by interaction with one or more lattice phonons. The excitation energy is directly transformed into heat by this process. Multi-phonon relaxation into energetically close levels is very fast and can effectively depopulate excited states. The temperature dependent nonradiative transition rate W_{nr} is described by [Ris68, Moo60]

$$W_{\mathrm{nr}}(T) = W_0 \cdot e^{-a\Delta E}[1 - e^{-\frac{\hbar\omega_{\mathrm{eff}}}{kT}}]^{-p}. \tag{3.13}$$

The empirical parameter W_0 depends on the host material and a describes the electron-phonon coupling, which can be considered weak in case of $4f$ electrons. ΔE is the energy difference between the two states and $\hbar\omega_{\mathrm{eff}}$ is the effective phonon energy of the host material, which depends on the lattice structure, bonding strength and the inter-ionic distances. The number of phonons needed to bridge the energy gap is given by $p = \frac{\Delta E}{\hbar\omega_{\mathrm{eff}}}$. The temperature dependence of W_{nr} can be neglected in case of praseodymium in fluorides because of their low phonon energies [Ada85]. The nonradiative lifetime of an excited state is defined as

$$\tau_{\mathrm{nr}} = \frac{1}{W_{\mathrm{nr}}}. \tag{3.14}$$

The effective lifetime τ_{eff} can now be calculated from the nonradiative (Eqn. 3.14) and the radiative lifetime (Eqn. 3.11):

$$\frac{1}{\tau_{\text{eff}}} = \frac{1}{\tau_{\text{R}}} + \frac{1}{\tau_{\text{nr}}}. \tag{3.15}$$

Selection Rules for Radiative Transitions

The radiative transitions in trivalent lanthanides mainly occur between $4f^n$-states. Since the initial and the final state of these transitions have the same parity, electric dipole transitions are forbidden by the Laporte selection rule and only magnetic dipole transitions can occur [Hen89]. In general, magnetic dipole transitions are weaker than electric dipole transitions by a factor of 10^5. Under the influence of a non-inversion symmetric crystal field, however, configurational mixing between $4f$ and opposite parity states like $4f^{n-1}5d^1$-states partly allow electric dipole transitions between $4f$-states in the lanthanides. In case of inversion symmetry the Laporte selection rule can be weakened by non-centric distortions like lattice defects. The weakening for sites with inversion symmetry is considerably smaller than the weakening for non-inversion sites.

The general selection rules for electric dipole transitions can be summarized as follows [Hen89, Kam90]:

1. $\Delta l = \pm 1$
2. $|\Delta S| = 0$
3. $|\Delta L| \leq 2l$
4. $|\Delta J| \leq 2l$

The mixing of $4f$ states and those of opposite parity and the resulting transition rates can be calculated using the Judd-Ofelt-theory [Jud62, Ofe62]. Unfortunately, the splitting of the ^{2S+1}L terms of the perturbing configuration into $^{2S+1}L_J$ has to be negligible compared to the energy gap between the states of opposite parity. This condition is not fulfilled for the $4f^2$ energy levels of Pr^{3+}. Thus, the results obtained from the Judd-Ofelt-theory can only be seen as a rough estimation.

Interionic Processes

Interionic processes involve the direct transfer of excitation energy between two ions without absorption or emission of photons. The ion which delivers excitation energy is labeled *donor* (D), the ion accepting even a fraction of the energy is called *acceptor* (A).

Depending on the energy difference of the excited states of the donor and the acceptor before and after the energy transfer process, it is possible to distinguish between *resonant* and *non-resonant* excitation energy transfer. A resonant energy transfer occurs when the amount of energy delivered resembles the amount of energy accepted. In the non-resonant case, a fraction of excitation energy is exchanged with the phonon field of the host lattice.

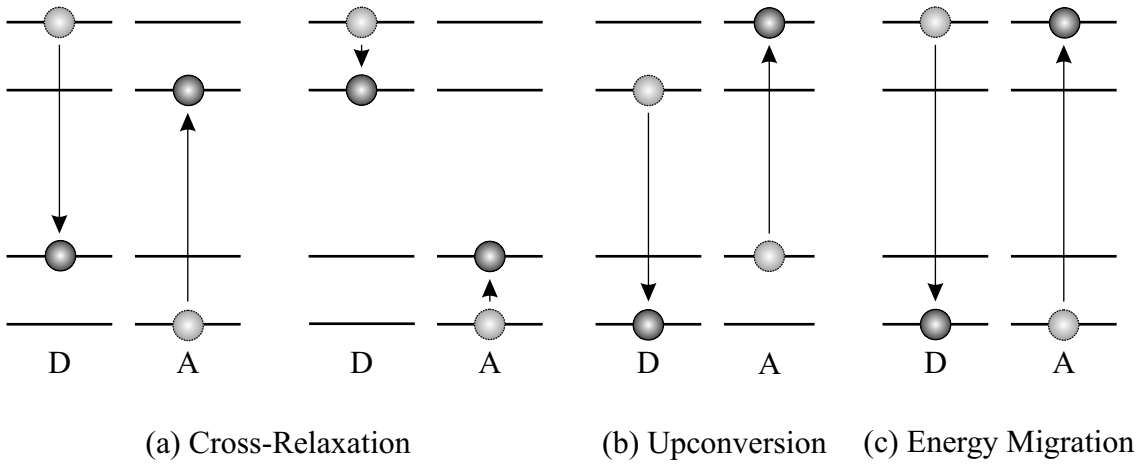

Figure 3.3: Possible interionic energy transfer processes between adjacent rare earth ions of the same type

Depending on the energetic state of D and A after the energy transfer process, one distinguishes between three processes: cross-relaxation, upconversion, and energy migration.

Cross-Relaxation

In the beginning of a cross-relaxation process (CRP), just the donor is in an excited state. After the interaction, the donor has lost a fraction of its excitation energy to the acceptor such that both ions are in an excited state (Figure 3.3(a)). CRPs exhibit losses for realizing lasers if the initial excited state of the donor ion resembles the upper laser level.

Energy Transfer Upconversion

To achieve energy transfer upconversion (ETU), the two ions involved in this process have to be in an excited state in the beginning (Figure 3.3(b)). In this case, the excitation energy from the donor is transferred to the acceptor leaving the accepting ion in an energetically higher state than the initial state of the donor. Using ETU processes, it is possible to populate highly located energy levels without direct excitation.

Energy Migration

While the energy is transferred from a donor to an acceptor in case of CRP and ETU, energy migration only takes place between two donors resulting in a resonant process (Figure 3.3(c)). This process accelerates both the ETU and CRP because the excitation energy is available in a large volume. In this case, the excitation energy can reach impurities or imperfections and energy migration provides losses.

Interaction Mechanisms

Interionic processes of interacting ions can be induced by multipolar or exchange interaction. These interaction types exhibit different characteristics regarding coupling strength and dependence on the interionic distance. The interaction mechanisms will be introduced shortly in the following paragraphs.

Multipolar Interaction

In case of multipolar interaction between two RE-ions, both magnetic multipole and electric multipole coupling is possible. In both cases, the corresponding fields of the donor and the acceptor ion interact with each other. Since the electric multipole interaction is several orders of magnitude stronger than the magnetic multipole interaction [Hen89], the following section will only focus on the electric multipole interaction.

The electric multipolar induced processes can be further separated with respect to the interacting multipolar fields. In case the electric dipole field of D interacts with the electric dipole field of A, this process is labelled dipole-dipole (dd). In the same way, dipole-quadrupole (dq), quadrupole-dipole (qd) and quadrupole-quadrupole (qq) induced interactions are defined. The radial dependence of the energy transfer rate for electric multipolar induced interactions is proportional to R^{-s}, where $s = 6$ for dd-, 8 for dq- and qd- and 10 for qq-induced interactions (cf. Section 3.1.3). Thus, dd-induced interactions feature large interaction lengths of several tens of angstroms [För48, För49] and are usually considered first when energy transfer processes occur in a system. Higher order multipolar induced energy transfer processes are at least two orders of magnitude smaller than dd-induced processes [Hen89].

Exchange Interaction

While multipolar interactions enable distant ions to transfer energy, the exchange interaction is based on the direct overlap of the electron wave functions of donor and acceptor [Lev69, Sil97, Had99]. Thus, the interaction range is limited to a few angstroms only. Nevertheless, the exchange-induced energy transfer rates are comparable to dd-induced transfer rates. Energy transfer by exchange interaction can also occur via the overlap of the electron wave functions of D and A with a ligand ion in between. This process is called a super-exchange process [Mir96].

3.1.3 Calculation of the Transfer Rate

In this section an overview of interionic processes, their occurrence, nature and influence on the deexcitation rate will be given. Beginning with the microscopic part of excitation energy transfer, the results obtained by Förster [För48] and Dexter [Dex53] will be introduced. Next, this model will be expanded to the description of multiple ions in a host material resulting in the continuum approximation of Inokuti and Hirayama [Ino65] in its static form. In a last step, the dynamic models, which involve energy migration, namely the *diffusion model* and the *hopping model* will be introduced briefly. Further details on

all of the models can be found in the book of Henderson and Imbusch [Hen89] and the review paper by Burshtein [Bur85].

Model of Förster and Dexter

Förster [För48] and Dexter [Dex53] developed a model for nonradiative energy transfer processes between a single donor and a single acceptor. They obtained a simple result for the intensity decay characteristics of the donor ion:

$$I(t) = I_0 \cdot \exp\left(-\frac{t}{\tau_{\mathrm{R}}} - W_{\mathrm{DA}} \cdot t\right) \tag{3.16}$$

with the energy transfer rate

$$W_{\mathrm{DA}} = \frac{2\pi}{\hbar}\left|\left\langle D, A^* \left|\hat{I}\right| D^*, A\right\rangle\right|^2 \Omega. \tag{3.17}$$

Here, $\hat{I}$ denotes the operator of the interaction mechanism, Ω reflects the overlap of the corresponding transition lines and τ_R denotes the lifetime of the donor without acceptors. D and A denote the donor and the acceptor in the ground state while D* and A* correspond to the excited states of these ions.

Förster assumed a *dd induced* interaction. In this case, the transfer rate obtains the following form [För48]:

$$W_{DA}^{dd} = \frac{3\hbar^4 c_0^4 Q_a}{4\pi n^4 R_{DA}^6 \tau_{\mathrm{R}}} \int \frac{f_{\mathrm{D}}(E) f_{\mathrm{A}}(E)}{E^4} dE \tag{3.18}$$

Herein, Q_a denotes the integrated absorption cross-section of the corresponding transition of the acceptor, f_D and f_A denote the normalized line shapes of the corresponding radiative transitions of donor and acceptor, and R_{DA} is the distance between the interacting ions.

To simplify the previous formula, the energy transfer microparameter $C_{\mathrm{DA}}^{\mathrm{dd}}$ will be introduced reducing Equation 3.18 to

$$W_{\mathrm{DA}}^{\mathrm{dd}} = \frac{C_{\mathrm{DA}}^{\mathrm{dd}}}{R_{\mathrm{DA}}^6}. \tag{3.19}$$

In case of dq-, qd- or qq-induced interactions the energy transfer rates $W_{\mathrm{DA}}^{(s)}$ can be defined in analogy to Equation 3.19

$$W_{\mathrm{DA}}^{(s)} = \frac{C_{\mathrm{DA}}^{(s)}}{R_{\mathrm{DA}}^s}. \tag{3.20}$$

In this equation, s corresponds to the order of the multipolar process involved as defined in Section 3.1.2.

Dexter [Dex53] determined the transfer rate in case of an *exchange-induced* energy transfer between donor an acceptor to be

$$W_{\mathrm{DA}}^{\mathrm{ex}} = \frac{2\pi}{\hbar} K^2 \exp\left(-\frac{2R}{L}\right) \int f_{\mathrm{D}}(E) f_{\mathrm{A}}(E) dE. \tag{3.21}$$

Here, K is a constant with a dimension of energy, L is called the "effective average Bohr radius" for the excited and unexcited states of D and A. Inokuti and Hirayama [Ino65] simplified Equation 3.21 and obtained:

$$W_{\mathrm{DA}}^{\mathrm{ex}} = \frac{1}{\tau_{\mathrm{R}}} \exp\left[\gamma_{\mathrm{x}} \left(1 - \frac{R}{R_{\mathrm{c}}}\right)\right] \tag{3.22}$$

by introducing

$$\gamma_{\mathrm{x}} = \frac{2R_{\mathrm{c}}}{L} \tag{3.23}$$

and

$$\frac{e^{\gamma_{\mathrm{x}}}}{\tau_{\mathrm{R}}} = \frac{2\pi}{\hbar} K^2 \int f_{\mathrm{D}}(E) f_{\mathrm{A}}(E) dE. \tag{3.24}$$

Herein R_{c} is the "critical transfer distance", namely the distance, in which the radiative decay rate matches the nonradiative energy transfer rate.

Approximation of Inokuti and Hirayama

Up to now, the considerations only took into account a single donor and a single acceptor interacting with each other (microscopic energy transfer). As a result, the decay rate of the donor luminescence, given by Equation 3.16, is single exponential in time. In macroscopic scales, the distribution of donors and acceptors in a crystalline material is completely homogeneous and the decay characteristics of the donor luminescence are non-exponential.

In the absence of energy transfer between donor ions, Blumen [Blu80] derived the following formula for the decay curve of an ensemble of excited donors:

$$I(t) = I_0 \cdot \exp\left(-\frac{t}{\tau_{\mathrm{R}}}\right) \prod_l \left[1 - c_{\mathrm{A}} + c_{\mathrm{A}} \exp(-W_{\mathrm{D_0 A}_l} \cdot t)\right] \tag{3.25}$$

c_{A} is the probability that a site is occupied by an acceptor and l refers to all lattice sites available. $W_{\mathrm{D_0A}_l}$ denotes the energy transfer rate from the donor at position 0 to the acceptor at lattice site l. Equation 3.25 is valid for both multipolar and exchange interaction between donor and acceptor. By assuming a continuous distribution of acceptors starting with a minimum distance R_0 around a donor and an electric multipole interaction, Watts [Wat75] deduced the following equation

$$I(t) = \exp\left(-\frac{t}{\tau_{\mathrm{R}}}\right) \cdot \exp\left[-\frac{n_{\mathrm{A}}}{n_0}\Gamma\left(1-\frac{3}{s}\right)\left(\frac{t}{\tau_{\mathrm{R}}}\right)^{3/s}\right] \tag{3.26}$$

Here, $\Gamma(x)$ is the gamma function. Due to the assumption of a continuous distribution of acceptors the influence of the closest acceptors is weighted too strong and Equation 3.26 is valid after a certain time t_1, which is defined as [Vor82]

$$t_1 = \frac{|\ln(1-c_{\mathrm{A}})|}{c_{\mathrm{A}}}\frac{R_0^6}{C_{\mathrm{DA}}^{\mathrm{dd}}} \tag{3.27}$$

In case of a *dd induced* excitation energy transfer, Inokuti and Hirayama [Ino65] derived for $t>t_1$

$$I(t) = I_0 \cdot \exp(-\frac{t}{\tau_{\mathrm{R}}} - \gamma_{\mathrm{i}}\sqrt{t}) \tag{3.28}$$

with

$$\gamma_{\mathrm{i}} = \frac{4}{3}\pi^{\frac{3}{2}} n_{\mathrm{A}} (C_{\mathrm{DA}}^{\mathrm{dd}})^{1/2} \tag{3.29}$$

Here, n_{A} denotes the acceptor concentration density. For shorter timescales $t<t_1$, Voron'ko [Vor76] and Blumen [Blu80] used Equation 3.25 to derive

$$I(t) = I_0 \cdot \exp\left(-\frac{t}{\tau_{\mathrm{R}}} - c_{\mathrm{A}} C_{\mathrm{DA}}^{(6)} t \sum_i \frac{1}{R_i^6}\right) \tag{3.30}$$

Assuming a continuous distribution of acceptors beginnig from R_0, this equation reduces to

$$I(t) = I_0 \cdot \exp\left(-\frac{t}{\tau_R} - \frac{4\pi}{3}\frac{C_{DA}^{dd} n_A}{R_0^3} t\right). \tag{3.31}$$

In case of an *exchange induced* energy transfer, one obtains

$$I(t) = I_0 \cdot \exp\left(-\frac{t}{\tau_R} - \gamma_x^{-3}\frac{n_A}{n_0} g(e^{\gamma_x} t/\tau_R)\right) \tag{3.32}$$

where

$$n_0 = \frac{3}{4\pi R_C^3} \tag{3.33}$$

is the critical ion density. The function g is given by

$$g(z) = -z \int_0^1 \exp(-zy)(\ln y)^3 dy. \tag{3.34}$$

Influence of Energy Migration

The considerations in the last section included two possible relaxation channels of an excited donor: either by emitting a photon or by transferring the excitation energy to an acceptor. In the next step, energy migration will be taken into account by extending Equation 3.28, accordingly.

In analogy to the microparameter C_{DA} describing the transfer rate from donor to acceptor, a microparameter depicting the donor-donor transfer rate, C_{DD}, can be defined. Depending on the ratio of these parameters, different models are valid. Furthermore, the critical concentration c^*, which describes the limit for the supermigration regime, can be approximated by

$$c^* = \left(\frac{C_{\mathrm{DA}}}{C_{\mathrm{DD}}}\right)^{1/8} \tag{3.35}$$

In Figures 3.4(a) and (b), the different sections of the nonradiative decay curve are displayed for the limiting cases $C_{\mathrm{DD}} \gg C_{\mathrm{DA}}$ and $C_{\mathrm{DD}} \ll C_{\mathrm{DA}}$.

The case of supermigration (Section IV in Figures 3.4(a) and (b)), which occurs at $c_{\mathrm{A}} > c^*$, the decay characteristics are single exponential, because the excitation energy is distributed over the whole number of donors before the energy is transferred to the acceptors. In case $c_{\mathrm{A}} < c^*$, the decay process can be divided into three stages. An initial exponential stage (Section I), which holds for $0 < t < t_1$. This decay goes over into the Förster decay curve (Section II). Beginning at t_2, given by Equation 3.41, the decay curve becomes single exponential again (Section III) due to energy migration processes.

Depending on the ratio between the energy transfer microparameters, different regimes and models are able to describe the excitation energy transfer processes.

Fast Migration Regime ($C_{\mathrm{DD}} \gg C_{\mathrm{DA}}$)

In case of fast migration between donors, every donor feels the same acceptor environment [Vor82] and Equation 3.25 results in

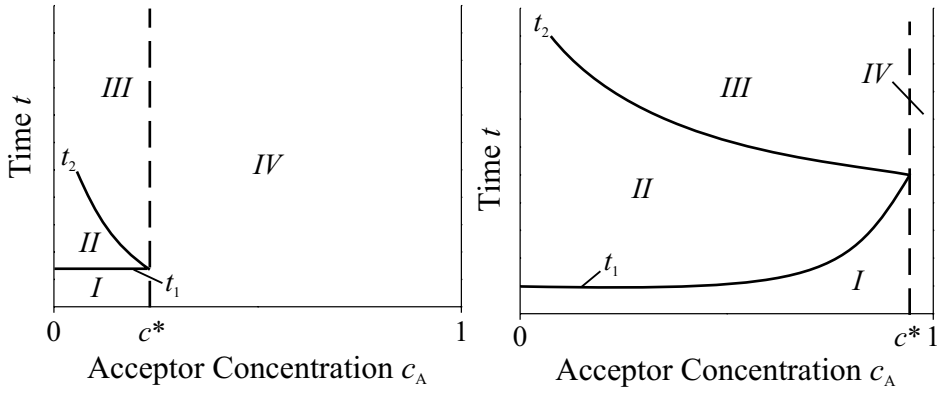

Figure 3.4: Different sections of the nonradiative decay curve in case of (a) $C_{\mathrm{DD}} \gg C_{\mathrm{DA}}$ and (b) $C_{\mathrm{DD}} \ll C_{\mathrm{DA}}$ [Vor76]. The regions *I*–*IV* are described in the text.

$$I(t) = I_0 \cdot \exp\left(-\frac{t}{\tau_{\mathrm{R}}} - W_{\mathrm{DA}} \cdot t\right) \tag{3.36}$$

where

$$W_{\mathrm{DA}} = c_{\mathrm{A}} \sum_{l} W_{\mathrm{D_0A}_l}. \tag{3.37}$$

Here, c_{A} denotes the acceptor concentration and $W_{\mathrm{D_0A}_l}$ is the energy transfer rate from the donor at location 0 to the acceptor at location l. Fast migration occurs for all ratios of C_{DD}-C_{DA} at very short timescales ($t < t_1$) after excitation. During this time interval, the luminescent decay of the donor ions is single exponential.

The Hopping Model ($C_{\mathrm{DD}} \geq C_{\mathrm{DA}}$)

Burshtein described the migration of excitation energy as a random-walk across donors [Bur72]. After each transfer process ("hop"), the excitation energy stays for a characteristic time (τ_{hop}) at the actual donor. Watts [Wat75] showed that

$$\frac{1}{\tau_{\mathrm{hop}}} = \left(\frac{2\pi}{3}\right)^3 n_{\mathrm{D}}^2 C_{\mathrm{DD}}. \tag{3.38}$$

For sufficiently long times ($t > t_2$) the effects of direct D-A transfer are of minor importance and the radiative decay of the donor luminescence follows the equation [Bur72, Vor76]

$$I(t) = I_0 \cdot \exp\left(-\frac{t}{\tau_{\mathrm{R}}} - W_{\mathrm{DD}}^{\mathrm{hop}} \cdot t\right). \tag{3.39}$$

with

$$W_{\mathrm{DD}}^{\mathrm{hop}} = \pi \left(\frac{2\pi}{3}\right)^{5/2} n_{\mathrm{A}} n_{\mathrm{D}} (C_{\mathrm{DA}} C_{\mathrm{DD}})^{1/2}. \tag{3.40}$$

Here, n_{A} and n_{D} denote the donor and acceptor ion densities. The time t_2 can be calculated by

$$t_2 = \left(\frac{\gamma_{\mathrm{i}}}{W_{\mathrm{DA}}}\right)^2 \tag{3.41}$$

γ_{i} is defined in Equation 3.29.

The Diffusion Model ($C_{\mathrm{DD}} \ll C_{\mathrm{DA}}$)

Yokota and Tanimoto described the energy transfer between two donors as a diffusion process [Yok67]:

$$\frac{\partial \Psi(R,t)}{\partial t} = -\frac{1}{\tau_R}\Psi(R,t) + D\nabla^2\Psi(R,t) - \sum_i W_{\mathrm{DA}}(R - R_i)\Psi(R,t) \tag{3.42}$$

Ψ denotes the density of excited donors and D is the diffusion constant. Further details regarding the diffusion model can be found in the publication by Yokota et al. [Yok67] and the book of Henderson and Imbusch [Hen89], but will not discussed here.

The solution of this equation is not single exponential in the beginning, but for sufficiently long times ($t > t_2$, see Equation 3.41), the donor luminescence follows the equation

$$I(t) = I_0 \cdot \exp\left(-\frac{t}{\tau_{\mathrm{R}}} - W_{\mathrm{DD}}^{\mathrm{dif}} \cdot t\right). \tag{3.43}$$

$$W_{\mathrm{DD}}^{\mathrm{dif}} = \frac{(4\pi)^2}{3}\left(\frac{1}{2}\right)^{3/4} n_{\mathrm{A}} n_{\mathrm{D}} C_{\mathrm{DA}}^{1/4} C_{\mathrm{DD}}^{3/4} \tag{3.44}$$

As in case of the hopping model, the decay rate is proportional to the donor and acceptor concentration, n_{D} and n_{A}, respectively.

3.2 Measurement Setup

In this section, relevant information about the used setups for absorption-, emission-, ESA- as well as lifetime measurements will be introduced, briefly.

3.2.1 Absorption Measurements

Room temperature measurements of GSA were performed using the two-channel spectrophotometer CARY supplied by Varian. The spectral resolution was chosen according to the spectral linewidths and set to 0.15 nm for the anisotropic crystals BYF, YLF, and LLF and to 0.3 nm in case of KYF to obtain accurate transmission data. Applying Beer-Lambert's law (Eqn. 3.7), the measured transmission curves in the spectral range from 400 nm to 650 nm were converted to absorption cross-sections using the Pr^{3+}-ion density. The results of the room temperature measurements can be found in Section 3.3.1.

Additionally, GSA measurements on YLF and LLF were performed at low temperatures. The setup for these measurements is shown in Figure 3.5. A cryostatic temperature regulator was used to cool down the samples to approximately 10 K. In order to keep the low temperature of the sample, the light intensity was reduced by an appropriate aperture. The transmitted light of a tungsten halogen lamp was spectrally resolved using a 1 m SPEX monochromator. Due to the reduced linewidth of many optical transitions at 10 K, the spectral resolution was set to 0.03 nm. For signal detection, a cooled Silicon diode was used. The reference spectrum was recorded after removing the sample from the cryostatic chamber. These measurements were done using lock-in technology.

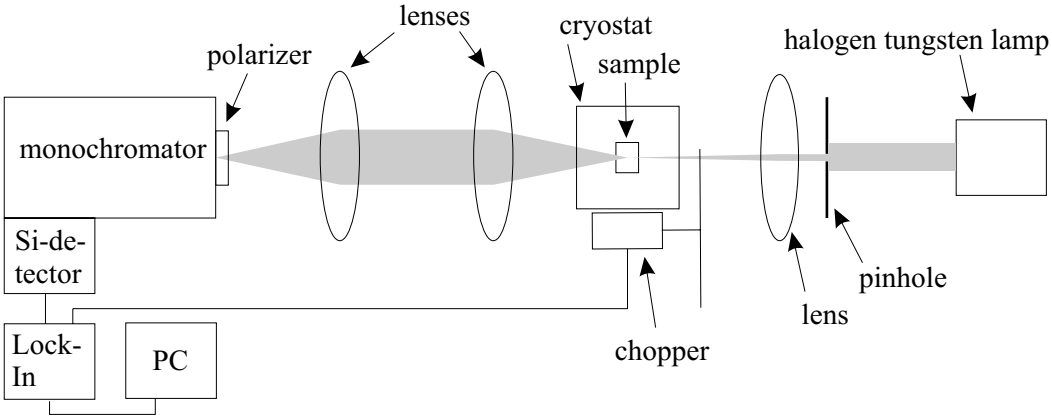

Figure 3.5: Schematic of the setup used in the low temperature absorption measurements

3.2.2 Emission Measurements

Both, room temperature as well as low temperature emission measurements were performend in the setup shown in Figure 3.6. As excitation source, a GaN-laser diode operated at 444 nm or, in case of some low temperature measurements, a frequency doubled optically pumped semiconductor laser (OPSL) emitting at 479.5 nm was employed. The crystal was prevented from heating at low temperature measurements by reducing the power of the excitation sources to 6 mW. To determine the spectral response of the setup, a tungsten filament lamp ($T = 2600$ K) was mounted at the sample position instead. Assuming an emissivity of a black body, the correction data can be determined by dividing the theoretical and the measured spectrum. The resulting emission cross-sections were determined using the Füchtbauer-Ladenburg formula [Wal98, Sch02].

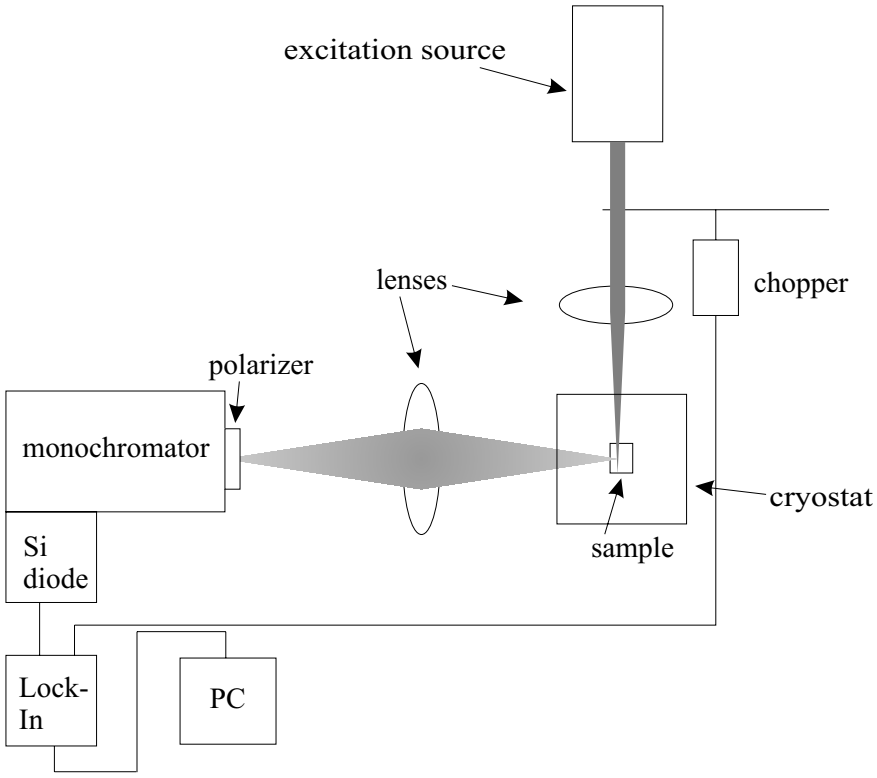

Figure 3.6: Schematic of the setup used in the low temperature emission measurements

3.2.3 Excited State Absorption Measurements

In the framework of this thesis continuous wave ESA spectra were recorded using the "pump- and probe"-technique first reported by Köttke et *al.* [Koe95]. Thereby, depending on the excitation wavelength, ESA originating from different energy levels can be

investigated. Figure 3.7 shows the setup used in the experiments. The pump beam was provided by a GaN-laser diode or optionally by a frequency doubled OPSL while the broad band probe beam is generated by a xenon lamp. The transmitted light is dispersed and analysed using a 1 m monochromator and a photomultiplier tube. Two choppers are used to modulate the pump and the probe beams and two lock-in amplifiers measure the transmitted light signals. The probe chopper signal triggers the first lock-in amplifier, which results in a measurement of the intensity I of the transmitted light. This signal is transferred into the second lock-in amplifier, which is triggered by the pump chopper. In this way the second lock-in amplifier measures the difference in transmission in pumped and unpumped condition ΔI.

The reduced population numbers of the ground state in presence of the laser excitation results in a variation of the absorbed light. Additionally, the population of the excited states causes ESA and stimulated emission.

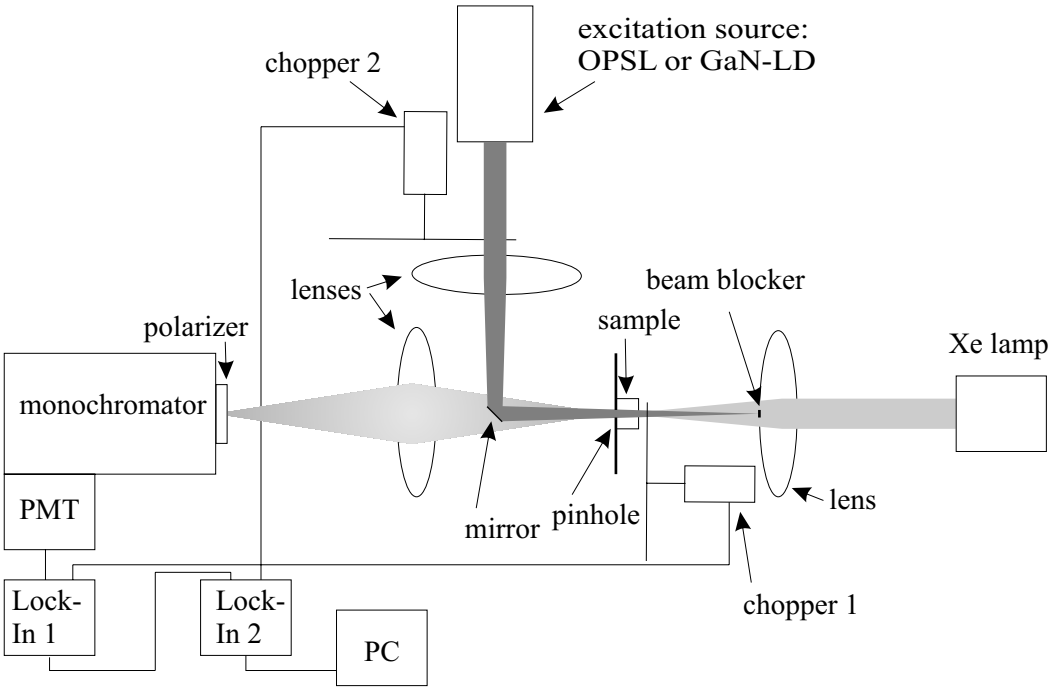

Figure 3.7: Schematic of the setup used in the ESA-measurements

The signal in the case of the unpumped crystal I_u can be described by Beer-Lambert's law (cf. Equation 3.7):

$$I_\mathrm{u} = I_0 \exp\left(-\sigma_\mathrm{GSA} n l\right) \tag{3.45}$$

where n denotes the total dopant ion concentration, l is the thickness of the sample, and σ_GSA is the GSA cross-section. The transmitted probe intensity by the pumped sample

I_p is given by

$$I_\mathrm{p} = I_0 \exp\left(-\sigma_\mathrm{GSA}(n-n_\mathrm{e})l + \sum_i \frac{n_i}{n_\mathrm{e}}(\sigma_{\mathrm{em},i} - \sigma_{\mathrm{ESA},i})n_\mathrm{e} l\right) \tag{3.46}$$

where n_i is the population density of level i ($\sum_i n_\mathrm{i} = n_\mathrm{e}$), and n_e denotes the total excited population density. $\sigma_{\mathrm{em},i}$ and $\sigma_{\mathrm{ESA},i}$ are the stimulated emission and the ESA cross-sections from level i, respectively. Forming the ratio of Equations 3.45 and 3.46 and subsequently taking the logarithm one obtains

$$\ln\left(\frac{I_\mathrm{p}}{I_\mathrm{u}}\right) = \sigma_\mathrm{GSA} n_\mathrm{e} l + \sum_i n_i(\sigma_{\mathrm{em},i} - \sigma_{\mathrm{ESA},i})l \tag{3.47}$$

where the term $\sigma_\mathrm{GSA} n_\mathrm{e} l$ represents the bleaching of the GSA due to the excited ions.

The frequencies of the choppers and the integration time constant of the lock-in amplifiers have to be chosen accurately in order to assure a good signal-to-noise ratio. Using a lamp as an excitation source results in a small population density of the excited state and, thus, slightly different transmission spectra of the pumped and unpumped case are obtained. The integration time constant of the first lock-in amplifier must be at least three times shorter than half a cycle of the pump chopper frequency. As a consequence, the frequency of the probe chopper must be high enough to allow operation with short integration time. Finally, the frequency of the pump chopper must be slow enough to provide steady state excitation of all levels.

In case of the investigated Pr^{3+}:YLF and Pr^{3+}:LLF samples the probe chopper frequency f_probe was set to 675 Hz and integration time constant of the first lock-in amplifier was $t_\mathrm{probe} = 30$ ms. The pump chopper was operated at $f_\mathrm{pump} = 10$ Hz which means a pump time (half cycle) of 50 ms that is 1.6 times longer than t_probe.

As the difference $\Delta I = I_\mathrm{p}$-I_u is very small, the following approximation can be made:

$$\ln\left(\frac{I_\mathrm{p}}{I_\mathrm{u}}\right) = \ln\left(1 + \frac{I_\mathrm{p} - I_\mathrm{u}}{I_\mathrm{u}}\right) = \ln\left(1 + \frac{\Delta I}{I_\mathrm{u}}\right) \approx \frac{\Delta I}{I}. \tag{3.48}$$

One of the advantages of the double-modulation technique is the acquisition of both I_p and I_u at the same time avoiding errors due to drifts of the probe beam. This results in a good reproducibility of the measurements. The output of the second lock-in must be rescaled according to the amplification factor of the amplifier A, to obtain ΔI from the measured signal $A\Delta I$. Using equation 3.48, the expression for the measured signal $\frac{\Delta I}{I}$ is then given by

$$\frac{\Delta I}{I} = (n_\mathrm{e} l A)\left(\sigma_{GSA} + \sum_i \frac{n_i}{n_\mathrm{e}}\left(\sigma_{\mathrm{em},i} - \sigma_{\mathrm{ESA},i}\right)\right). \tag{3.49}$$

For the determination of the cross-sections values the knowledge of A and n_e is not required. Since the raw spectra can be calibrated with the bleaching signal of the GSA, a wavelength region where only GSA occurs is sufficient to obtain the factor $n_e l A$. In this way, the measured ESA spectrum can be rescaled accordingly. To remove the influence of GSA, subtraction of the GSA spectrum from the scaled ESA spectrum results in

$$\sum_i (n_i/n_e)(\sigma_{em,i} - \sigma_{ESA,i}). \tag{3.50}$$

3.2.4 Lifetime Measurements

Figure 3.8 shows the setup used in the decay measurements. The excitation source is a pulsed optical parametric oscillator (OPO) tunable from 400 nm to 2.1 µm. This laser fabricated by Solar Laser System provides pulse durations of 30 ns and pulse energies up to 15 mJ at a repetition rate of 10 Hz. The fluorescence signal was spectrally resolved using a 0.5 m SPEX monochromator and detected by a S1 photomultiplier tube. To achieve a high resolution in timescales, the PMT was connected directly to a 0.5 GHz oscilloscope with a 50 Ω resistor inside. Under these conditions, time constants of up to 5 ns are detectable. If not stated elsewhere, an average of 3000 decay curves was taken for each measurement.

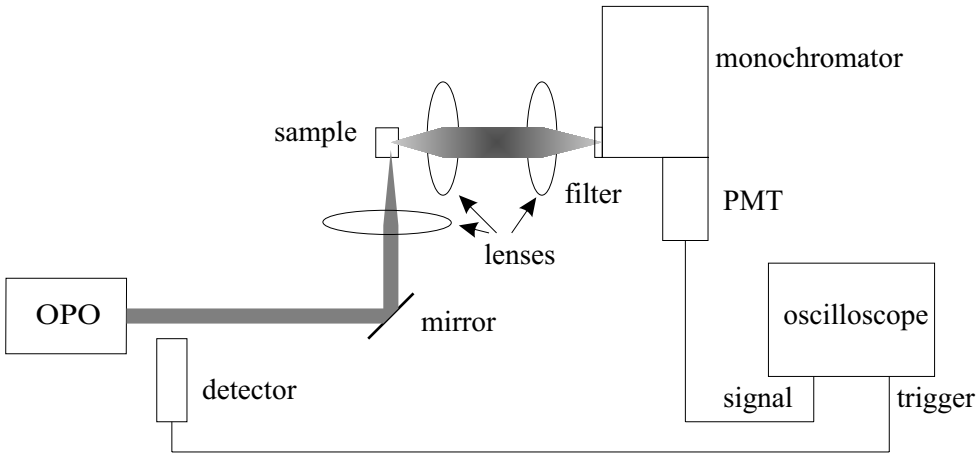

Figure 3.8: Schematic of the setup used in the decay measurements

3.3 Room Temperature Results

In this section spectroscopic data of the Pr-doped fluorides obtained from room temperature measurements are presented. Results of absorption and emission measurements in these materials were published earlier [Est79, Ada85, San94b, Osi03a, Cor07, Cam07, Ric07]. These data are presented in the following section. The continuous wave ESA spectra and results of the lifetime measurements are discussed in Sections 3.3.2 and 3.3.3, respectively.

3.3.1 Absorption and Emission Measurements

The results of the room temperature absorption measurements are displayed in Figure 3.9. Table 3.1 contains the peak absorption cross-sections of the investigated Pr^{3+}-doped crystal systems. In the anisotropic single crystals Pr^{3+}-ions feature peak absorption cross-sections of up to $2.3\times10^{-19}\,cm^2$ at a wavelength of 479.2 nm and a peak width of 0.65 nm. The OPSL-pump systems used in the laser experiments are spectrally matched to this absorption peak. In contrast to the OPSLs, GaN-based laser diodes (GaN-LDs) emitting in the spectral range around 444 nm are spectrally broader and feature a small tunability range. In this spectral region the peak absorption cross-section reaches $1.0\times10^{-19}\,cm^2$ and the peak width is at least 1.8 nm which is advantageous for diode-pumped laser experiments.

The results of the emission measurements in the visible spectral range under GaN-LD-excitation in case of Pr^{3+}:YLF, Pr^{3+}:LLF, and Pr^{3+}:KYF and Ar-ion laser excitation in case of Pr^{3+}:BYF are shown in Figure 3.10. Like in case of absorption, the emission transitions of Pr^{3+}:LLF and Pr^{3+}:YLF are strongly polarized and feature the same characteristics. The dominant transition of emission $^3P_0\rightarrow{}^3F_2$ around 640 nm has a peak emission cross-section of more than $2.1\times10^{-19}\,cm^2$. The strongest transitions are $^3P_0\rightarrow{}^3H_4$ ($\approx$ 479.2 nm), $^3P_0\rightarrow{}^3H_6$ ($\approx$ 604.2 nm - $\approx$ 607.1 nm), $^3P_0\rightarrow{}^3F_4$ ($\approx$ 721.0 nm), $^3P_0\rightarrow{}^3F_3$ ($\approx$ 697.7 nm) and $^3P_1\rightarrow{}^3H_5$ ($\approx$ 522.6 nm) in decreasing order. Laser action under GaN-LD-pumping has been demonstrated on these transitions except those at $\approx$ 697.7 nm and $\approx$ 479.2 nm.
The emission spectra of Pr^{3+}:BYF differ both in peak heights as well as in the peak wavelengths. The highest emission cross-section of $1.8\times10^{-19}\,cm^2$ is located at 607.6 nm (transition $^3P_0\rightarrow{}^3H_6$), followed by peaks at 480.3 nm ($^3P_0\rightarrow{}^3H_4$), 719.7 nm ($^3P_0\rightarrow{}^3F_4$), 639.4 nm and 642.7 nm ($^3P_0\rightarrow{}^3F_2$), 694.2 nm ($^3P_0\rightarrow{}^3F_3$), and 523.9 nm ($^3P_1\rightarrow{}^3H_5$).
The last emission spectrum shown in Figure 3.10 is obtained from Pr^{3+} in KYF. This system features emission cross-sections up to $0.9\times10^{-19}\,cm^2$. Besides the ground state transition, the strongest emission occurs at 644.9 nm ($^3P_0\rightarrow{}^3F_2$), where laser oscillation under GaN-LD-excitation was reported recently [Bra07, Cam07].

All emission spectra show a broad background of emission in the spectral regions from 595 nm to 630 nm and from 680 nm to 730 nm. The energy level structure of Pr^{3+} does not predict such broad optical transitions in emission but a few spectrally narrow transitions

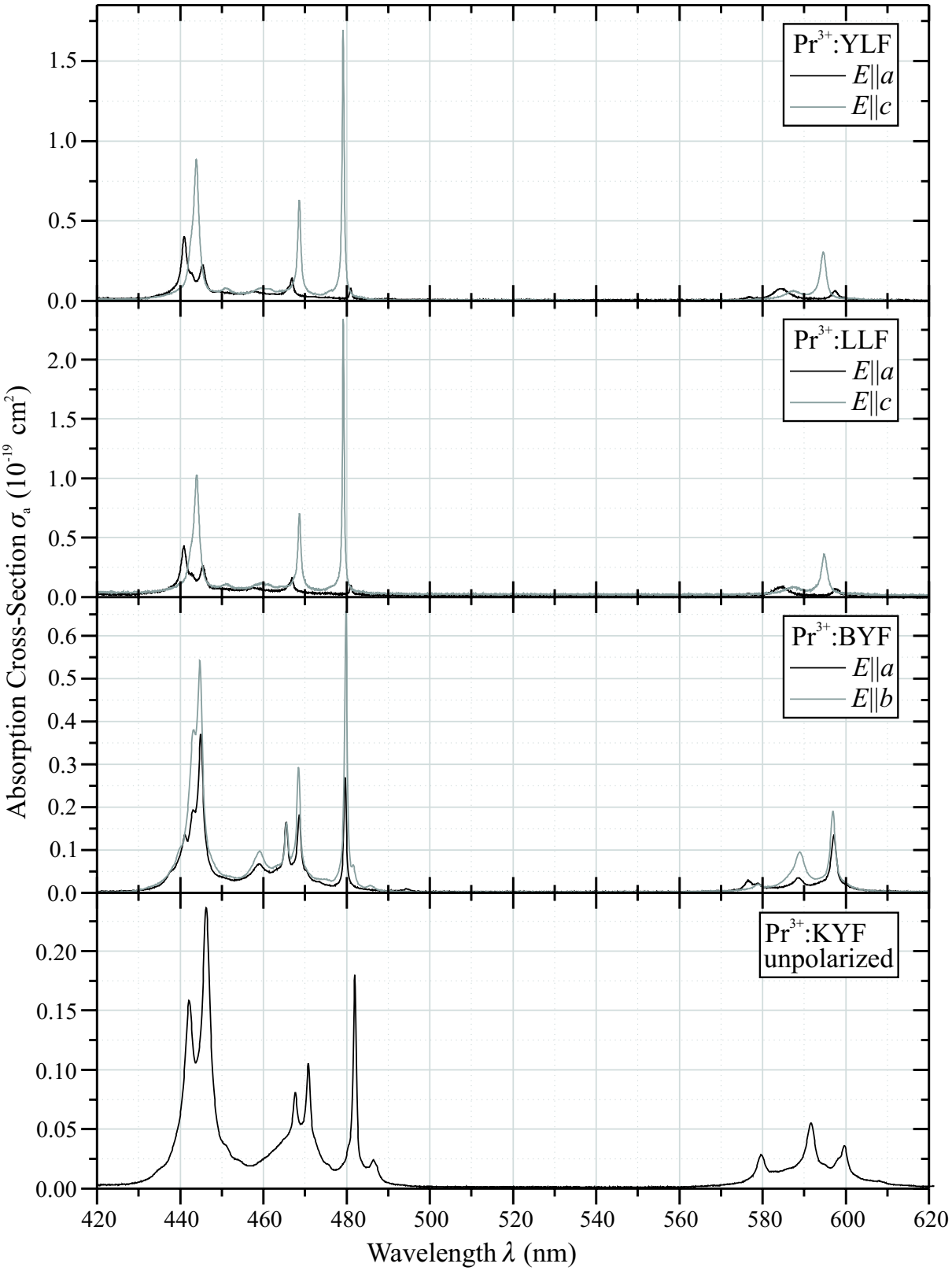

Figure 3.9: Room temperature polarized absorption spectra of different Pr^{3+}-doped fluorides

λ (nm)	σ_a (10^{-20} cm^2)	Polarization	Transition
YLF			
441.0	4.1	$\vec{E}\|\vec{a}$	$^3H_4 \rightarrow {}^3P_2$
443.9	8.9	$\vec{E}\|\vec{c}$	$^3H_4 \rightarrow {}^3P_2$
468.6	6.3	$\vec{E}\|\vec{c}$	$^3H_4 \rightarrow {}^3P_1$
479.2	17.0	$\vec{E}\|\vec{c}$	$^3H_4 \rightarrow {}^3P_0$
584.7	0.7	$\vec{E}\|\vec{a}$	$^3H_4 \rightarrow {}^1D_2$
594.6	3.1	$\vec{E}\|\vec{c}$	$^3H_4 \rightarrow {}^1D_2$
LLF			
440.9	4.3	$\vec{E}\|\vec{a}$	$^3H_4 \rightarrow {}^3P_2$
444.0	10.3	$\vec{E}\|\vec{c}$	$^3H_4 \rightarrow {}^3P_2$
468.7	7.1	$\vec{E}\|\vec{c}$	$^3H_4 \rightarrow {}^3P_1$
479.2	23.4	$\vec{E}\|\vec{c}$	$^3H_4 \rightarrow {}^3P_0$
584.4	0.8	$\vec{E}\|\vec{a}$	$^3H_4 \rightarrow {}^1D_2$
594.8	3.6	$\vec{E}\|\vec{c}$	$^3H_4 \rightarrow {}^1D_2$
BYF			
444.7	5.4	$\vec{E}\|\vec{b}$	$^3H_4 \rightarrow {}^3P_2$
468.4	2.9	$\vec{E}\|\vec{b}$	$^3H_4 \rightarrow {}^3P_1$
479.8	6.6	$\vec{E}\|\vec{b}$	$^3H_4 \rightarrow {}^3P_0$
589.0	1.0	$\vec{E}\|\vec{b}$	$^3H_4 \rightarrow {}^1D_2$
596.9	1.9	$\vec{E}\|\vec{b}$	$^3H_4 \rightarrow {}^1D_2$
KYF			
442.1	1.6		$^3H_4 \rightarrow {}^3P_2$
446.2	2.4		$^3H_4 \rightarrow {}^3P_2$
467.7	0.8		$^3H_4 \rightarrow {}^3P_1$
470.8	1.1		$^3H_4 \rightarrow {}^3P_1$
482.0	1.8		$^3H_4 \rightarrow {}^3P_0$
579.6	0.3		$^3H_4 \rightarrow {}^1D_2$
591.7	0.6		$^3H_4 \rightarrow {}^1D_2$
599.7	0.4		$^3H_4 \rightarrow {}^1D_2$

Table 3.1: Peak absorption cross-sections of GSA to the $^3\mathrm{P}_J$-manifold and the $^1D_2$ energy level of Pr^{3+} in different fluoride crystals

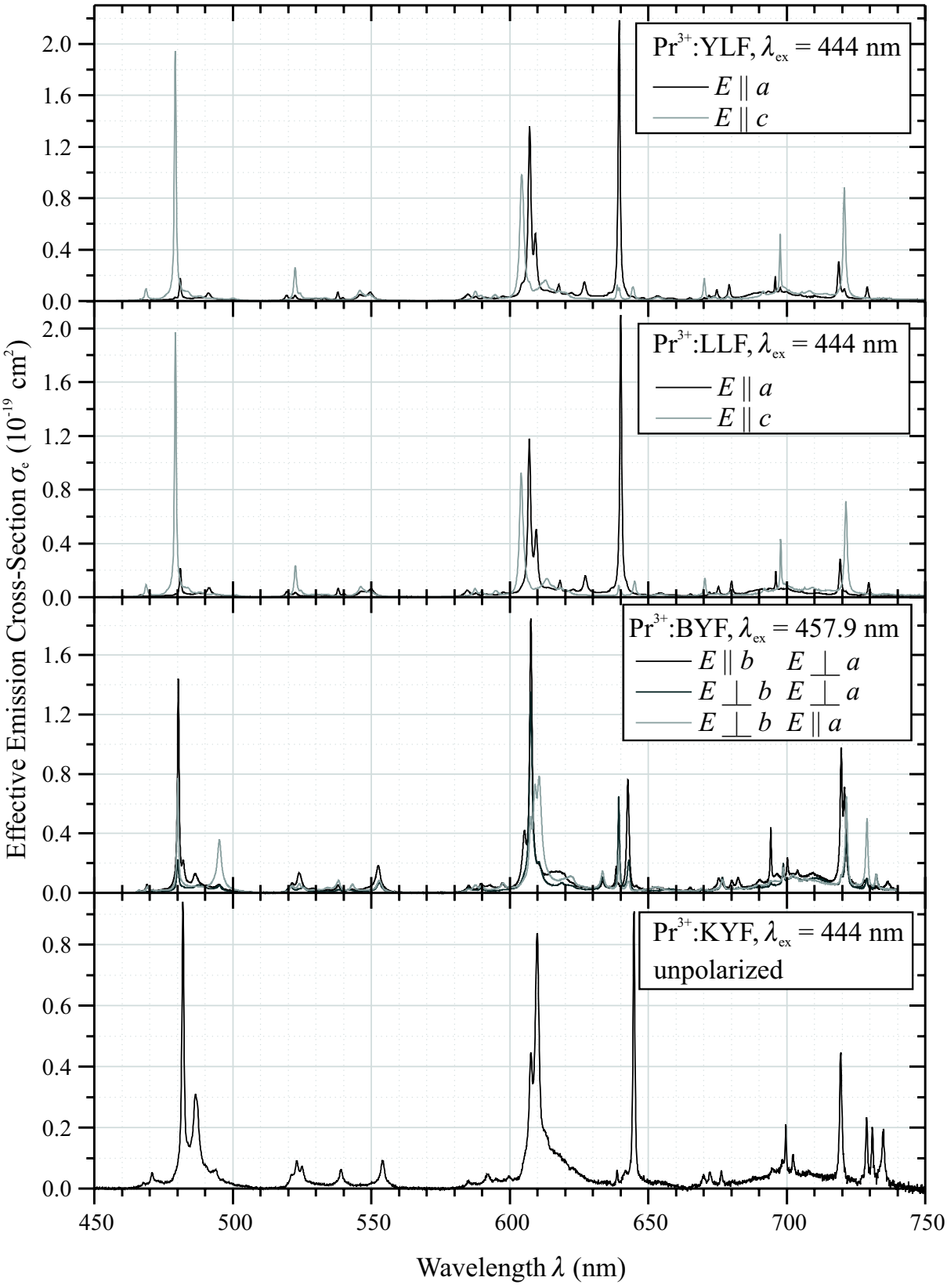

Figure 3.10: Room temperature polarized emission spectra of different Pr^{3+}-doped fluorides using a GaN-LD (YLF, LLF, and KYF) or an Ar-ion laser (BYF) as excitation source

λ (nm)	σ_e (10^{-20} cm^2)	Polarization	Terminating Level
YLF			
479.2	19.4	$\vec{E}\|\vec{c}$	$^3H_4$
604.3	9.8	$\vec{E}\|\vec{c}$	$^3H_6$
607.2	13.6	$\vec{E}\|\vec{a}$	$^3H_6$
639.5	21.8	$\vec{E}\|\vec{a}$	$^3F_2$
697.6	5.2	$\vec{E}\|\vec{c}$	$^3F_3$
720.8	8.8	$\vec{E}\|\vec{c}$	$^3F_4$
LLF			
479.3	19.7	$\vec{E}\|\vec{c}$	$^3H_4$
604.1	9.3	$\vec{E}\|\vec{c}$	$^3H_6$
607.0	11.8	$\vec{E}\|\vec{a}$	$^3H_6$
640.1	21.0	$\vec{E}\|\vec{a}$	$^3F_2$
697.8	4.3	$\vec{E}\|\vec{c}$	$^3F_3$
721.4	7.2	$\vec{E}\|\vec{c}$	$^3F_4$
BYF			
480.3	14.4	$\vec{E}\|\vec{b}$	$^3H_4$
607.6	18.5	$\vec{E}\|\vec{b}$	$^3H_6$
610.6	7.9	$\vec{E}\|\vec{a}$	$^3H_6$
639.4	6.5	$\vec{E}\perp\vec{a}, \vec{E}\perp\vec{b}$	$^3F_2$
642.7	7.6	$\vec{E}\|\vec{b}$	$^3F_2$
694.2	4.4	$\vec{E}\|\vec{b}$	$^3F_3$
719.7	9.8	$\vec{E}\|\vec{b}$	$^3F_4$
721.6	6.5	$\vec{E}\|\vec{a}$	$^3F_4$
729.0	5.0	$\vec{E}\|\vec{a}$	$^3F_4$
KYF			
482.0	9.4		$^3H_4$
609.9	8.4		$^3H_6$
644.9	9.1		$^3F_2$
699.6	2.1		$^3F_3$
719.5	4.5		$^3F_4$
728.9	2.3		$^3F_4$
730.9	2.0		$^3F_4$
734.9	2.0		$^3F_4$

Table 3.2: Peak emission cross-sections of the strongest transitions originating from the $^3P_0$-energy level of Pr^{3+} in different fluoride crystals

in these regions. Regarding the broad absorption background in the spectral region from 430 nm to 485 nm, colour centre formation in the investigated materials is possible. Colour centres feature broad bands of absorption and emission in the visible spectral region. Further investigations on colour centres were not performed in this thesis but should be considered in the future. As expected from the crystallographic point of view, the optical spectra of Pr^{3+}:YLF and Pr^{3+}:LLF feature the same characteristics.

3.3.2 Excited State Absorption

The set-up used for the ESA measurements introduced in Section 3.2.3 allowed the measurement of excited state absorption from 280 nm to 750 nm. By using GaN-LDs as well as OPSLs, ESA spectra originating from the $^3P_0$-level of of Pr^{3+}:$LiYF_4$ and Pr^{3+}:$LiLuF_4$ were recorded. Figures 3.11 and 3.12 show the obtained spectra. The following paragraph gives a short discussion on the results.

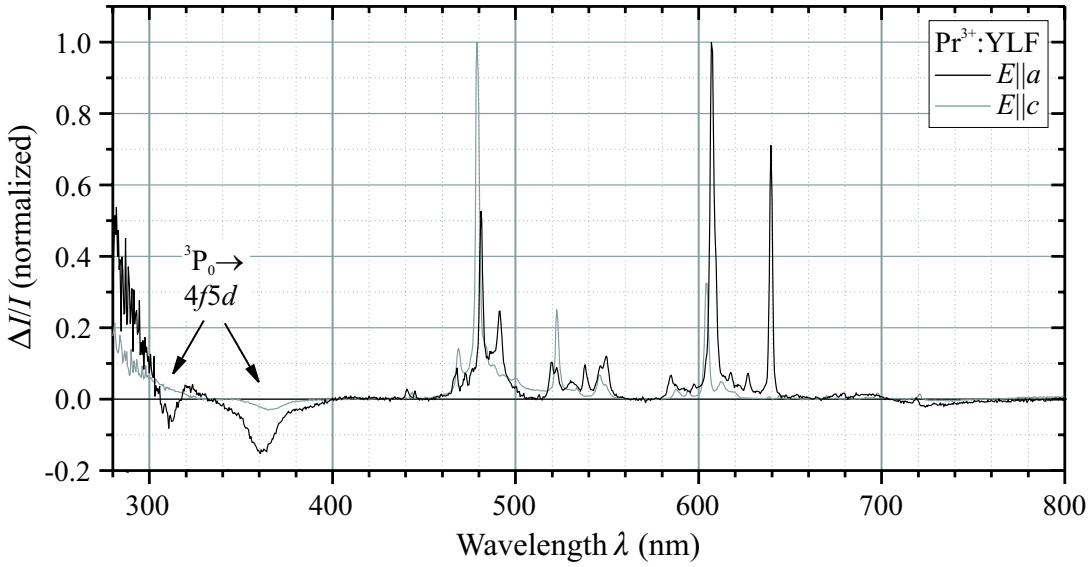

Figure 3.11: Polarized ESA-spectra in the ultraviolet and visible spectral range. In the indicated wavelength regions ESA transitions from the $^3P_0$ to the $4f5d$-states are expected.

In principle, the spectra can be divided in two sections: the first one, covering the spectral range from 280 nm to 410 nm, is dominated by ESA. The absorption lines are broad ($\Delta\lambda \geq$ 20 nm) and can be assigned to different ESA transitions from the $^3P_0$ to different $4f5d$-states of Pr^{3+} [San94a, Sar94, Lar99, Lar00, Nic01]. The second part, corresponding to the visible spectral region from 440 nm to 750 nm, is dominated by the stimulated emission originating from the ^3P_J-multiplet as well as the $^1D_2$ energy level. In the spectral region from 695 nm to 750 nm, the characteristic emission transitions $^3P_0 \rightarrow {}^3F_3$ and $^3P_0 \rightarrow {}^3F_4$ were not detected. Instead, a broad ESA background has been has been recorded here.

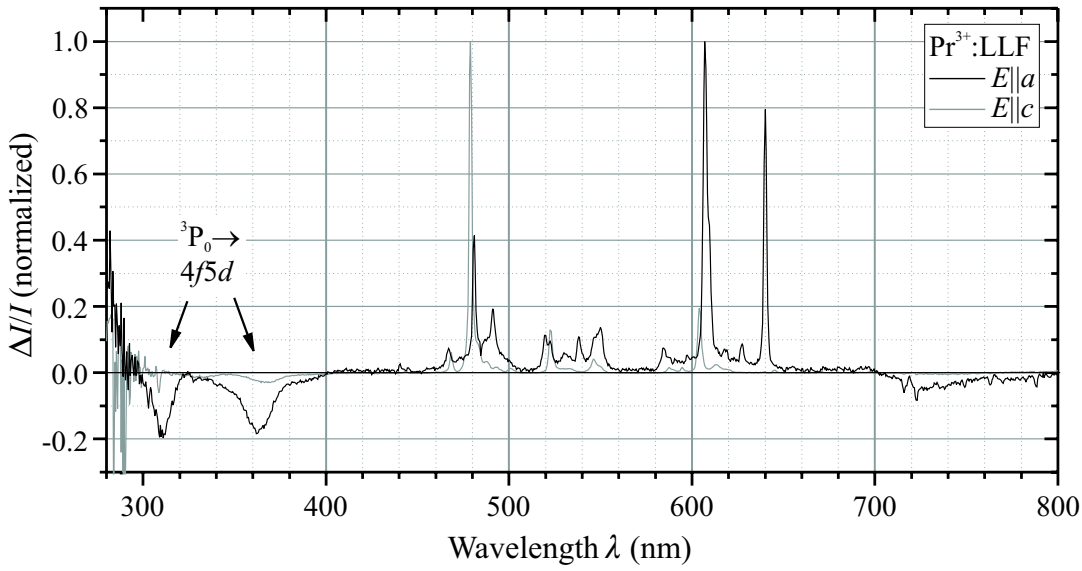

Figure 3.12: Polarized ESA-spectra in the ultraviolet and visible spectral range. ESA transitions from the $^3P_0$ to the $4f5d$-states are induced by photons in the indicated wavelength regions.

The reason for this is not clear. According to the energy level scheme, no narrow absorption lines around 698 nm and 721 nm should occur suppressing the emission transitions into the $^3F_3$ and $^3F_4$ energy levels. Furthermore, no ESA transitions from the $^3P_0$ to the $4f5d$ states are expected in this spectral region. Although the population of the $4f5d$ states is very low, ESA inside these energy states was checked by measuring the ESA spectrum with an appropriate filter blocking the UV-components from the pump beam responsible for the ESA transitions $^3P_0 \rightarrow 4f5d$. However, no change has been found in this spectral region. Due to different setup components in comparison to [San94a] and [Ric04a], the limited spectral sensitivity of the applied photomultiplier tube is most likely the reason for the obtained data around 735 nm. In the former measurements, no laser transitions in the visible spectral range were subject to ESA-processes originating from the upper laser level.

Neither on the pump wavelengths of GaN-LDs (444.0 nm) and OPSLs (479.5 nm) nor on possible laser wavelengths, such as 639.5 nm, 607.2 nm, and 522.6 nm, no ESA occurs.

3.3.3 Lifetime Measurements

Pr^{3+} ions doped in single crystals often exhibit nonexponential fluorescence decay curves from the $^3P_0$-level. This occurs both in oxidic and fluoridic single crystals [Ada85, Mal93, Der03, Xio05]. In former publications, different authors found fluorescence originating from the $^1D_2$ under $^3P_0$-excitation [Heg82, Der03]. Population of the $^1D_2$-energy level can be generated via radiative or nonradiative transitions. In oxide host materials with high

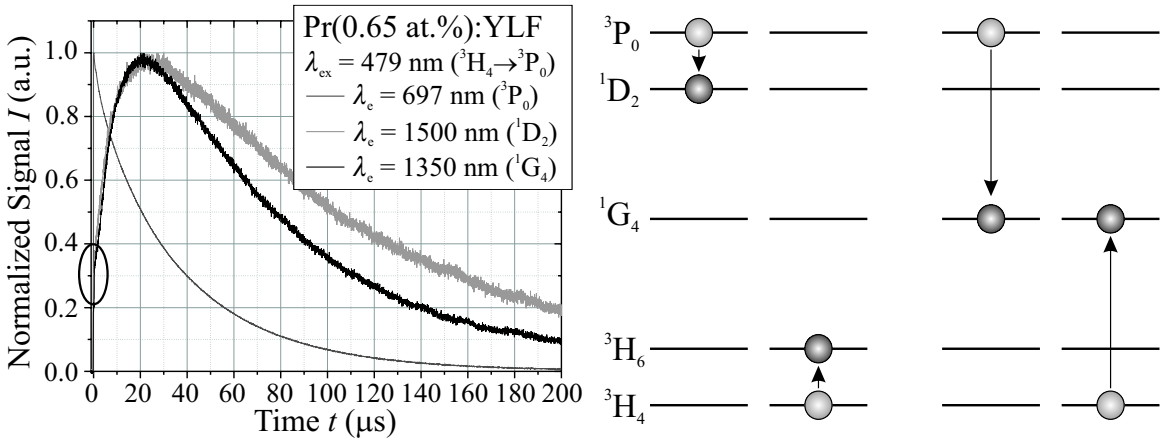

(a) (b)

Figure 3.13: (a) Pr^{3+}(0.65 at.%):YLF: decay characteristics under $^3P_0$-excitation (b) Cross-relaxation processes in the Pr^{3+}-system suggested by [Heg82] and [Der03]

phonon energies, the energy gap between $^3P_0$ and $^1D_2$ of $\approx 4000\,\mathrm{cm}^{-1}$ can be bridged by multi-phonon relaxations leading to an enhanced population of the $^1D_2$-state. This leads to a single exponential decay curve and a temperature dependence of the fluorescence decay rate. In case of low-phonon host materials like fluorides for very low concentrations no $^1D_2$ fluorescence and no temperature dependence of the fluorescent lifetime was detected [Ada85]. However, at reasonable high Pr^{3+}-concentrations nonexponential deexcitation curves and $^1D_2$-fluorescence is observed in these materials.

A direct evidence for energy transfer processes in Pr^{3+}-doped systems can be seen in Figure 3.13 (a) in case of a Pr^{3+}:YLF crystal with a Pr^{3+} concentration of 0.65 at.%, for example. The decay curves of the $^3P_0$, $^1D_2$ and $^1G_4$ are displayed in linear scale under $^3P_0$-excitation. The obtained characteristics show different behaviour: The $^3P_0$-fluorescence curve is nonexponential during the first 20 µs and exhibits a single exponential behaviour at larger timescales. This can be seen more clearly in the decay curve of the Pr^{3+}(0.65 at.%):YLF in semilogarithmic scale in Figure 3.15. The decays from $^1D_2$ and $^1G_4$ show different characteristics. The fluorescence intensity reaches its maximum value after 20 µs and decreases single exponentially for sufficiently long timescales. These results can be explained by the mechanisms shown in Figure 3.13 (b). Under $^3P_0$-excitation, excitation energy is transfered by CRPs to the $^1D_2$ and $^1G_4$ energy levels. Hegarty and Deren suggested the existence of these CRPs between adjacent Pr^{3+}-ions [Heg82, Der03]. In this process, Pr^{3+}-ions which are not excited are acting as acceptors.

The decay characteristics shown in Figure 3.14 (a) are taken under $^1D_2$-excitation. The $^1D_2$ fluorescence signal, ranging from the excitation pulse to about 75 µs is nonexponential

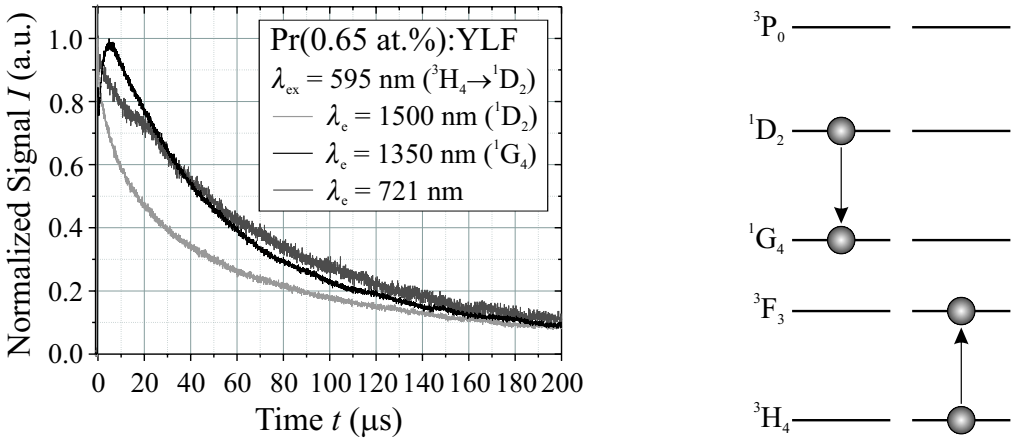

(a) (b)

Figure 3.14: (a) Pr^{3+}(0.65 at.%):YLF: decay characteristics under $^1D_2$-excitation (b) Additional energy transfer process detected in Pr^{3+}:YLF

and passes into a single exponential behaviour at $\approx 100\,\mu s$. In case of $^1D_2$-excitation, fluorescence from the $^1G_4$ and at 721 nm could be detected as well. The decay curve of the $^1G_4$-level is shaped as in case of $^3P_0$-excitation, but with a shorter rise time of about 5 µs. The measured signal at 721 nm features an almost single exponential decay starting with the excitation pulse. These results add another CRP to the chart: This CRP originating from the $^1D_2$ enables even more population in the $^1G_4$ energy level. It is schematically depicted in Figure 3.14 (b). Considering the fluorescence decay curve at 721 nm, the decay constant differs from the one of Pr^{3+}-ions directly excited in the $^3P_0$ energy level. The fluorescence is most likely not originating from the $^3P_0$ energy level, because any ETU process leading to a population of the $^3P_0$ is far from resonance as well as high excitation intensities and two closely spaced excited Pr^{3+}-ions are necessary to achieve ETU. Furthermore, these ions most likely loose their excitation energy by CRP after the ETU process. Thus, a fast deexcitation of the $^3P_0$-state is expected under $^1D_2$-excitation. This behaviour could not be confirmed by the measurements. The detected fluorescence might be the result of colour centres interacting with excited Pr^{3+} ions. A second aspect in the decay curves which is not explainable so far is the very fast increase in fluorescence originating form the $^1D_2$ and $^1G_4$ levels in Figures 3.13(a) and 3.14(a). After the initial increase, which is marked in Figure 3.13(a), these curves feature a curved behaviour. A simple CRP model predicts no very fast increase prior to the curved behaviour. The initial increase in fluorescence might be due to parasitic excitation of colour centres in the blue spectral region at 444 nm or 479.6 nm. Colour centres might also provide fractions of the fluorescence background around 700 nm in the room temperature emission spectra in Figure 3.10 as discussed in Section 3.3.1.

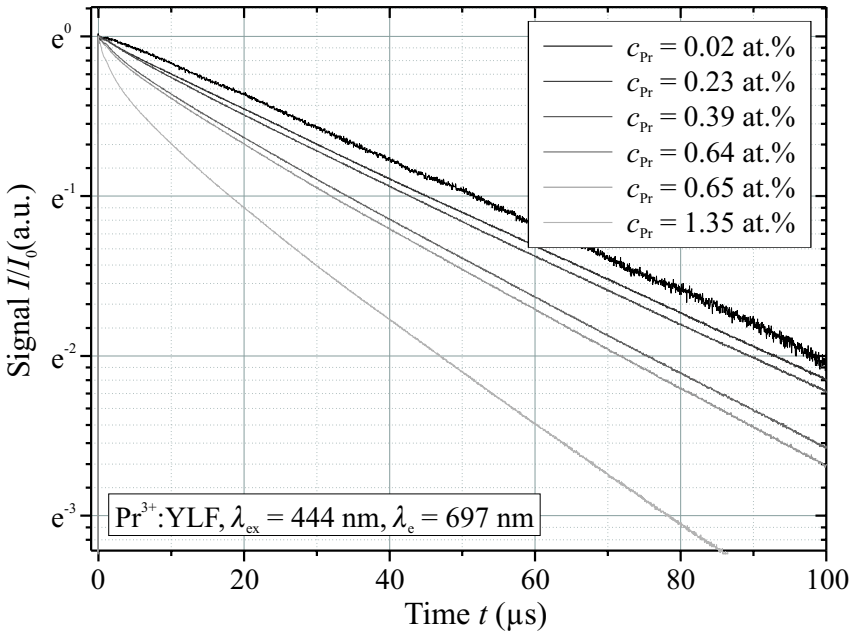

Figure 3.15: Decay curves of the $^3P_0$-level of Pr^{3+}:YLF under direct excitation

To obtain high energy transfer rates W_{DA} and W_{DD}, Pr^{3+} ions in the host lattice must be located at neighbouring RE-sites. Thus, the effect of fluorescence quenching by CRPs should increase with increasing Pr^{3+} concentration. The concentration dependence of the luminescent decay from the $^3P_0$ state of Pr^{3+}:YLF is shown in Figure 3.15. In semilogarithmic scale, the nonexponential behaviour of the decay curves during the first microseconds can be seen clearly. With increasing dopant concentration, the effect gains influence. Apart from the nonexponential decay at the beginning, the time constant in the single exponential regime shortens with increasing concentrations as well. As already discussed in Section 3.1.3, energy migration between donor ions affects the exponential behaviour for sufficiently long times after excitation. High energy migration rates enable exictation energy to reach more distant acceptors and fluorescence quenching can occur in longer timescales. This can be seen at the steeper slope at longer times.

While in case of single exponential decay curves the effective lifetime τ_{eff} can be determined by an exponential fit, the effective lifetime of nonexponential decay curves can be calculated by

$$\tau_{\mathrm{eff}} = \int_0^\infty I_0(t)dt \tag{3.51}$$

where $I_0(t)$ denotes the normalized decay curve. Table 3.3 shows the calculated effective lifetimes for different Pr-concentrations (c_{Pr}) as well as the nonradiative decay rate W_{nr} obtained by Equation 3.15. The radiative lifetime was estimated by the measured lifetime of a sample with the lowest doping level available.

c_{Pr} (at.%)	τ_{eff} (µs)	W_{nr} (10^3 s^{-1})
YLF	$\tau_{\mathrm{R}} \approx 50\,\mu\mathrm{s}$	
0.02	49.8	0.1
0.23	45.9	1.8
0.34	45.0	2.2
0.38	43.8	2.8
0.64	35.7	8.0
0.65	34.1	9.3
1.35	21.4	26.7
LLF	$\tau_{\mathrm{R}} \approx 50\mu\mathrm{s}$	
0.15	46.8	1.4
0.20	47.0	1.3
0.45	34.0	9.4
BYF	$\tau_{\mathrm{R}} \approx 47\,\mu\mathrm{s}$	
0.65	42.6	2.0
1.50	21.1	25.9
2.30	15.9	41.4
KYF	$\tau_{\mathrm{R}} \approx 48\,\mu\mathrm{s}$	
0.10	47.6	<0.1
0.20	46.0	0.7
0.70	43.1	2.2
2.00	24.1	20.5

Table 3.3: Measured $^3P_0$ decay parameters of Pr^{3+} in different fluoride crystals

Determination of the average number of interacting ions

According to Equation 3.15, the average nonradiative decay rate $W_{\mathrm{nr}} = 1/\tau_{\mathrm{nr}}$ can be calculated with the knowledge of the effective lifetime and the radiative lifetime. The order of W_{nr} with respect to the Pr^{3+} concentration can be obtained by a double logarithmic plot. Figure 3.16 shows this plot. The slope of a linear fit in this scale determines the order of the process responsible for the nonradiative decay. In case of all Pr^{3+} doped fluorides under investigation, the value is close to 2, indicating an energy transfer process where two Pr^{3+}-ions (a Pr^{3+}-"pair") are involved in the quenching processes.

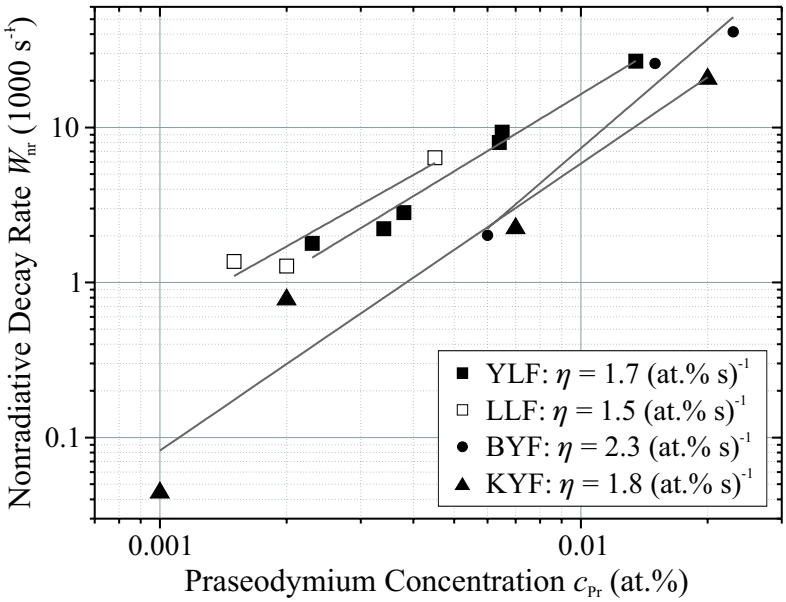

Figure 3.16: Concentration dependence of the nonradiative decay rate W_{nr} of the $^3P_0$-state of Pr^{3+}-ions in the different host materials

Determination of the Nature of Energy Transfer Processes

To determine the nature of the nonradiative decay, a more detailed decay analysis is necessary. This is possible by transforming the decay curve $I(t)$ to a concentration and lifetime independent form $v(t)$ [Kob73]. $I(t)$ has to be transformed according to

$$v(t) = -\frac{t/\tau_{\mathrm{R}} + \ln(I(t))}{c_{\mathrm{A}}}. \tag{3.52}$$

Figure 3.17 shows the measured data as well as the multipolar- and exchange-induced excitation energy transfer plots in a double logarithmic scale. It can be seen that the measured decay curve can not be explained by one coupling mechanism only. In fact, two mechanisms for excitation energy transfer are dominant: in the first interval from 0 to

$0.2{\cdot}\tau_R$, the measured decay curves can be approximated by exchange-induced CRPs, while dipole-dipole induced interaction dominates the decay characteristics in the following microseconds. Investigations on the Nd^{3+}:$Y_3Al_5O_{12}$ system had the same result [DT98]. The discrepancy between the slope of the theoretical and the measured curve is most likely resulting from the absence of energy migration processes in Equations 3.26 and 3.32.

Determination of the energy migration microparameters

In the first step, the energy migration rate induced by D-D excitation energy transfer W_{DD}^{dd} was determined using Equation 3.53. Fitting was performed from $2{\cdot}\tau_R$ to $4{\cdot}\tau_R$. Depending on the host material, the radiative lifetimes given in Table 3.3 were assumed.

$$I(t) = I_0 \cdot \exp\left(-\frac{t}{\tau_R} - W_{DD}t\right) \tag{3.53}$$

Table 3.5 gives the results from the fitting process as well as the calculated values of the microparameters regarding energy migration. The calculation was performed for the hopping model (Eqn. 3.40) as well as the diffusion model (Eqn. 3.44). With an increase in Pr^{3+}-concentration, the migration rate W_{DD} increases as well.

Discussion

This behaviour can be explained by a decrease in the mean distance between the ions with higher concentrations, which leads to higher energy migration rates and thus to a larger nonradiative deexcitation rate. The calculated energy transfer microparameters, C_{DD}^{hop} and C_{DD}^{dif}, give information about the regime of energy migration. Depending on the magnitude of C_{DA} and C_{DD}, the hopping mechanism or the diffusion model can be applied. As listed in Table 3.5, for low concentration levels the condition for the hopping model is fulfilled, while in case of high Pr^{3+}-concentrations, ambivalent results prevent a classification.

Determination of the Cross-Relaxation energy transfer microparameter

To obtain the microparameter regarding the dd-induced donor-acceptor energy transfer, C_{DA}^{dd}, two approaches were pursued:

In the first case, the equation by Inokuti and Hirayama, complemented by a single exponential factor $\exp(-W_{DD}t)$ taking into account the energy migration processes, was used to fit the decay curves in the time range between $0.2{\cdot}\tau_R$ and $2{\cdot}\tau_R$ (see Eqn. 3.28). Application of Equation 3.29 with the appropriate Pr^{3+}-ion density, $C_{DA,i}^{dd}$ is determined.

$$I(t) = I_0 \cdot \exp\left(-\frac{t}{\tau_R} - W_{DD}t - \gamma_i\sqrt{t}\right) \tag{3.54}$$

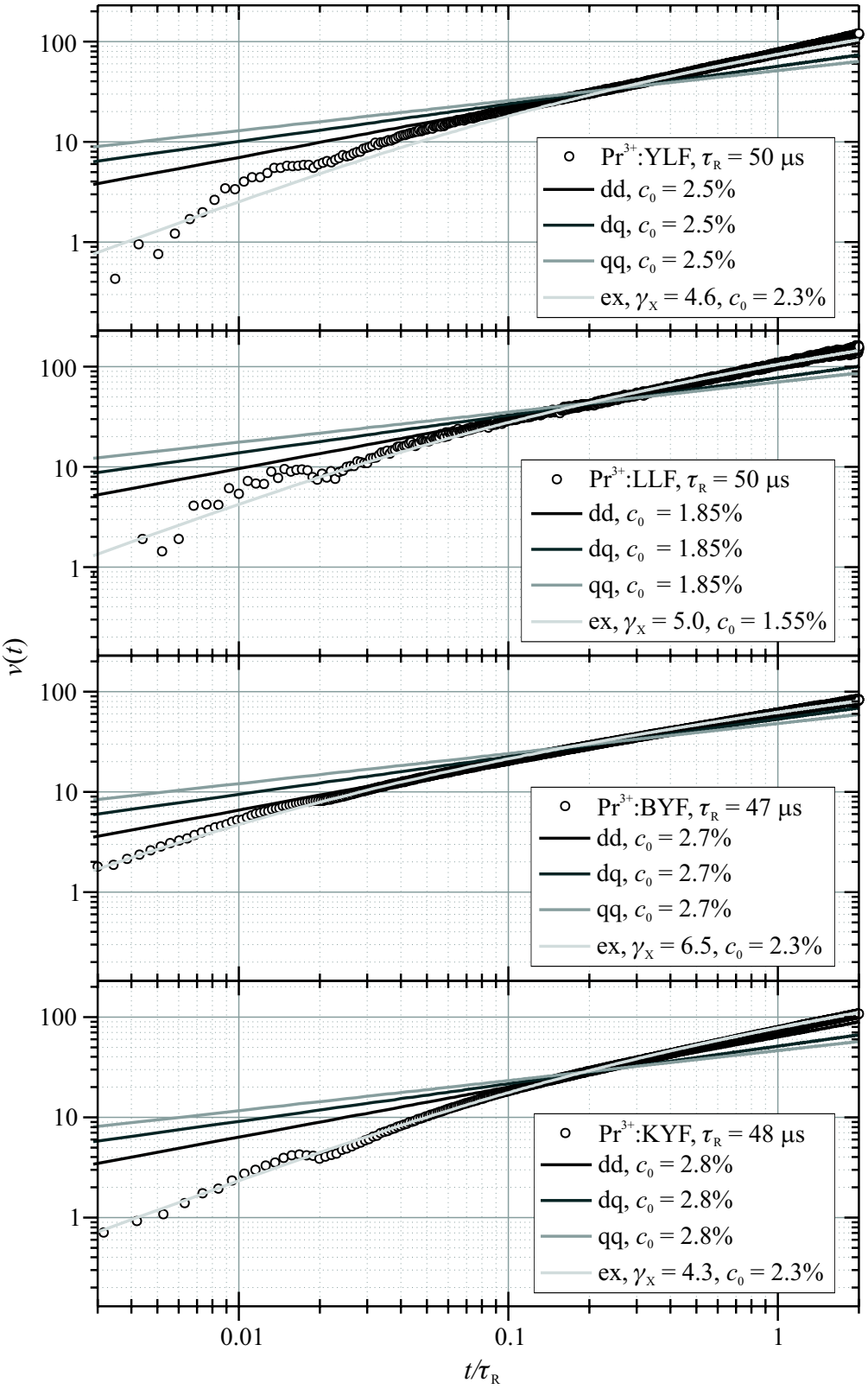

Figure 3.17: $v(t)$-plot for different mulitpolar and exchange processes as well as for the measured decay curves of Pr^{3+}-doped fluorides (dots)

The second approach is the direct calculation of the decay curve via Equation 3.25 for the time interval from $0.2{\cdot}\tau_{\mathrm{R}}$ to $2{\cdot}\tau_{\mathrm{R}}$. In analogy to Equation 3.54, the energy migration is considered by the exponential factor $\exp(-W_{\mathrm{DD}}t)$ resulting in

$$I(t) = I_0 \cdot \exp\left(-\frac{t}{\tau_{\mathrm{R}}} - W_{\mathrm{DD}}t\right) \prod_l \left(1 - c_{\mathrm{A}} + c_{\mathrm{A}} \exp(-W_{\mathrm{D_0A}_l} \cdot t)\right) \tag{3.55}$$

with

$$W_{\mathrm{D_0A}_l} = \frac{C_{\mathrm{DA,s}}^{\mathrm{dd}}}{R_{0l}^6}. \tag{3.56}$$

To calculate the decay curve directly, knowledge of the distance between rare earth ion sites as well as their orientation is required. Due to the minor importance of orientation [Blu81, Dok81], this aspect was neglected in the calculations. The distances between the Y^{3+} or Lu^{3+} lattice sites in YLF, LLF, BYF, and KYF were taken from [Tho61, Kam93b, Gui93, Pie74], respectively and calculated with the software included in the FindIt structural database. Taking into account neighbouring ions in a sphere of 30 Å, about 1300 crystal sites were included in the calculations. The fit of the decay curves using this model directly resulted in determination of the donor-acceptor energy transfer microparameter, $C_{\mathrm{DA,s}}^{\mathrm{dd}}$.

Table 3.4 contains the microparameters obtained by the continuum approximation and the direct calculation via summation. They are are in the range of some $10^{-39}\,\mathrm{cm^6 s^{-1}}$, and thus in the same order of magnitude as reported for Nd^{3+}-ions or Tm^{3+}-ions [Vor82, Sou02a, Sou02b]. In contrast to former reported results, the ratio between the results from the continuum approximation and the direct summation is small [Bur78].

From the theoretical point of view, $C_{\mathrm{DA}}^{\mathrm{dd}}$ should be independent of the donor and acceptor concentration. However, this is not confirmed by the experimental results. In a former study on energy transfer between Yb^{3+}-ions and other rare earths, Bolz realized this aspect, too [Bol01]. He suggested the reasons for this behaviour are upconversion as well as cross-relaxation processes or metastable levels from the acceptor ions which are not considered in the applied model.

A rough approximation of the maximal distance between two interacting ions can be made by equating the radiative decay rate τ_R^{-1} (3.11) and the cross-relaxation rate (3.56) resulting in

$$R_{\mathrm{C}} = (C_{\mathrm{DA}}^{\mathrm{dd}} \tau_{\mathrm{R}})^{1/6} \tag{3.57}$$

The radius R_{C} of the sphere, where the nonradiative decay rate is higher than the radiative decay rate and thus, quenching effects should be visible, is (71±6) Å, (82±11) Å, (67±16) Å, and 63 Å in case of YLF, LLF, BYF, and KYF, respectively. Assuming a homogeneous distribution of Pr^{3+}-ions occupying suitable host lattice sites, the spheres are occupied by more than one Pr^{3+}-ion at a concentration of 0.020 at.% in YLF, 0.013 at.%

c_{Pr} (at.%)	$C_{\mathrm{DA}}^{\mathrm{dd}}$ (continuum) (10^{-39} cm^6 s^{-1})	$C_{\mathrm{DA}}^{\mathrm{dd}}$ (summation) (10^{-39} cm^6 s^{-1})
YLF		
0.34	4.7	5.2
0.38	2.2	2.2
0.64	1.8	1.9
0.65	2.6	2.7
0.70	1.6	1.4
1.35	3.3	3.4
LLF		
0.15	3.4	3.9
0.20	3.0	3.4
0.45	10.5	14.1
BYF		
0.65	0.3	0.3
1.50	5.4	5.5
2.30	2.9	2.9
KYF		
2.00	1.2	1.4

Table 3.4: Calculated cross relaxation energy transfer microparameters (see text)

c_{Pr} (at.%)	W_{DD} (10^3 s^{-1})	$C_{DA,s}^{dd}$	C_{DD}^{hop}	C_{DD}^{dif} (10^{-39} cm^6 s^{-1})	Model
YLF					
0.34	0.7	5.2	5.2	13.0	hopping
0.38	1.2	2.2	22.5	25.8	hopping
0.64	3.3	1.9	24.7	25.9	hopping
0.65	3.9	2.7	22.3	27.4	hopping
0.70	4.5	1.4	43.2	41.4	hopping
1.35	8.6	3.4	4.7	10.4	hopping
LLF					
0.15	1.2	3.9	402	213	hopping
0.20	0.7	3.4	57.5	55.6	hopping
0.45	2.3	14.1	5.2	18.1	—
BYF					
0.65	0.8	0.3	9.5	7.4	hopping
1.50	6.9	5.5	1.5	5.7	—
2.30	9.7	2.9	1.0	3.6	—
KYF					
2.00	6.2	1.4	0.7	2.3	—

Table 3.5: Calculated energy migration microparameters (see text)

in LLF, and 0.025 at.% in BYF and KYF. This is in contrast to the experimental results. The mean concentration level where quenching processes are detectable is ≈0.3 at.% in case of YLF. Thus, the acqired energy transfer microparameters are too high, because the calculated concentration limits would predict cross-relaxation processes at concentration levels where the excited states still are decaying single exponentially.

Application of the Judd-Ofelt-Theory in case of the energy transfer ($^1I_6$, $^3H_4$) → ($^1D_2$, $^3H_6$) is possible, but not for the mechanism ($^3P_0$, $^3H_4$) → ($^1D_2$, $^3H_6$), because the reduced matrix elements of the transition ($^3P_0$ →$^1D_2$) equals zero. The resulting energy transfer microparameter C_{DA}^{dd} is 1.6×10^{-48} cm^{6}s^{-1}. This value is orders of magnitude lower than the results obtained by the fitting procedure and supports the considerations made before.

These large discrepancies can be explained by the distribution of the Pr^{3+}-ions inside the crystals. The formulas herein assume a homogeneous ion distribution. At least for YLF and LLF this is only a rough approximation. Further details will be given in the low temperature spectroscopy results in Section 3.4. Nevertheless, the parameters obtained by summation will be considered in the last step.

c_{Pr} (at.%)	R_{C} (Å)	L (Å)
YLF		
0.34	6.2	0.2
0.38	6.9	0.4
0.64	7.3	0.8
0.65	7.7	1.0
0.70	7.8	0.9
1.35	8.4	1.9
LLF		
0.15	8.9	0.1
0.20	38.3	1.1
0.45	10.6	0.5
BYF		
0.65	7.6	2.1
1.50	6.6	4.6
2.30	8.3	2.0
KYF		
2.00	12.4	0.2

Table 3.6: Calculated parameters for (super-)exchange induced energy transfer

Determination of the parameters regarding exchange-induced cross-relaxation energy transfer processes

Finally, the time interval from 0 s to $0.2 \cdot \tau_{\mathrm{R}}$ was calculated taking into account exchange as well as dipole-dipole interaction and energy migration (Equations 3.55 and 3.58). To receive reasonable results, the parameters for dd induced cross-relaxation and energy migration were fixed. In this way both the effective Bohr radius L and the critical distance R_{C} could be acquired.

$$W_{\mathrm{D_0A}_l} = \frac{C_{\mathrm{DA,s}}^{\mathrm{dd}}}{R_{0l}^6} + \frac{1}{\tau_{\mathrm{R}}} \exp\left[\frac{2R_{\mathrm{C}}}{L}\left(1 - \frac{R_{0l}}{R_{\mathrm{C}}}\right)\right] \tag{3.58}$$

Table 3.6 shows the results of the calculations. The critical distances for exchange-induced cross-relaxations are in the range from about 7 Å to 11 Å, which means every praseodymium ion within a sphere of 11 Å around an excited praseodymium ion can act as an acceptor. The determination of the effective Bohr radius however shows large discrepancies: depending on the crystal structure, values from below 0.1 Å up to 2.7 Å were obtained. These values contain a large uncertainty because the model does not consider an inhomogeneous ion distribution.

Discussion

Lupei has been investigating the exchange-induced energy transfer mechanism in the well-known system Nd^{3+}:$Y_3Al_5O_{12}$ for several years and received comparable results for R_C [DT98, Lup00]. In this system, the critical distance was in the range from 5 Å to 10 Å. Concerning the effective Bohr radius L, values from 0.5 Å to 1.0 Å have been reported. These results are in accordance with the obtained data from the Pr^{3+}-doped fluorides which were investigated in this work.

3.4 Low Temperature Results

In this section spectroscopic results of both YLF and LLF performed at cryogenic temperatures will be presented. Because these crystal systems behave identically, the spectra were taken from different samples and concentrations. After introducing the results obtained by absorption measurements in Section 3.4.1, site-selective emission spectroscopy leads to the results discussed in 3.4.2. Further investigations on the Pr^{3+}-ions in these Scheelite-type structures regarding excitation and lifetime measurements are presented in the last section.

3.4.1 Low Temperature Absorption Measurements

The spectral behaviour of praseodymium ions in the Scheelite-type structures YLF and LLF have been investigated under cryogenic temperatures of ≈10 K. The absorption coefficient of the transition ${}^3H_4 \rightarrow {}^3P_0$ at 479.32 nm is displayed in Figure 3.18 for different Pr^{3+}-concentrations. The spectral resolution was set to 0.03 nm and the measurement stepwidth was 0.01 nm for these measurements.

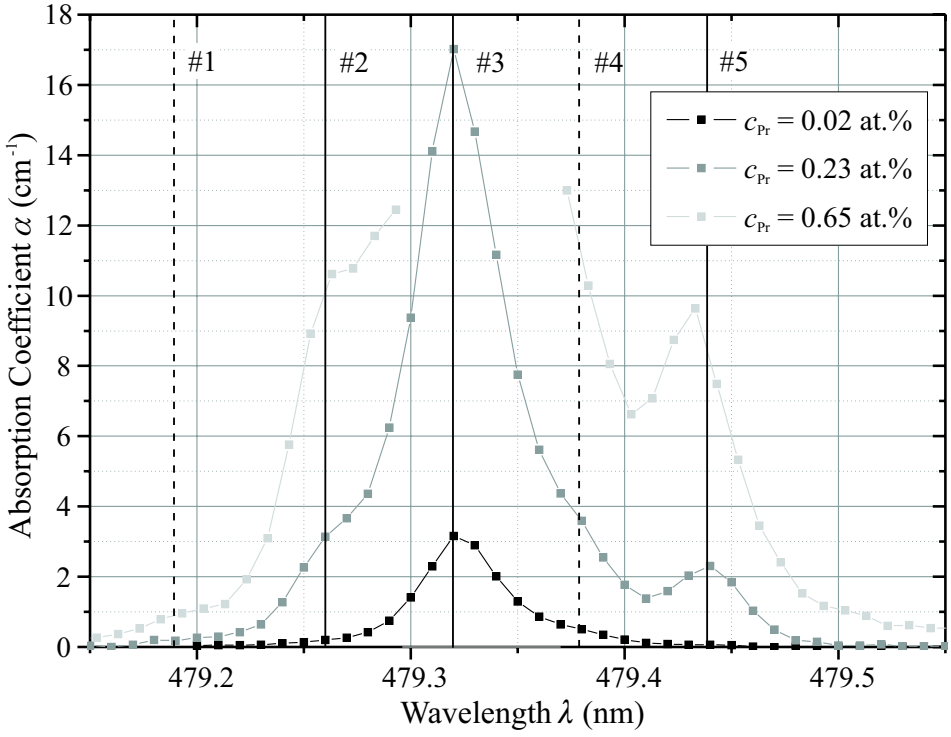

Figure 3.18: Absorption spectrum of Pr^{3+}:YLF on the transition ${}^3H_4 \rightarrow {}^3P_0$ measured at 10 K ($\vec{E} \| \vec{c}$)

Due to the thickness of the highly doped sample (0.65 at.% Pr^{3+}), the peak absorption

coefficient could not be determined and the data points around the maximum have been removed. Nevertheless, several information can be found in the spectra. From the theoretical point of view, the $^3P_0$-level should not show any Stark splitting, because the total angular momentum equals zero. However, the ground state absorption into the $^3P_0$ occurs at several wavelengths. Beside the main peak absorption at 479.32 nm (#3, 20863 cm^{-1}), two strong lines, #2 and #5 at 479.26 nm (20866 cm^{-1}) and 479.44 nm (20858 cm^{-1}) have been detected, respectively. Furthermore, two other ground state transitions can be found at 479.19 nm (#1, 20869 cm^{-1}) and 479.38 nm (#4, 20860 cm^{-1}). Possible explanations for the existence of multiple absorption peaks are as follows:

1. At least one of the energy levels $^3P_1$ or $^1I_6$ possess Stark levels in this energy range. With respect to the published data of Stark levels from Pr^{3+}:$LiYF_4$, any Stark level from the $^3P_1$ or $^1I_6$ is located more than 223 cm^{-1} above the $^3P_0$ [Est79, Ada85]. This energy difference corresponds to a wavelength difference of ≈5 nm.

2. The absorption bands are due to impurities from other rare earth ions or other metal ions inside the crystal matrix. In case there are reasonable amounts of other rare earth ions in the crystal, only Sm^{3+}, Tb^{3+} or Er^{3+} are actually absorbing in the spectral region around 480 nm. However, excitation of the sidebands did not lead to characteristic spectra of any rare earth ion besides Pr^{3+}. Although it is not possible to exclude the occurrence of other impurities, no evidence of any influence on the effects investigated have been found.

3. The host lattice matrix is not perfect and thus enables different environments for rare earth ions. In this case, the distorted environment leads to slightly different energies of the $^3P_0$ level and thus to different absorption wavelengths. Although it is well-known that any crystal contains defects like dislocations, imperfections or colour centres in the lattice, no information regarding the defect density of YLF single crystal has been published yet, to the best of the authors knowledge. Nevertheless, colour centre generation by ultrashort pulses has already been demonstrated in Tm^{3+}:YLF [Cou07]. But even without exposing YLF single crystals to high-intensity radiation, defects have been found via spectroscopic investigations of Nd^{3+}:YLF. In the same way as shown in Figure 3.18, Barthem discovered five satellites in absorption spectra taken at 1.5 K [Bar86]. In his interpretation, the discovered satellite bands resulted from the formation of different Nd^{3+}-pairs. Thus, Pr^{3+}-ions in the YLF host lattice might form pairs as well.

Considering the probability of the explanations discussed above, the third one seems to be the most promising one. Additional measurements investigating the local site symmetry of the Pr^{3+}-ions in YLF using ESR[2]-measurements did not result in usable data. The signal-to-noise ratio of the investigated samples was too low. The hypothesis of pair formation will be confirmed in Section 3.4.3.

[2]ESR: electron spin resonance

3.4.2 Low Temperature Emission Measurements

Using a narrowband OPSL as excitation source, site-selective fluorescence spectra were recorded from the cooled crystals. Figure 3.19 shows the measured spectra for $\vec{E} \parallel \vec{c}$ polarization for Pr^{3+}(0.23 at.%):YLF. Here, the spectral resolution and the data interval was set to 0.2 nm and 0.066 nm, respectively. As excitation wavelengths, 479.32 nm (Figure 3.18 #3) and 479.44 nm (Figure 3.18 #5) were used. The other excitation wavelengths either led to a significantly lower signal level or did not show any fluorescence at all, which might indicate closely spaced and thus strongly quenched Pr^{3+}-pairs.

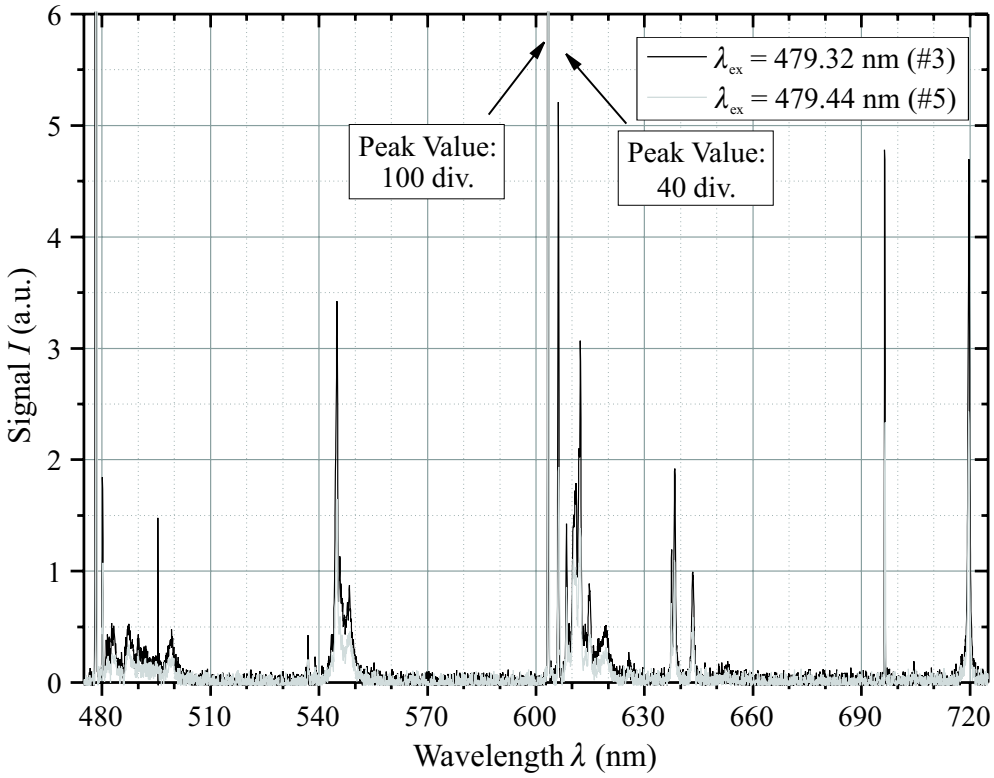

Figure 3.19: $\vec{E} \parallel \vec{c}$-polarized emission spectrum of Pr^{3+}(0.23 at.%):YLF measured at 10 K under different excitation wavelengths

Two interesting aspects arise from the fluorescence spectra: on the one hand, the Pr^{3+} ions at sites #3 and #5 possess slightly different energy level schemes and on the other hand the polarized Pr^{3+}-fluorescence near 604 nm is by far the strongest line of emission, as Hashimoto recently found out [Has07b]. With increasing temperatures the emission intensity at 604 nm is decreasing significantly. The reason for this behaviour is still uncertain. Amplified spontaneous emission at this wavelength has been found at higher pump intensities, but has been suppressed during the measurement process by reducing the output power of the excitation source to 6 mW, limiting the excitation intensity to

$12\,\mathrm{W/cm^2}$ in the sample. The influence of the broad GSA bands into the $^1D_2$ state around 595 nm (Figure 3.9) is not strong enough to suppress such a strong fluorescence signal.

3.4.3 Low Temperature Excitation and Lifetime Measurements

Because the fluorescence at 604 nm is dominant, this spectral region was investigated in further detail by excitation spectroscopy and lifetime measurements.

Figure 3.20 displays the results obtained under cw-excitation by the OPSL. These measurements were performed with a spectral resolution and a data interval of 0.03 nm and 0.01 nm, respectively. As it can be clearly seen from the figure, the emission wavelength changes when exciting different sites. In the spectral region around 604 nm three different emission wavelengths have been found. The emission at 604.29 nm refers to the ion class #3. Excitation close to the corresponding absorption wavelength of 479.32 nm leads to a strong fluorescence signal. Emission at 604.40 nm is induced by excitation of ion class #5 while the transition at 604.49 nm can be excited by tuning the excitation wavelength to 479.52 nm.
These results indicate no energy transfer occurring from class #3-ions to class #5-ions. In contrast, emission from class #3-ions occurs at every shown excitation wavelength. This is most likely due to their broad absorption characteristics. An interesting aspect is the incorporation of Pr^{3+} ions into the different sites in crystal matrix of YLF. The concentration dependence of incorporated Pr^{3+} ions can be determined by measuring the emission spectrum under excitation of ion class #5. In this case, both classes #5 and #3 show fluorescence. Assuming that most of the ions are of class #3, direct comparison of the fluorescence intensity of #5 scaled by the emission of #3 results in the concentration dependence. In Figure 3.21 the maximum emission intensities of both #3 and #5 are shown in a double logarithmic plot. The slope of the emission intensity of site #3 has been adjusted to be $1\,(\mathrm{at.\%})^{-1}$, meaning a concentration scaled intensity. Under these conditions the slope of emission intensity of class #5 ions was roughly $4.6\,(\mathrm{at.\%})^{-1}$. This result states a highly increasing amount of Pr^{3+}-ions located at this type of lattice site with increasing Pr^{3+}-concentration. Due to the large discrepancy of the ionic radii of Y^{3+} and Pr^{3+}, lattice distortions in the neighbourhood of Pr^{3+}-ions seem to emerge in the Pr^{3+}:YLF-system.

The excitation source for the decay measurements was an optically parametric oscillator (OPO) operated in pulsed mode providing a pulsewidth of 30 ns. The excitation wavelength width was $\Delta\lambda \approx 0.2$ nm at 479.3 nm. Thus, the excitation spectra are not fully resolved and the measured linewidth is not resembling the intrinsic linewidth of the Pr^{3+}-system. However, the qualitative behaviour can still be discussed. The resolution for the decay curves was limited by the spectral resolution of the 0.5 m monochromator. Sufficient signal was obtained from the emission from the ions of class #3 and #5, but not for the transition at 604.49 nm. Thus, the smallest emission peak has not been characterized.

Figures 3.22(a) and (b) show the decay characteristics of class #3 and class #5 Pr^{3+}-ions for different concentrations in semilogarithmic scale. The decay curves in 3.22(a)

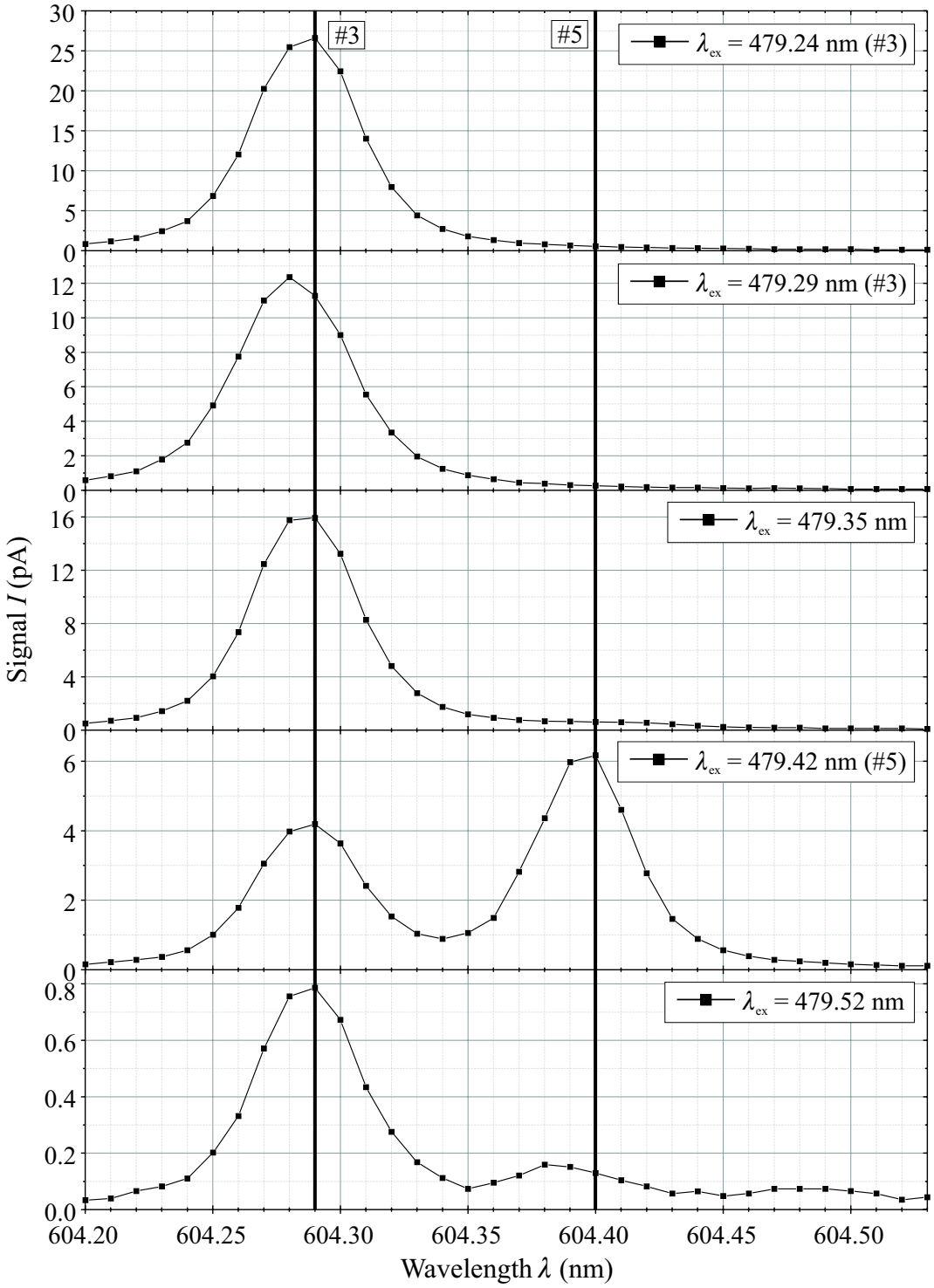

Figure 3.20: Site-selective emission spectra of Pr^{3+}:YLF excited by OPSL. The lines at 604.29 nm and 604.40 nm indicate the emission wavelength of class #3 and #5 Pr^{3+}-ions, respectively

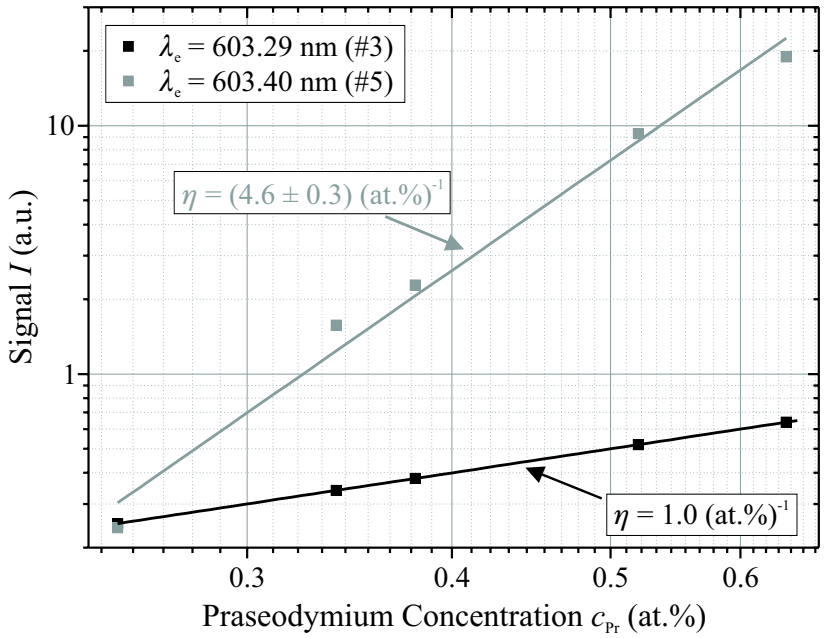

Figure 3.21: Concentration dependence of the emission intensity of ions at site #3 and #5

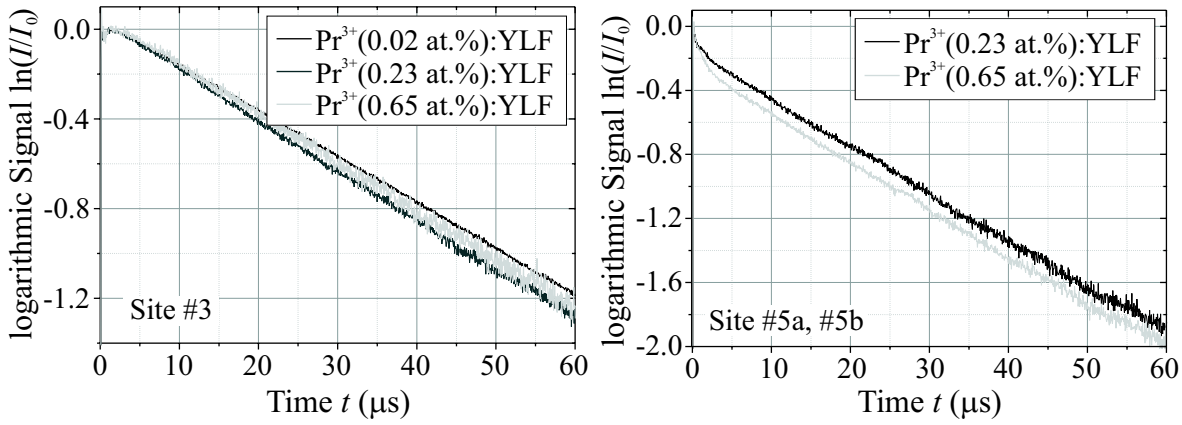

(a) (b)

Figure 3.22: $^3P_0$ decay characteristics of Pr^{3+}:YLF with different Pr^{3+} concentrations in case of (a) ion class #3 and (b) ion class #5

show single exponential decays which are almost independent of the Pr^{3+} concentration. Because the associated absorption peak is present even at very low concentration levels and the excited state decays exponentially, ion class #3 refers to Pr^{3+}-ions on regular Y^{3+}/Lu^{3+} lattice sites in the YLF/LLF single crystal. These ions do not interact with other dopant ions at these temperature levels.

The decay curve of class #5 ions shown in Figure 3.22(b) featured two decay constants. A fast decay is dominant during the first 2.5 µs after the excitation pulse and a slower one at longer timescales. Due to the low temperature of ≈10 K, and thus a reduced capability of energy transfer, these decay curves cannot be explained by a single class of ions only. In fact, two different ion classes are contributing to the emission at the investigated wavelength. In the following discussion the class having a high nonradiative decay rate will be referred to as #5a and the second, slow decrease in fluorescence intensity is a result of the decay of ions of class #5b.
The high nonradiative decay rate of ion class #5a must be a result of fast CRPs leading to a fast increase of the population of the $^1D_2$ and $^1G_4$ energy levels according to Figure 3.13(b). In the same time interval, many ions of class #5b are still excited because of the lower decay rate. A comparison between the decay rates of class #3 ions ($W_3 = 2.3\times10^4\,s^{-1}$) and class #5b ions ($W_{5b} = 3.1\times10^4\,s^{-1}$) shows a clear difference. Due to the single exponential decay, it is most likely that the class #5b ions have a slightly different crystal field but do not interact with other impurity ions.

The corresponding excitation measurements at Pr^{3+}:LLF are shown in Figure 3.23. The data confirms the assumptions made earlier. Class #3 ions are excited by the largest peak of absorption only. By contrast, the ions associated to classes #5a and #5b feature a double peak structure in the excitation spectrum, which can be explained by two closely spaced Pr^{3+}-ions, whose electron wave functions are overlapping. Due to the overlap of the optically active electron shells the two ions form a pair that must be treated as a single dimer system with the quantum mechanics formalism. Since the wave function of the coupled system need to fulfill Pauli's exclusion principle, the two single ion cannot have identical energy levels. The coupled system shows the so-called Davydov splitting for all single atom energy levels into two states[Mor65]. The overlap shifts the energetic states of the interacting ions and enables fast excitation energy transfer between these ions. Thus, it is most likely that Pr^{3+}-ions of class #5 are located at distorted crystal sites. Furthermore, the slightly asymmetric excitation peak heights might be a result of the two different ion classes #5a and #5b. Ion class #5b corresponds to one excitation wavelength only and thus supports the assumption of a single ion at a distorted lattice site. Considering the excitation spectrum for $^1D_2$-emission, it becomes clear that $^1D_2$-emission occurs when Pr^{3+}-ions are excited to the $^3P_0$-state even at low temperatures. The shape and position of the excitation peak indicates several crystal sites contributing to the excitation population of the $^1D_2$ state. The excitation peak is not symmetrical but has a satellite where class #5a and #5b ions are absorbing. This might point at a more reasonable amount of these ions providing excitation energy to the $^1D_2$-level compared to class #3 ions.

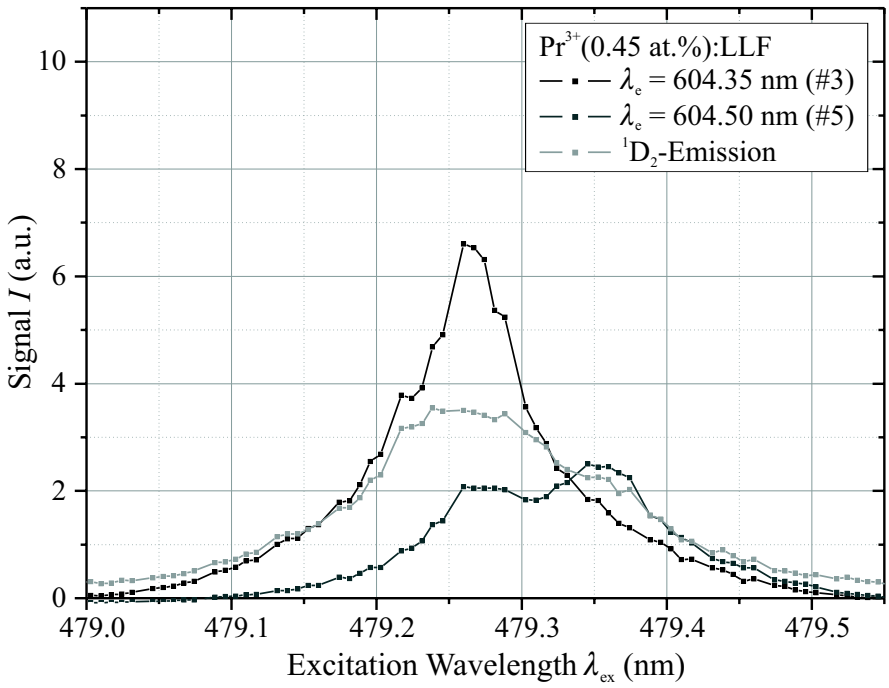

Figure 3.23: $^3P_0$ excitation spectra of site #3, #5 and of the $^1D_2$ energy level Pr^{3+}(0.45 at.%):LLF obtained with a pulsed OPO system as excitation source.

3.4.4 Temperature Dependence of the $^3P_0$ Decay Characteristics

With the knowledge obtained from the last two sections, the temperature dependence of the $^3P_0$ decay characteristics of Pr^{3+}:YLF crystals with reasonable dopant levels can be explained. According to Figure 3.24, a nonexponential decay can be found within the first 10 microseconds after excitation at 300 K. Long-ranged electric multipole or exchange induced interaction generates the nonexponential part. With decreasing temperature down to 100 K, the decay curve changes to a single exponential curve.

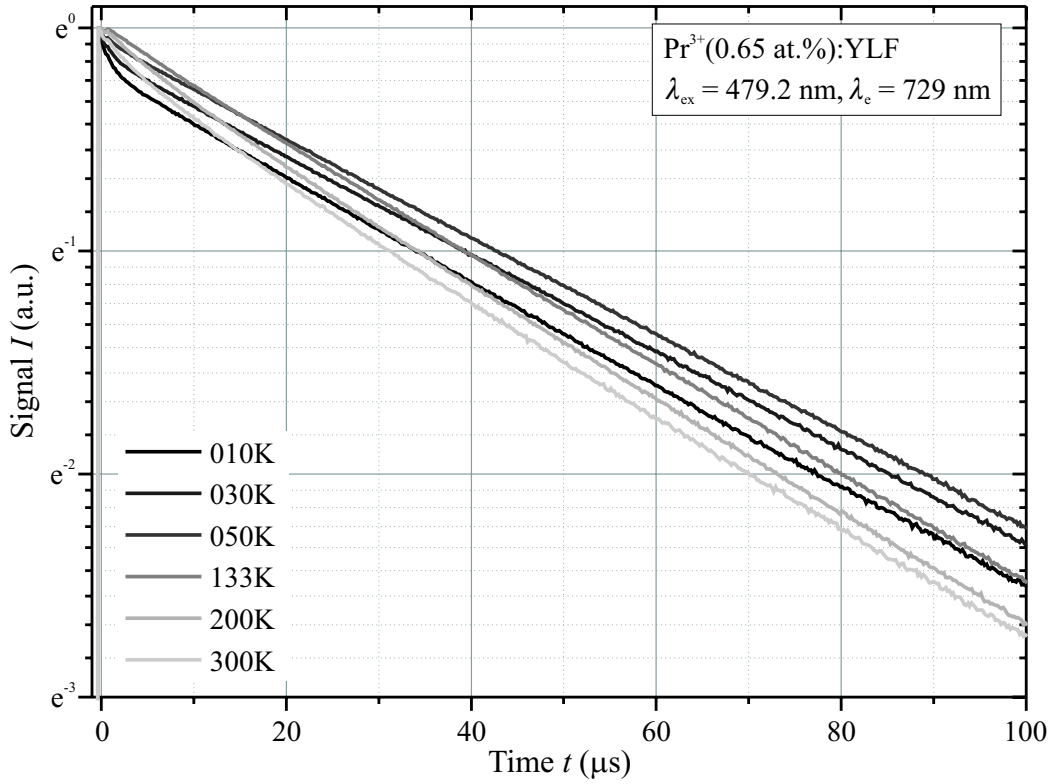

Figure 3.24: Temperature dependence of the $^3P_0$-decay in Pr^{3+}(0.65 at.%):YLF under direct excitation

The reason for this behaviour can be found in the reduction of the linewidths in absorption and emission, leading to a significantly reduced microparameter (cf. Equation 3.18). With decreasing temperature, several nonradiative energy transfer channels are most likely "frozen" out resulting in an increased fluorescence yield. At 100 K, the different sites found in the low temperature measurements are still able to transfer their energy in a microscopic scale. Further reduction to 10 K leads to further uncoupling of these ion classes. This process results in an average decay curve, which is nonexponential in the first 6 microseconds and single exponential afterwards.

3.5 Summary

In this chapter, the incorporation behaviour of praseodymium ions in the fluoride crystals YLF, LLF, BYF and KYF have been investigated using optical spectroscopy. Effective cross-relaxation processes resulting in nonradiative decay rates of some thousands of s^{-1} have been found. The nature of interaction between Pr^{3+}-ions at room temperature results from (super-)exchange and dipole-dipole interaction. Typical distances of interaction are about 9 Å in case of (super-)exchange and about 70 Å in case of dipole-dipole induced interaction. By reducing the temperature below 100 K, several nonradiative energy transfer channels are most likely "frozen" out and the luminescence from the different sites found in the low temperature measurements becomes observable. Further reduction to 10 K leads to further uncoupling of the different ion classes.

A more detailed study on the most promising crystal structures for efficient laser action, YLF and LLF, revealed more than 5 ion classes which correspond to different sites in the host lattice. By all means available, 3 of them could be identified. Besides the Pr^{3+}-ions on regular Y^{3+}/Lu^{3+}-sites, one more ion class which is not influenced by excitation energy transfer has been found. However, it corresponds to an irregular lattice site. An increase in the ion concentration revealed a tendency to cluster even at Pr^{3+}-concentrations of 0.22 at.%. This is not surprising considering the ionic radii of the host ion and the dopant ion. By incorporation of large dopant ions, local stress is induced in the host matrix. This can be compensated by voids, for example. The last type of Pr^{3+}-ions found in the spectroscopic investigations performs efficient energy transfer most likely induced by the exchange mechanism. These ions are located at irregular sites and contribute to the population of the $^1D_2$ energy level strongly.

4 Laser Experiments

4.1 Fundamentals

In this section basic properties of the methods applied during the laser experiments will be given. After a brief introduction to the rate equation model used to describe the properties of a 4-level laser system, key aspects of second harmonic generation and active Q-switching will be presented. The concluding parts contain general information about the pump laser systems used in the experiments, namely frequency doubled optically pumped semiconductor lasers (OPSLs) and GaN-based laser diodes (GaN-LDs).

4.1.1 Laser Principles

Rate Equation Model

In order to obtain laser oscillation, population inversion is necessary. Population inversion regarding the energy levels 1 and 2 (see Figure 4.1) is obtained when the population density N_2 of a higher located energy level (energy E_2) is larger than the population density N_1 of a lower energy level (energy E_1). As a result, amplification of light of the frequency $\nu_L = h^{-1}(E_2\text{-}E_1)$ by stimulated emission can be achieved under these conditions. By designing an optical cavity, which enables an electromagnetic standing wave inside, laser oscillation can take place. A more detailed discussion of the employed optical cavities used can be found in Section 4.3 in this work. A large overview of laser cavity design aspects and explanations can be found in [Sve89, Koe99].

Many well-established lasers are 4-level laser systems like for example Ti^{3+}:$\alpha-Al_2O_3$, Nd^{3+}:$Y_3Al_5O_{12}$ or Pr^{3+}:YLF. Figure 4.1 shows the energy level scheme of Pr^{3+} in YLF with optical transitions in the visible spectral region. Direct excitation of the upper laser levels ($^3P_0$ or $^3P_1$, population density N_2) can be achieved efficiently by two wavelengths, either 443.9 nm or 479.6 nm. Using a GaN-LD, Pr^{3+}-ions can be excited from the ground state $^3H_4$ (population density N_0) into the $^3P_2$ level (population density N_3) followed by a fast relaxation as indicated or by using an OPSL which directly excites at the short wavelength wing of the ground state transition into the $^3P_0$. Depending on the effective lifetime of the upper laser level, population inversion with respect to the lower laser levels ($^3F_4$, $^3F_2$, $^3H_6$ or $^3H_5$, population density N_1) is generated by these pump sources. If the lower laser level is efficiently depleted, laser oscillation is possible at the transition from the upper to the lower laser level. In principle it is possible to obtain inversion by

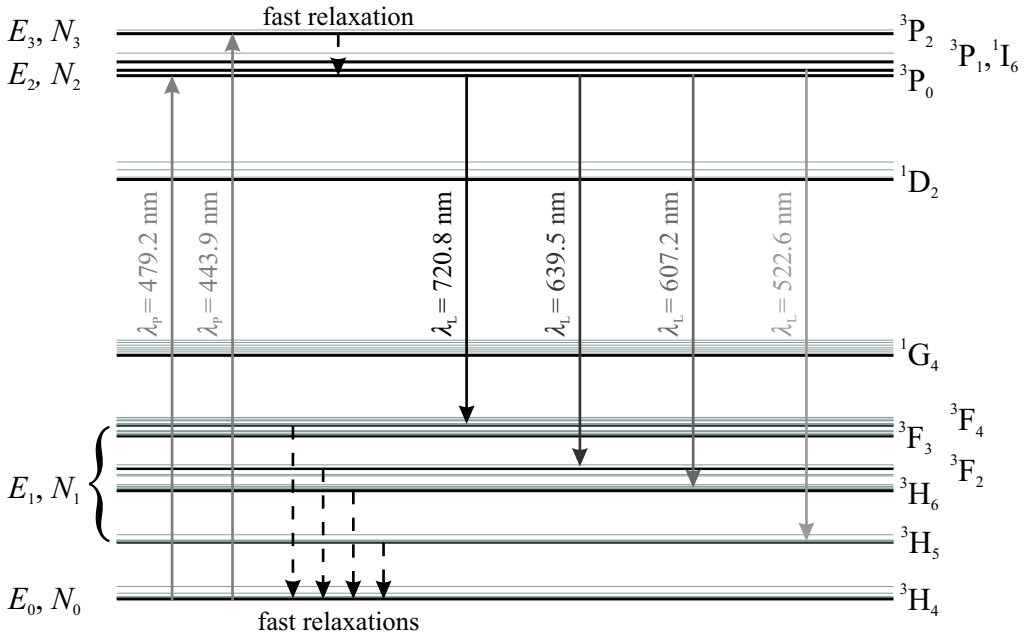

Figure 4.1: Energy level scheme of Pr^{3+}:YLF with the investigated 4-level-laser transitions. N_j and E_j denote the population densities and energy of state j

absorption of a single pump photon. This is the major advance of 4-level laser systems in comparison to 3-level lasers, where the laser transition ends in one of the Stark levels of the ground state, which is thermally populated at ambient temperatures.

To describe the power characteristics of a laser system, rate equations are used. In case of the ideal 4-level laser operating in the continuous wave mode (cw) the following rate equations are considered [Sve89]:

$$\frac{dN_2}{dt} = W_\mathrm{P} N_0 - BqN_2 - \frac{N_2}{\tau_\mathrm{eff}} \tag{4.1}$$

$$\frac{dq}{dt} = V_\mathrm{L} B N_2 q - \frac{1}{\tau_\mathrm{c}} q \tag{4.2}$$

$$N_\mathrm{t} = N_0 + N_2 \tag{4.3}$$

Here, W_P denotes the pump rate, q is the laser photon number, N_t denotes the total ion density, and V_L denotes the volume of the laser mode inside the active medium. Equation 4.1 describes the temporal behaviour of the population of the upper laser level. The population is on the one hand increased by the pump rate but on the other hand decreased by the laser transition and spontaneous emission. Equation 4.2 resembles the laser photon number inside the optical cavity. The first term reflects the increase of laser photons by the stimulated emission process while the second term describes the reduction of the photon number by output coupling and other loss processes inside the cavity. This

is represented by the photon lifetime τ_c. The last Equation (4.3) provides a constant ion density. Due to the fast relaxation processes, the population densities N_3 and N_1 are neglected.

The rate equation system described above does not consider the initial condition of laser oscillation caused by spontaneous emission. In Equation 4.2 the photon growth rate would remain zero for all times if no laser photon is present in the beginning. The following equations are stationary results of the already started laser oscillation process. In this case the missing initial conditions have no effect. However, for a numerical simulation process these conditions have to be considered.

The parameter B is given by

$$B = \frac{\sigma_e c_0 l}{V_L L'} = \frac{\sigma_e c_0 l}{V_L (L + (n-1)l)}. \tag{4.4}$$

Here, σ_e denotes the emission cross-section of the laser transition. The parameter L' is the effective cavity length which takes into account the refractive index of the active medium, L is the cavity length and l is the crystal thickness.
Introducing the inversion population density $N_i = N_2 - N_1 \approx N_2$ the rate equation system can be transformed to

$$\frac{dN_i}{dt} = W_P(N_t - N_i) - BqN_i - \frac{N_i}{\tau_{eff}} \tag{4.5}$$

$$\frac{dq}{dt} = V_L B N_i q - \frac{1}{\tau_c} q \tag{4.6}$$

In case of continuous wave lasing $dN/dt = 0$ and $dq/dt = 0$ holds. The threshold inversion can be derived from Equation 4.6

$$N_{thr} = \frac{1}{V_L B \tau_c} = \frac{\gamma}{\sigma_e l} \tag{4.7}$$

where $\gamma = L'/(\tau_c c_0)$ are the roundtrip losses of the optical cavity. N_{thr} is the value of the population inversion where the gain compensates these losses. The losses can be separated into the internal losses $\gamma_i = \text{-ln}(1\text{-}L_i)$ and the losses originating from the cavity mirrors $\gamma_1 = \text{-ln}(1\text{-}T_1)$ and $\gamma_2 = \text{-ln}(1\text{-}T_2)$ according to

$$\gamma = \gamma_i + \frac{\gamma_1 + \gamma_2}{2}. \tag{4.8}$$

The parameters T_1, T_2 and L_i denote the mirror transmissions and the losses caused by the active medium, respectively.
The pump rate for the threshold condition W_{thr} is determined by Equations 4.6 and 4.7 resulting in

$$W_{\mathrm{thr}} = \frac{N_{\mathrm{thr}}}{(N_{\mathrm{t}} - N_{\mathrm{thr}})\tau_{\mathrm{eff}}} \approx \frac{N_{\mathrm{thr}}}{N_{\mathrm{t}}\tau_{\mathrm{eff}}} = \frac{\gamma}{N_{\mathrm{t}} l \tau_{\mathrm{eff}} \sigma_{\mathrm{e}}}. \tag{4.9}$$

Under these conditions, the laser photon number equals zero. An increase in the pump rate W_{P} above W_{thr} results in an increasing photon number q, while the inversion population remains constant at N_{thr}. The photon number can be described by

$$q = V_{\mathrm{L}}\tau_{\mathrm{c}} \left(W_{\mathrm{P}}(N_{\mathrm{t}} - N_{\mathrm{thr}}) - \frac{N_{\mathrm{thr}}}{\tau_{\mathrm{eff}}} \right) = V_{\mathrm{L}} N_{\mathrm{thr}} \frac{\tau_{\mathrm{c}}}{\tau_{\mathrm{eff}}} \left(\frac{W_{\mathrm{P}}}{W_{\mathrm{thr}}} - 1 \right) \tag{4.10}$$

resulting in the laser power transmitted through mirror 2

$$P_2 = \frac{\gamma_2 c_0}{L'} h\nu_{\mathrm{L}} q = \frac{\gamma_2 h\nu_{\mathrm{L}} V_{\mathrm{L}}}{\sigma_{\mathrm{e}}\tau_{\mathrm{eff}} l} \left(\frac{P_{\mathrm{abs}}}{P_{\mathrm{thr}}} - 1 \right). \tag{4.11}$$

Here, P_{abs} denotes the absorbed pump power and P_{thr} the absorbed pump power at the laser threshold

$$P_{\mathrm{thr}} = W_{\mathrm{thr}} h\nu_{\mathrm{P}} V_{\mathrm{L}} N_{\mathrm{t}} = \frac{\gamma h\nu_{\mathrm{P}} V_{\mathrm{L}}}{\sigma_{\mathrm{e}}\tau_{\mathrm{eff}} l}. \tag{4.12}$$

A second parameter describing the power characteristics of a laser is the slope efficiency η_{S}. It is the derivative of the output power with respect to the absorbed pump power

$$\eta_{\mathrm{S}} = \frac{dP_2}{dP_{\mathrm{abs}}} = \frac{h\nu_{\mathrm{L}} V_{\mathrm{L}}}{\sigma_{\mathrm{e}}\tau_{\mathrm{eff}} l} \frac{\gamma_2}{P_{\mathrm{thr}}} = \frac{\nu_{\mathrm{L}}}{\nu_{\mathrm{P}}} \frac{\gamma_2}{2\gamma}. \tag{4.13}$$

The slope efficiency is proportional to the quantum defect $\eta_{\mathrm{Q}} = (\nu_{\mathrm{L}})/(\nu_{\mathrm{P}})$as well as the ratio between the output coupling losses and the total cavity losses $\gamma_2/(2\gamma) = T_2/(T_2 + L_{\mathrm{i}})$.

These results are valid for ideal 4-level lasers exhibiting no other loss channels for the laser process such as reabsorption of the laser photons, ESA- or energy transfer processes. By introducing different loss channels, Equations 4.12 and 4.13 must be extended to

$$P_{\mathrm{thr}} = \frac{\gamma h\nu_{\mathrm{P}} V_{\mathrm{L}}}{\sigma_{\mathrm{e}}\tau_{\mathrm{eff}} l \eta'} \tag{4.14}$$

and

$$\eta_{\mathrm{S}} = \eta' \frac{\nu_{\mathrm{L}}}{\nu_{\mathrm{P}}} \frac{\gamma_2}{2\gamma} = \eta' \eta_{\mathrm{Q}} \frac{T_2}{T_2 + L_{\mathrm{i}}} = \eta'' \eta_{\mathrm{O}} \eta_{\mathrm{Q}} \frac{T_2}{T_2 + L_{\mathrm{i}}}. \tag{4.15}$$

Here, η' denotes all efficiencies which influence the laser performance, η_O denotes the geometrical overlap efficiency of the pumped volume and the laser mode in the active medium and $\eta'' \equiv \eta'/\eta_O$ denotes other loss processes affecting the laser[1].

Reabsorption losses can be introduced in the initial rate equations by terms linear in population densities. They are essential for 3-level laser systems and have been studied in detail by Risk [Ris88]. In contrast, energy transfer processes like cross-relaxations or upconversion processes are two-ion processes and need to be introduced by terms quadratic in population densities (see for example [Osi03a]). As a result, such a rate equation system can only be solved numerically. Due to unknown coupling parameters of the CRPs shown in Figures 3.13(b) and 3.14(b), the influence of these processes for the Pr^{3+}-lasers have not been investigated in detail.

The influence of CRPs on the slope efficiency is reduced if high laser intensities in the active medium are achieved. Danielmeyer [Dan76] defined the so-called stimulated lifetime

$$\tau_S = \frac{I_S}{I}\tau_{eff}. \tag{4.16}$$

With this parameter, an estimation of the power level where CRPs do not have any effect on the slope efficiency is possible. In Equation 4.16 I denotes the laser intensity and $I_S = \frac{h\nu_L}{\sigma_e \tau_{eff}}$ denotes the saturation intensity of the laser transition. If $I \gg I_S$, the influence of CRPs is reduced because the rate of stimulated emission exceeds the cross-relaxation rate. The necessary intensities for some of the investigated samples are estimated in Section 4.4.1.

Loss Determination

To determine the internal residual roundtrip losses of a given laser cavity, two methods were applied. The first method, introduced for 4-level laser systems by Findlay and Clay [Fin66], takes into account the dependence of the laser threshold power P_{thr} on the total losses γ. By assuming a completely reflecting mirror M_1 which corresponds to $\gamma_1 = 0$ Equation 4.12 can be transformed to

$$\gamma_2 = \frac{2\sigma_e \tau_{eff} l}{h\nu_P V_L} P_{thr} - 2\gamma_i = K_C P_{thr} - 2\gamma_i. \tag{4.17}$$

The parameter K_C denotes the parameter proportional to the small signal gain coefficient. By plotting γ_2 with respect to P_{thr} and performing a linear fit, the internal losses γ_i can be determined with an extrapolation to $P_{thr} = 0$.

The second method for determining the internal losses was presented by Caird et *al.* [Cai88]. Here the dependence of the slope efficiency with respect to the output coupling losses $\gamma_2 + \gamma_1$ is used. Assuming again $\gamma_1 = 0$, Equation 4.13 can be written as

[1] Other efficiencies are for example the pumping efficiency or the energy transfer efficiency in case of codoped systems.

$$\frac{1}{\eta_S} = \frac{1}{\eta_Q}\left(1 + \frac{2\gamma_i}{\gamma_2}\right) \tag{4.18}$$

From the linear dependence of η_S^{-1} with respect to γ_2^{-1}, two parameters can be obtained. At the condition $\gamma_2^{-1} = 0$, the slope efficiency η_S equals η_Q, the quantum defect, which is the maximum obtainable slope efficiency. The internal losses γ_i can be determined from the slope of the linear fit.

Laser Beam Characteristics

Laser beams originating from solid-state lasers usually feature beneficial beam properties. The most important are described in the following paragraphs.

Let the z-axis be along the resonator axis and the transversal intensity profile to be Gaussian. In this case, the laser beam radius $w(z)$ follows the equation

$$w(z) = w_0\sqrt{1 + \left(\frac{z}{z_R}\right)^2}. \tag{4.19}$$

The laser beam radius w of a Gaussian beam is defined as the shortest distance from the beam axis to the location where the intensity is reduced to $1/e^2$. The Rayleigh length z_R describes the near-field expansion of the beam. It is defined as the distance from the position of the beam waist w_0 to the position where the beam radius equals $\sqrt{2}w_0$ and can be calculated by

$$z_R = \frac{n\pi w_0^2}{\lambda M^2} = \frac{w_0}{\theta}. \tag{4.20}$$

Here, n denotes the refractive index of the medium at wavelength λ. The angle θ describes the far field of the laser beam and is half of the angle of divergence. It is given by Equation 4.21,

$$\theta = \frac{\lambda M^2}{n w_0 \pi} \tag{4.21}$$

The confocal parameter b is equivalent to the Rayleigh length. It is connected to z_R by $b = 2z_R$. The beam quality factor M^2 takes into account the deviation of the transversal intensity profile of a laser beam with respect to a Gaussian profile. For a Gaussian beam, $M^2 \equiv 1$, while any deviation leads to $M^2 > 1$. In general, the beam quality factor for solid state lasers can reach 1. Such beams are called diffraction limited.
M^2 is measured by determining the beam parameters w_0 and θ of a focused beam. By combining Equations 4.20 and 4.21, one obtains

$$M^2 = \frac{n\pi w_0 \theta}{\lambda} \tag{4.22}$$

4.1.2 Second Harmonic Generation

This section gives a brief overview of second harmonic generation (SHG). A more detailed description of the effects can be found in [Boy95, Sut96].

When an electromagnetic wave passes a dielectric medium, the electrons in the medium are deflected with respect to their equilibrium condition. As a consequence, these induced electric dipoles generate a macroscopic polarization $\vec{P}$. At sufficiently high intensities, the induced polarization cannot be described by a linear dependence on the incident electric field $\vec{E}$ but higher orders in $\vec{E}$ have to be taken into account as well. Each component of the induced polarization vector follows the equation

$$P_{\mathrm{i}} = \epsilon_0 \chi^{(1)}_{\mathrm{ij}} E_{\mathrm{j}} + \epsilon_0 \chi^{(2)}_{\mathrm{ijk}} E_{\mathrm{j}} E_{\mathrm{k}} + \epsilon_0 \chi^{(3)}_{\mathrm{ijkl}} E_{\mathrm{j}} E_{\mathrm{k}} E_{\mathrm{l}} + \ldots \tag{4.23}$$

Here, ϵ_0 denotes the electric permittivity of the free space and $\chi^{(\mathrm{m})}$ denotes the tensor of the dielectric susceptibility of rank m+1. SHG occurs when the components of $\chi^{(2)}$ are different from zero. This is true in case of non-centrosymmetric crystals. Due to $\chi^{(2)}$, the induced polarization oscillates not only with the frequencies of the incident waves ω_1 and ω_2 but also with $2\omega_1$, $2\omega_2$, $\omega_1 + \omega_2$, and $\omega_1 - \omega_2$. The first two are called SHG, while the third and the fourth are labeled sum frequency generation (SFG) and difference frequency generation, respectively.

Due to the dispersion of the crystal, the electromagnetic waves with ω and 2ω see different indices of refraction n_ω and $n_{2\omega}$, respectively. As a result, the phase difference between the initially generated wave and the wave generated along the optical path increases. After passing the coherence length $L_{\mathrm{C}} = \frac{\lambda}{4(n_{2\omega} - n_\omega)}$ the phase difference reaches $\lambda/2$ and the SHG-radiation is converted back to the fundamental wave with frequency ω. To obtain SHG over larger distances, the phase velocities for the fundamental and the second harmonic wave must be matched. This can be achieved using the birefringence of uniaxial or biaxial crystals. They have two refractive indexes for a given direction of propagation $\vec{k}$, corresponding to two orthogonally polarized beams. By an appropriate choice of polarization and propagation direction it is possible to fulfill the phase matching condition

$$\Delta k = k_{2\omega} - 2k_\omega = 0, \tag{4.24}$$

due to

$$\Delta n = n_\omega - n_{2\omega} = 0. \tag{4.25}$$

The directions for the phase matched SHG-condition are obtained by considering the intersection of the ellipsoid of the refractive index for the fundamental and the second harmonic wave. Two types of processes are possible regarding the orientation of the incident fundamental beams: In Type I nonlinear processes, both polarization vectors are parallel while in case of Type II nonlinear processes, the polarization vectors are oriented orthogonally. Furthermore, a distinction between the so-called critical phase matching (CPM) and non-critical phase matching (NCPM) is done. In case of NCPM, the angle θ between an optical axis and $\vec{k}$ must be equal to 90° (90° NCPM) or 0° (0° NCPM), while in case of CPM, θ can differ from these values.
The birefringence of the nonlinear crystal compensates the phase difference between the fundamental wave and the SHG wave, but also affects the direction of the energy flux given by the different Poynting vectors $\vec{P}_\omega$ and $\vec{P}_{2\omega}$. This phenomenon is called the Poynting vector beam walk-off. In case of NCPM, no beam walk-off is occurring.

The following calculations are valid for intracavity SHG of a plane wave and no thermal effects in the laser medium. In this case, the power of the SHG-radiation can be calculated by [Agn02]

$$P_{2\omega} = \frac{\pi w_1^2}{8k} I_S^2 \left(-\left(k + \frac{L_i}{I_S}\right) + \left[\left(k + \frac{L_i}{I_S}\right)^2 + 4\frac{k}{I_S}\left(2K_C P_{abs} - L_i\right) \right]^{1/2} \right)^2 \tag{4.26}$$

with

$$k = \frac{4\pi^2}{\lambda_\omega^2} Z_0 \frac{d_{eff}^2 l^2}{n_{2\omega}^3} \frac{w_1^2}{w_2^2} \beta \tag{4.27}$$

Here, $I_S = h\nu_\omega/(\sigma_e \tau_{eff})$ denotes the saturation intensity, k is the effective nonlinearity of the nonlinear crystal in use, $Z_0 = 377\,\Omega$ represents the vacuum impedance, l is the length of the nonlinear crystal, $n_{2\omega}$ is the refractive index at $\lambda_{2\omega}$, w_1 and w_2 are the beam waists in the laser crystal and in the nonlinear crystal, respectively, and $\beta \approx 2$ is a factor that takes into account the phase mismatch between the fundamental and the second harmonic wave in the second pass through the nonlinear crystal. K_C, L_i, and P_{abs} denotes the small-signal gain coefficient, the linear cavity losses, and the amount of absorbed pump power, respectively. The output power is quadratically dependent on the absorbed pump power P_{abs} and the effective nonlinearity of the crystal. Furthermore, an increment in SHG power can be achieved by increasing the crystal length l and the effective nonlinear coefficient d_{eff}.

4.1.3 Active Q-Switching

The following paragraphs describe the basic principles of actively Q-switched laser operation. A more detailed overview can be found in [Sve89, Sie86, Koe99].

Figure 4.2 displays the dynamics of a Q-switched laser system. Initially, the cavity losses are high enough to suppress cw laser oscillation (a). During this time, gain is increasing

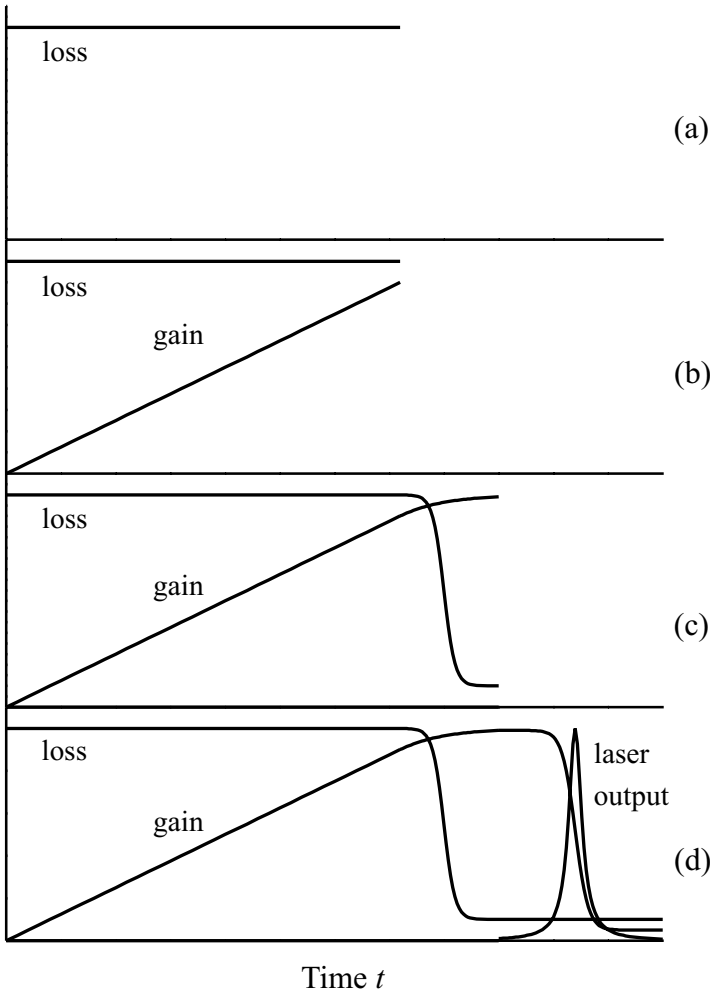

Figure 4.2: General dynamics of a Q-Switched laser system [Sie86]

until reaching a certain level (b). In the next step, the losses are fastly reduced to a very low level determined by the output coupling and the internal losses of the cavity (c). At this moment, the gain exceeds the laser threshold and the photon number in the cavity increases very fast and strongly, while the gain is reduced simultaneously. When the loss rate exceeds the gain in the active medium, the photon number reduces again and the inversion is below the level necessary for cw laser operation (d). At this point, losses are set to a high level again and the cycle starts anew.

The storable energy E_s in an active medium can be calculated by the formula

$$E_\mathrm{s} = V_\mathrm{L} h\nu_\mathrm{L} W_\mathrm{P} \tau_\mathrm{eff} \tag{4.28}$$

with

$$W_{\mathrm{P}} = \frac{f_2 \eta_{\mathrm{a}} P_{\mathrm{P}} \lambda_{\mathrm{P}}}{V_{\mathrm{L}} h c_0} \tag{4.29}$$

denoting the pump rate, and f_2 denoting the fraction of population determined by Boltzmann's equation of the upper laser level. η_{a} is the fraction of energy absorbed in the material featuring an absorption coefficient α and a thickness l given by $\eta_{\mathrm{a}} = 1\text{-}\exp(\alpha l)$.

The initial population inversion density n_{i} for a repetition rate f_{Q} is given by

$$n_{\mathrm{i}} = n\left(t = \frac{1}{f_{\mathrm{Q}}}\right) = W_{\mathrm{P}} \tau_{\mathrm{eff}} \left[1 - \exp\left(-\frac{1}{\tau_{\mathrm{eff}} f_{\mathrm{Q}}}\right)\right]. \tag{4.30}$$

To calculate the population inversion density after generating the pulse, n_{f}, the following assumptions will be made according to [Deg89]:

1. During the pump interval, both, pump rate and spontaneous decay are dominant. The laser photons inside the cavity are neglected resulting in the validity of Equation 4.30.
2. To determinate the pulse characteristics, only the fastest processes will be considered resulting in neglecting the pump rate and the spontaneous decay.
3. The Q-switching process is instantaneous and will only be considered by the boundary conditions.

These assumptions give a result for the inversion population n_{t} in case of the interval where the Q-switch is off (low loss regime):

$$n_{\mathrm{t}} = \frac{1}{2\sigma_{\mathrm{e}} l}\left[\ln\left(\frac{1}{R}\right) + L_{\mathrm{i}}\right] \tag{4.31}$$

Here, R is the reflectivity of the output coupling mirror.

With these results, the inversion population after pulse generation n_{f} can be determined by

$$n_{\mathrm{i}} - n_{\mathrm{f}} = n_{\mathrm{t}} \ln\left(\frac{n_{\mathrm{i}}}{n_{\mathrm{f}}}\right). \tag{4.32}$$

With the values of n_{i}, n_{f} and n_{t} the pulse peak power $P_{\max}$, the pulse energy E_{P} and a rough value of the pulse duration Δt assuming a rectangular shape can be calculated:

$$P_{\max} = \frac{V h \nu_{\mathrm{L}} c_0}{2L'} \cdot \ln\left(\frac{1}{R}\right)\left\{n_{\mathrm{i}} - n_{\mathrm{t}}\left[1 + \ln\left(\frac{n_{\mathrm{i}}}{n_{\mathrm{f}}}\right)\right]\right\} \tag{4.33}$$

$$E_P = V_{\mathrm{L}} h \nu_{\mathrm{L}} (n_{\mathrm{i}} - n_{\mathrm{f}}) \frac{\ln\left(\frac{1}{R}\right)}{\ln\left(\frac{1}{R}\right) + L_{\mathrm{i}}} \tag{4.34}$$

$$\Delta t \approx \frac{E_\mathrm{P}}{P_\mathrm{max}} \tag{4.35}$$

For estimation purposes the usable amount of energy E_max stored in the laser crystals can be approximated by

$$E_\mathrm{max} = P_\mathrm{max,cw}\tau_\mathrm{eff}. \tag{4.36}$$

Here $P_\mathrm{max,cw}$ denotes the maximum of the output power obtained in the cw experiments at the same pumping level. The pulse efficiency η_P can be calculated by

$$\eta_\mathrm{P} := \left.\frac{E_\mathrm{P}}{E_\mathrm{max}}\right|_{P_\mathrm{abs}} = \left.\frac{E_\mathrm{P}}{P_\mathrm{max,cw}\tau_\mathrm{eff}}\right|_{P_\mathrm{abs}}. \tag{4.37}$$

It resembles the fraction of the extracted pulse energy with respect to the maximally storable energy.

4.2 Pumping Sources

4.2.1 Optically Pumped Semiconductor Lasers

Optically pumped semiconductor lasers are part of the VECSEL[2] technology and combine several key technologies. The laser cavity has a thin-disk geometry where the RE-doped dielectric crystal is replaced by a semiconductor chip. Thus, the beam quality of the laser radiation is enhanced in comparison to widely used semiconductor edge emitters. The resulting laser beam is circular and nearly diffraction limited. Due to the disk laser setup, the thermal gradient is along the optical axis and does not affect the beam quality in case of higher output powers. The semiconducting chip, namely a surface-emitting semiconductor active mirror structure, is pumped optically. The semiconductor chip contains a distributed Bragg reflector structure over which an active region featuring several quantum wells is grown. Due to the broad absorption characteristics, no constraint in wavelength stability of the pump laser is imposed. The absorption length is typically $\approx 0.8\,\mu m$ so that the pump radiation can be absorbed efficiently in a single or double pass even in case of thin active regions. Those carriers created by optical pumping are trapped subsequently in the quantum wells. The gain bandwidth, differential gain, peak gain wavelength, and quantum efficiency depend sensitively on carrier concentration and temperature. Therefore, the active mirror is affected by the pump power level, the pump spot size and the thermal coupling to the heat sink. The gain bandwidth is typically some tens of nanometers. Depending on the utilized semiconductor material systems and the dimensions of the quantum well structure, the central wavelength of emission can be tuned from 850 nm to more than 1000 nm in case of GaAs/AlGaAs layers. By increasing the pump power, the active region spacially changes, which results in a red-shift of the laser wavelength of about $0.01\,nmK^{-1}$, and a reduced differential gain leading to the so-called "thermal overrolling". Thus, the output power of an OPSL is limited to a certain output power level depending on the temperature of the active region. By using different semiconducting materials, lasing could also be demonstrated at 660 nm with InGaP quantum wells [Mue02] and at 397 nm with a GaN-based VCSEL[3] [Par03]. So far, OPSLs can not emit in the visible spectral region due to lack of suitable semiconductors. However, by means of SHG, visible radiation has been generated in the blue, green, yellow, orange and red spectral region.

The OPSL system used in the laser experiments in the context of this work is an intra-cavity frequency doubled laser system and emits at a wavelength of 479.5 nm featuring a slight tunability. Its laser cavity is displayed in Figure 4.3. A laser diode emitting at a wavelength of 808 nm is the pump source for the OPS-chip. The cavity consists of two external mirrors, enabling a single folded V-type cavity. The cavity features a second beam waist in the arm M_1-M_2, where the nonlinear crystal lithium triborate (LiB_3O_5, LBO) is mounted. The cavity is highly reflective for the fundamental wavelength at about 960 nm,

[2]VECSEL: vertical external cavity surface emitting laser
[3]VCSEL: vertical cavity surface emitting laser

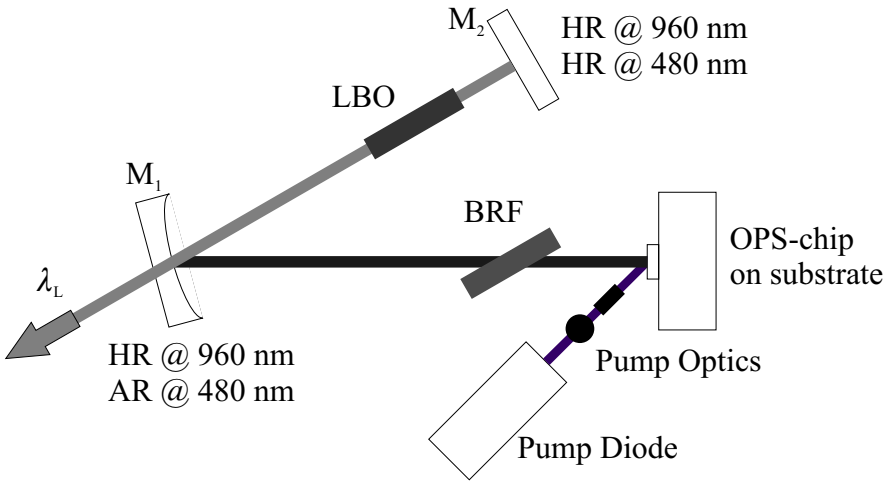

Figure 4.3: Schematic set-up of an OPSL used as a pump source for the laser experiments.

OPS System	Maximal power P_{max}	Beam quality M_x^2, M_y^2	Beam diameters d_x, d_y (µm)
MOPS	300 mW	< 1.1, < 1.1	700, 700
HOPS	1600 mW	< 1.1, < 1.1	1900, 1980
miniG	4500 mW	≈ 4.5, ≈ 1.9	180, 120

Table 4.1: Optical parameters of the used OPSL for pumping

while the visible radiation of about 479.5 nm is coupled out at the folding mirror M_1. To fix the operating wavelength of the OPSL, a birefringent filter (BRF) is inserted into the cavity. The OPSL-pumped laser experiments done in the framework of this thesis have been done with three different OPSL systems. Their optical parameters are listed in Table 4.1. While the MOPS-system (MOPS: Medium power OPSL) providing an output of 300 mW was the first OPSL available for laser experiments, the power scaled version (HOPS: High power OPSL) could provide up to 1.6 W of pump power at ≈480 nm. The miniG-system is a new generation of OPSL featuring even higher output powers with a reduced package size. With this technology, up to 15 W at 488 nm and 5 W at 460 nm could be demonstrated to date [Chi04]. However, the OPS-chips used in the high power experiments suffered from degradations resulting in a reduced chip lifetime.

4.2.2 GaN-based laser diodes

This section gives a short introduction to some properties of GaN, the manufacturing process of the optically active layers, and the performance of commercially available GaN-based laser diodes (GaN-LDs). A more detailed description can be found in Nagahama [Nag01] and Nakamura [Nak97].

GaN is a III-V-semiconductor featuring a direct band gap. Depending on the addition of In or Al, the band gap energy can be varied between 2.0 eV (16100 cm^{-1}) and 6.2 eV (50000 cm^{-1}). Due to the large lattice mismatch of 15% between the substrate and the GaN-layer, the production of high quality InGaN-layers on sapphire suffered from a large number of threading dislocations from $1\times10^{8}cm^{-2}$ to $1\times10^{12}cm^{-2}$ [Les95, Chi96]. The efficiency of InGaN-based LEDs[4] and laser diodes, however, is comparable to GaAs-based devices. Several approaches which reduce the density of defects such as using ELOG[5] as substrate [Usu97, Nam97] or applying AlGaN/GaN modulation-doped strained-layer superlattices (MD-SLSs) as cladding layers have improved the material quality. However, further development of the fabrication process is still necessary.

GaN-LDs are under investigation since 1996. While the first devices which were commercially available in 1999 provided low optical powers (5 mW) in the ultraviolet spectral region around 409 nm [Nak99], both output powers and the available wavelength range were improved. By variation of the In-content in the active layer, GaN-LDs cover the spectral range from 370 nm (UV) to 478 nm (blue). As a side effect, the increasing amount of In also rises the threshold current density. Thus, the lifetime of GaN-LDs operating in the long wavelength region is significantly below 10000 hours. At the wavelength region of interest for pumping Pr^{3+}-based lasers, engineering prototypes with output powers of more than 0.5 W of optical power in the wavelength region between 440 nm and 450 nm are commercially available. The electro-optical efficiency of these LDs is 16%.

The laser wavelength of semiconductor lasers is temperature-dependent. While the wavelength shift for GaAs-based laser diodes is about 0.2 nmK^{-1}, the tuning coefficient for GaN-LDs is as low as 0.07 nmK^{-1}. By adjusting the temperature of the laser diode using a temperature controller, fixing the laser wavelength is possible. However, due to the package design of the LDs, compensation of the wavelength shift is challenging. Figure 4.4 shows the typical wavelength shift of a temperature stabilized GaN-LD with increasing current. The wavelength of the investigated device shifts about 2.84 nm, which corresponds to a shift in temperature of about 40.6 K. During these measurements, the LD-package temperature was kept constant at 29°C. Thus, efficient cooling is necessary to compensate the current-induced wavelength shift. Regarding the beam quality of GaN-LDs, both beam divergence and transversal shape depend on the dimensions of the facet of the optically active layer. Typical facet dimensions of a 0.5 W multimode LD are 1 µm × 10 µm. The beam divergence angle is about 30° and 10° for the fast and the slow axis, respectively. While the beam quality of the fast axis is close to the diffraction limit

[4] LED: light emitting diode
[5] ELOG: epitaxially laterally overgrown GaN

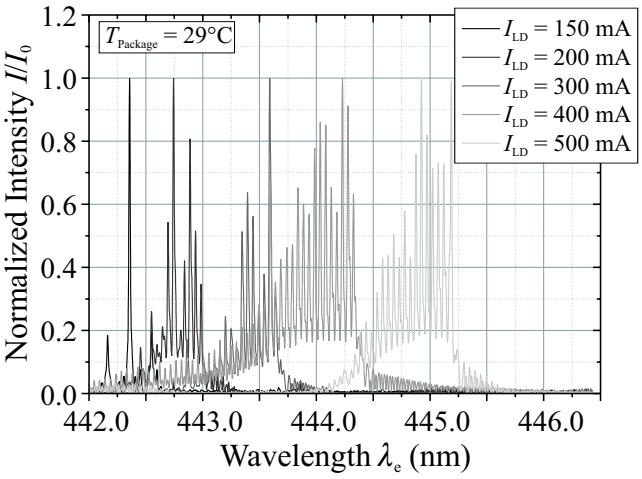

Figure 4.4: Emission spectra of a GaN-LD operated at different currents

($M^2 \approx 1$), the beam quality factor M^2 is about 3 for the slow axis. Due to the differences in divergence and spot dimensions, several optical elements for beam shaping are necessary. For example, an aspherical lens and anamorphic beam shaping optics can generate a collimated beam featuring a circular beam cross-section. To overcome the reduced beam quality of LDs, a combination of the GaN technology and VECSELs is promising. Studies of combining the VECSEL-geometry with GaN-active layers are subject to the actual research [Fee07].

4.3 Cavity Setup

In the following subsections, the cavity setups used for the laser experiments will be presented. A short discussion regarding the expectable overlap efficiencies will be given herein as well.

4.3.1 Fundamental Wave Operation Setup

OPSLs as Pump Source

For the fundamental wave operation the HOPS laser system was used as a pump source. The linear setup shown in Figure 4.5 was applied for the Pr^{3+}-lasers. It consists of two mirrors M_1 and M_2 with 50 mm radius of curvature (R_{OC}) each. They were installed at a distance of 80 mm – 84 mm, depending on the crystal thickness. The calculations regarding the overlap efficiency assume Gaussian beam profiles of the laser and pump beam. They were performed using the ABCD matrix formalism [Kog66] integrated in the WinLase software.

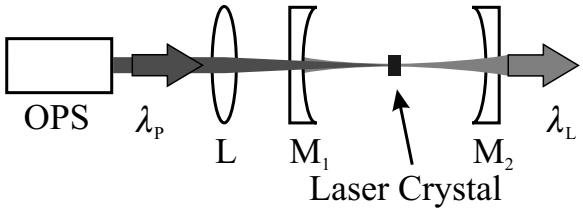

Figure 4.5: Schematic setup of the Pr^{3+}-lasers under OPSL-pumping

The pump radiation from the HOPS laser was focused into the laser crystal using a lens L with a focal length of $f = 100$ mm. Figure 4.6 displays the resulting beam radii of the pump beam and the laser mode in case of different laser wavelengths inside the cavity. The overlap efficiency was calculated as follows: After determination of the tangential (t) and sagittal (s) radii of both pump beam r_P and laser mode r_L at a certain position z inside the laser crystal, the areas of both beams were calculated by

$$A_P(z) = \pi r_{Ps}(z) \times r_{Pt}(z) \tag{4.38}$$

$$A_L(z) = \pi r_{Ls}(z) \times r_{Lt}(z). \tag{4.39}$$

In the next step, the overlap efficiency η_O was calculated for each position z to

$$\eta_O(z) = \left(\frac{A_P(z)}{A_L(z)}\right)^{\mathrm{sgn}(A_L(z)-A_P(z))}, \tag{4.40}$$

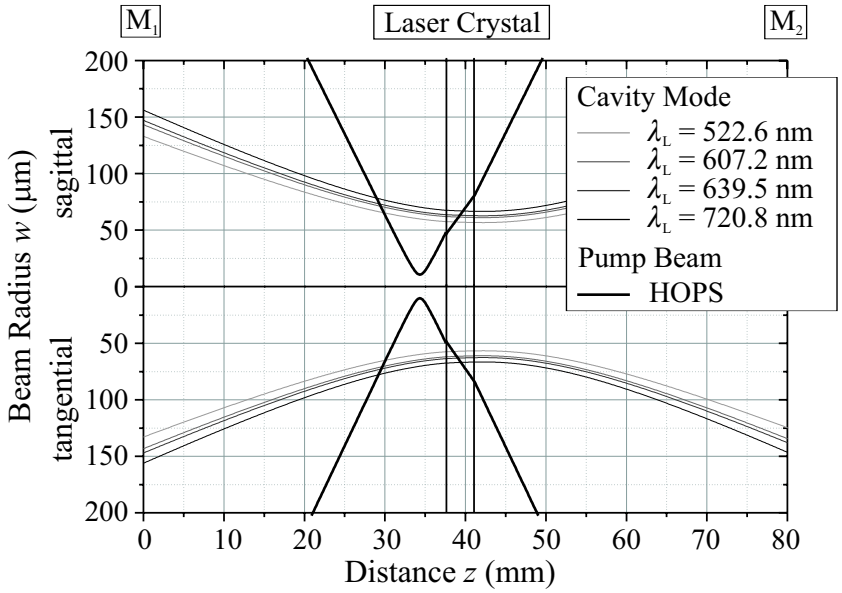

Figure 4.6: Beam radius plot inside the cavity for the HOPSL pump radiation and the laser operating at different laser wavelengths

where sgn(x) denotes the sign function[6] of x. The total overlap efficiency is the average of $\eta_O(z)$ inside the active medium. In case of OPSL-pumping, the maximum overlap efficiency achieved was 0.77 in case of the 3.45 mm Pr^{3+}:YLF and 0.80 in case of the 3.00 mm Pr^{3+}:LLF. This value is reasonable and a direct result of different properties of the pump beam and the laser mode in the active medium. The Rayleigh length z_R (Eqn. 4.20) for the geometry of the cavity in use was $z_R = 0.7$ mm and $z_R = 19.8$ mm for the pump and the laser beam, respectively. Although the discrepancy is large, using a more suitable focal lens with $f = 450$ mm would result in a higher laser threshold and an extensive laser system[7]. From the handling point of view the alignment process for both focal lengths is difficult: for a small focal length the longitudinal range of the highest overlap is small while in case of a large focal length the range of transversal alignment is narrow. The more convenient choice, however, is the lens with the short focal length.

GaN-LDs as Pump Source

The laser experiments with GaN-LDs as pump source were performed using the setup shown in Figure 4.7. Two collimated and beam-shaped GaN-LDs with 500 mW of pump power each were used to pump the laser crystal from both sides. The Pr^{3+}-doped crystal was mounted at the position of the beam waist of a single folded cavity consisting of three

[6]The sign function sgn(x) is defined as sgn(x)=1: x > 0, sgn(x)=0: x = 0, and sgn(x)=-1: x < 0

[7]Geometrical considerations of the pump geometry in longitudinally pumped laser rods resulted in a (r_P^2+r_L^2)-dependence of the laser threshold [Ris88].

mirrors. The input coupler for laser diode LD_1, namely M_1, had a R_{OC} of 50 mm while the second input coupling mirror M_2, used for laser diode LD_2, was a plane mirror at a folding angle of 26° in total. The output coupling mirror M_3 had a R_{OC} of 100 mm. The cavity length was measured to be in the range of 140 mm to 150 mm. Figure 4.8 shows the beam radii in case of a 17.1 mm Pr^{3+}:YLF-crystal in a 141 mm cavity for different laser transitions. Additionally, the characteristics of the pump beams from LD_1 and LD_2 are shown. The beam characteristics of the laser modes differ from the pump radiation as in the case of OPSL-pumping. Thus, the overlap efficiency η_O of each LD is significantly below 1.0.

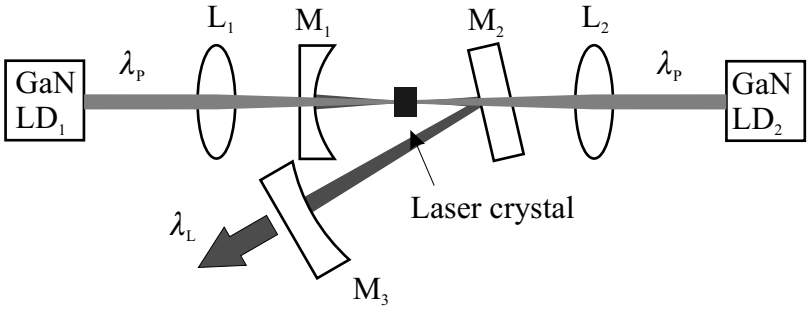

Figure 4.7: Schematic setup of the Pr^{3+}-lasers pumped by two GaN-LDs

In the following estimations two ideally collimated pump beams are assumed. Two $f = 50$ mm lenses focus the pump radiation into laser crystals of different lengths located at the centre of the beam waist of the cavity mode. In case of a a 2.2 mm thick crystal, the upper limit of η_O was about 0.76 for each laser diode. By pumping with two diodes simultaneously, the achievable limit of η_O is 0.97. Figure 4.9 (a) shows the resulting limits of efficiency for each LD and in case of double side pumping with respect to the crystal length. In Figure 4.9 (b), the corresponding efficiencies are shown for a 17 mm long crystal with respect to the position inside the crystal. In the experiments, the optimal overlap of LD_2 was set up first and then only LD_1 was adjusted for maximum laser output. The positions of the other components were not changed anymore. In this way, the achieved overlap efficiency was for a 4.7 mm crystal for example ≈ 0.70 in contrast to the calculated limit of ≈ 0.90. To improve η_O for each LD, the focal lengths of the focusing lenses have to be close to $f_1 = 450$ mm and $f_2 = 500$ mm for LD_1 and LD_2, respectively. In this case the threshold pump power will increase and an increased distance between the LDs and the laser cavity results in a less compact laser system.

4.3.2 Second Harmonic Generation Setup

The setup for SHG under OPSL-pumping is displayed in Figure 4.10. The setup is a V-type cavity consisting of three curved mirrors. The input coupling mirror M_1 had a R_{OC} of 50 mm, the folding mirror M_2, which is also one of the output couplers, had

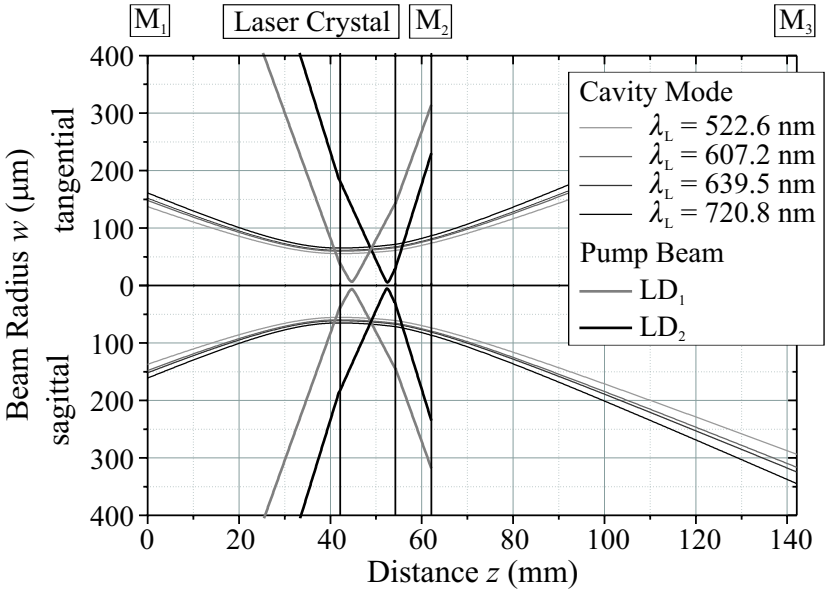

Figure 4.8: Radii of the pump beams provided by two GaN-LDs and the laser radiation in case of different transitions

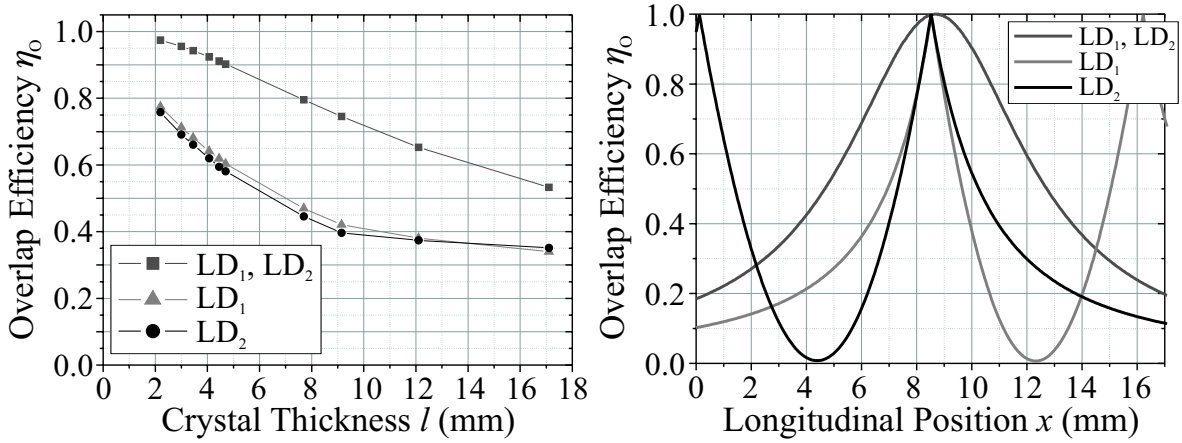

(a) (b)

Figure 4.9: (a) Overlap efficiency η_O with respect to the crystal thickness l and (b) dependence of the overlap efficiency on the position x inside a 17 mm long Pr^{3+}:YLF sample

$R_{OC} = 100\,\text{mm}$ and M_3 was a $R_{OC} = 50\,\text{mm}$ mirror. The folding angle was about 30° in total and the cavity length was in the range from 260 mm to 270 mm, depending on the thickness of the nonlinear and the laser crystal. As nonlinear medium, LBO was used

for frequency conversion of the visible radiation at ≈640 nm to the UV at 320 nm. The main advantages of this material are a wide transparency range from 0.12 µm to 2.6 µm, a high optical damage threshold and a large temperature acceptance of ≈9.3 cmK. The nonlinear coefficient d_{eff} for the investigated process is about 0.54 pm/V. Three crystals, cut for Type I CPM ($\theta = 90°$, $\phi = 53.5°$) with lengths of 3 mm, 5 mm and 8 mm were used. Both surfaces of the crystals were antireflection (AR)-coated for 640 nm and 320 nm. They were provided by Ekspla Company in Lithuania. The beam radius plot of the laser mode is displayed in Figure 4.11. The beam properties inside the nonlinear crystal feature an ellipticity of $\epsilon = 0.85$ and a beam diameter of ≈71 µm.

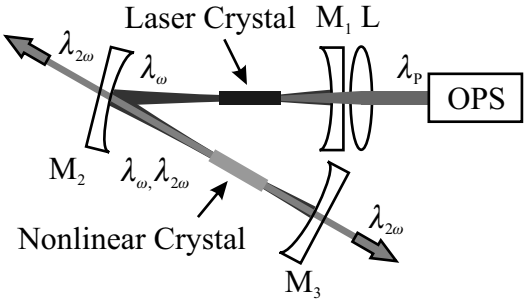

Figure 4.10: Schematic setup for SHG of OPSL-pumped Pr^{3+}-lasers operated at the transition ${}^3P_0 \rightarrow {}^3F_2$

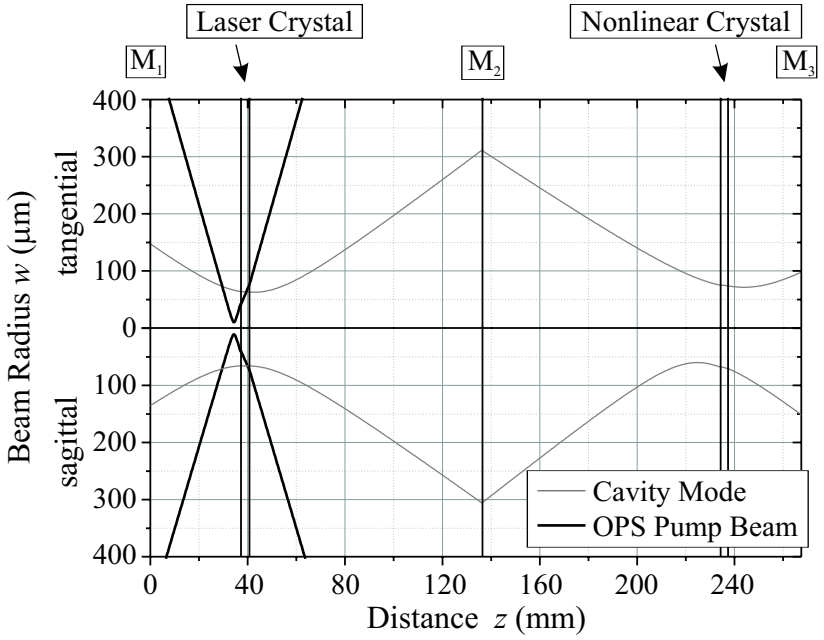

Figure 4.11: Beam characteristics of the OPSL-pump radiation and the laser mode for the SHG setup displayed in Figure 4.10

First results of SHG using GaN-LD-pumped Pr^{3+}-lasers were performed in the Z-type cavity displayed in Figure 4.12. This setup consists of the input coupling mirrors M_1 ($R_{OC} = 50\,mm$) and M_2 ($R_{OC} = \infty$), the output coupling mirror M_3 with $R_{OC} = 100\,mm$, and the end mirror M_4 with a radius of curvature of 50 mm. The total cavity length was 280 mm and the folding angles at M_2 and M_3 were 44° in total. The mean beam diameter in the nonlinear crystal was 71 µm featuring an ellipticity of $\epsilon \approx 0.66$.

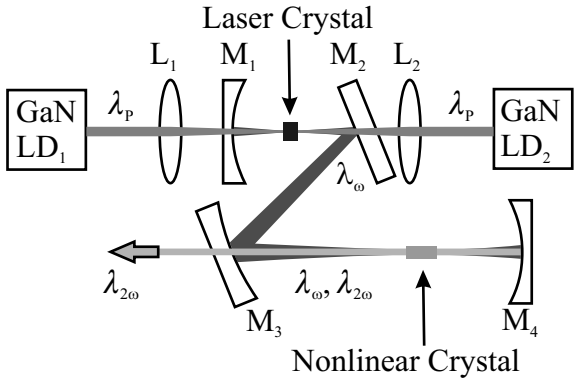

Figure 4.12: Schematic setup for SHG of GaN-LD-pumped Pr^{3+}-lasers operated at the transition ${}^3P_0 \rightarrow {}^3F_2$

As result, the transversal profile of the generated UV beam is astigmatic as well. The curved end mirror leads to a more challenging and complex alignment procedure. The main advantage of this cavity setup is the possibility to place the nonlinear crystal in the centre of the beam waist and thus obtaining near optimum conversion efficiencies.

4.3.3 Active Q-Switching Setup

Q-switching of Pr^{3+}-lasers has been performed by using an acoustooptical modulator (AOM) inside the laser cavity. The AOM used in the experiments consists of a fused silica block. Piezoelectric elements located on one side of the block induce supersonic waves transversal to the optical axis. An absorber mounted on the other side of the material suppresses the formation of a standing wave. Due to the photoelastic effect, the acoustic wave modulates the refractive index in the silica block. The changes in the refractive index are directly proportional to the amplitude of the acoustic wave. The resulting optical grating in the AOM-material adds diffraction losses for the propagating laser beam. If the RF-signal at the piezoelectric elements is switched off, the diffraction losses and the grating vanish and the pulsing process is initiated. The AOM used in the experiments was cut in Brewster's angle for the visible spectral range from 500 nm to 750 nm and had an optical path length of $\approx 50\,mm$. It was designed for a maximal beam radius of 300 µm. To obtain reasonable modulation depths, the passing laser beam should be collimated. The setup for active Q-switching is shown in Figure 4.13. It consists of a focusing lens L with a focal length of $f = 200\,mm$, an input coupling mirror M_1 with

a radius of curvature of 100 mm, a folding mirror M_2 ($R_{OC} = 200$ mm) forming an angle of 24°, and a plane output coupling mirror M_3. The cavity length slightly exceeded 350 mm. In this geometry, the average laser beam radius inside the AOM is ≈ 200 µm and almost completely collimated, resulting in sufficient modulation depths. As pump source, a 4.5 W OPSL called miniG was used. Its beam quality factors were $M_x^2 = 4.5$ and $M_y^2 = 1.9$, resulting in an astigmatic pump profile. The calculated overlap efficiencies were in the range from 0.6 to 0.8.

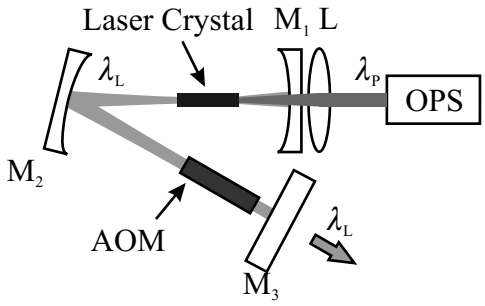

Figure 4.13: Schematic setup of the OPSL-pumped Q-switch experiments of Pr^{3+}-lasers

4.4 Results of OPS-pumped Pr-lasers

While the first Pr^{3+}-lasers realized were pumped by pulsed dye laser systems [Est77] or flashlamps [Kam98], different approaches for direct blue laser pumping of Pr^{3+}-ions were performed for example by Ar-ion lasers [San94b] or frequency doubled Nd:YAG ground state lasers [Heu99] in the last ten years. However, only a minor part of the pump radiation was absorbed in the Pr^{3+}-doped material due to the lack of overlap between the pump wavelengths and the absorption peaks of Pr^{3+}. A low power frequency doubled OPSL of suitable wavelength ($\approx 480\,\mathrm{nm}$) was available in our laboratory to demonstrate a compact and efficient cw Pr^{3+}:YLF-laser in 2004 for the first time [Osi04]. In the last three years, intracavity SHG experiments demonstrated efficient generation of UV radiation at 261 nm and at 360 nm with about 1 W of output power [Ost07a, Ost07b].

4.4.1 Fundamental Wave Experiments

In the context of this work, efficient laser oscillation of Pr^{3+}-doped YLF and LLF at high power levels has been demonstrated under HOPS-pumping at $\approx 480\,\mathrm{nm}$. Different laser wavelengths in the visible spectral range from the green spectral region ($\approx 523\,\mathrm{nm}$, transition $^3P_1 \rightarrow {}^3H_5$) to the near infrared at $\approx 721\,\mathrm{nm}$ (transition $^3P_1 \rightarrow {}^3F_4$) could be demonstrated. Table 4.2 gives the realized laser transitions with corresponding wavelengths and quantum defect η_Q of the transitions under HOPS-pumping. Additionally, the realized overlap efficiency η_O (cf. Section 4.3.1) and the maximum expectable slope efficiency $\eta_\mathrm{S,max} = \eta_\mathrm{Q} \times \eta_\mathrm{O}$ is given as well.

Laser transition	λ_L (nm)	η_Q	η_O	$\eta_\mathrm{S,max}$
YLF				
$^3P_1 \rightarrow {}^3H_5$	522.6	0.92	0.76	0.70
$^3P_0 \rightarrow {}^3H_6$	607.2	0.79	0.74	0.58
$^3P_0 \rightarrow {}^3F_2$	639.5	0.75	0.77	0.58
$^3P_0 \rightarrow {}^3F_4$	720.8	0.66	>0.77	>0.51
LLF				
$^3P_1 \rightarrow {}^3H_5$	523.9	0.91	0.78	0.71
$^3P_0 \rightarrow {}^3H_6$	607.0	0.79	0.78	0.62
$^3P_0 \rightarrow {}^3F_2$	640.1	0.75	0.80	0.60
$^3P_0 \rightarrow {}^3F_4$	721.4	0.66	>0.79	>0.52

Table 4.2: Overview of quantum defect η_Q, overlap efficiency η_O, and the upper limit of the slope efficiency $\eta_\mathrm{S,max}$ of different Pr^{3+}:YLF- and Pr^{3+}:LLF-laser transitions under OPSL-pumping

The laser crystals used in these experiments were a 3.45 mm long Pr^{3+}(0.65at.%):YLF crystal and a 3.0 mm long Pr^{3+}(0.45at.%):LLF crystal. They were cut along the $\vec{a}$-axis.

The facets have been polished in laser quality and had no anti reflection coatings. The pump radiation was linearly polarized and the crystals were oriented for $\vec{E}\|\vec{c}$ to make use of the large absorption coefficient and thus a high absorption efficiency in the crystal (cf. Figure 3.9). The amount of absorbed power in a single pass was determined to be 91% and 73% for Pr^{3+}:YLF and Pr^{3+}:LLF, respectively. The Pr^{3+}-doped BYF- and KYF-crystals could not be characterized in this setup due to the limited tunability range of the HOPS pump laser system.

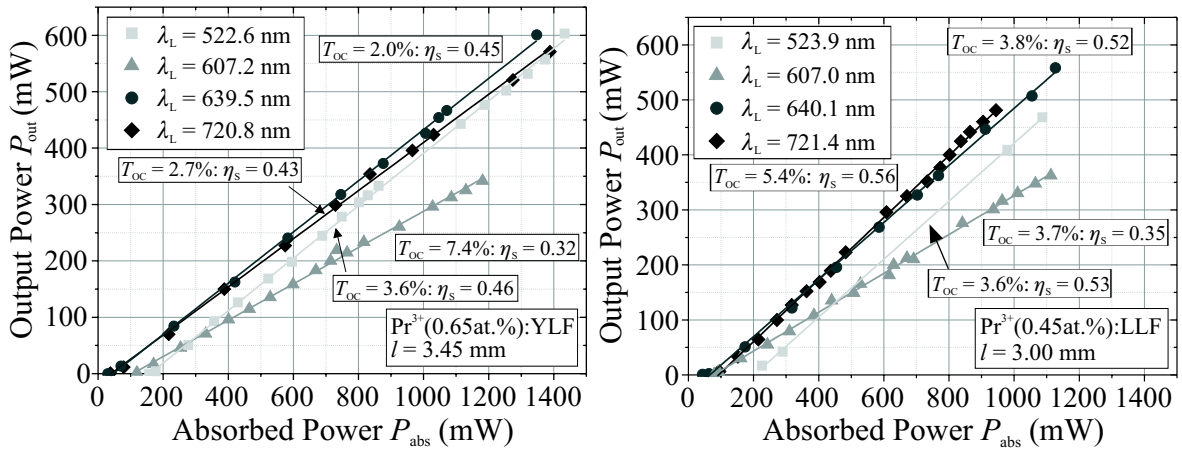

(a) (b)

Figure 4.14: Power characteristics of OPSL-pumped (a) Pr^{3+}:YLF and (b) Pr^{3+}:LLF operating at different transitions

Figure 4.14 (a) and (b) show the power characteristics with the highest slope efficiencies for the 3.45 mm long Pr^{3+}(0.65at.%):YLF and the 3.00 mm long Pr^{3+}(0.45at.%):LLF samples under HOPS-pumping, respectively. At an absorbed pump power of around 1.4 W, up to 600 mW of coherent green and red radiation was emitted from the laser set-up with slope efficiencies η_S of up to 0.46. To the best of our knowledge, this was the highest slope efficiency of a semiconductor laser pumped Pr^{3+}:YLF laser so far. The realized orange Pr^{3+}:YLF-laser at 607.2 nm enabled an output power of about 350 mW with $\eta_S = 0.32$. Figure 4.14 (b) shows the power characteristics of OPSL-pumped Pr^{3+}:LLF laser for the same transitions in the visible spectral range. Using the LLF crystal, more than 550 mW of laser radiation was emitted with a slope efficiency of 0.52 at the transition $^3P_0 \rightarrow {}^3F_2$ at 640.1 nm, while the laser power on the transitions $^3P_1 \rightarrow {}^3H_5$ at 523.9 nm and $^3P_0 \rightarrow {}^3F_4$ at 720 nm were about 500 mW with slope efficiencies η_S of 0.53 and 0.56, respectively. The orange laser transition ($^3P_0 \rightarrow {}^3H_6$) of Pr^{3+}:LLF at 607.0 nm shows a lower output of about 370 mW with a slope efficiency η_S of 0.35 with respect to the absorbed pump power, as already observed in YLF. In contrast to former laser results of Pr^{3+}:YLF lasers under argon ion laser pumping [San94b] no drop of the output power was observed during the laser experiments. The optimal transmission of the output couplers available of the

Pr^{3+}:YLF(Pr^{3+}:LLF) laser operating at 523 nm, 607 nm, 640 nm and 721 nm were 3.6% (2.1%), 7.4% (3.7%), 2.0% (3.8%) and 2.7% (5.4%), respectively. Internal losses of the lasers were estimated by a Findlay-Clay analysis and by the method of Caird. The internal losses per roundtrip were estimated to be about 0.6% for both Pr^{3+}:YLF and Pr^{3+}:LLF lasers emitting at $\approx$640 nm and $\approx$721 nm. In case of the shorter wavelengths, the internal losses were higher. Table 4.3 contains the results of the loss determination by both methods. In case of the orange laser transition of Pr^{3+}:YLF, the maximal obtainable slope efficiency from the Caird plot is larger than the quantum defect η_Q, indicating large uncertainties of this method. Loss values for the transition in the green spectral range could not be determined by any method. The reason might be changes of the pump laser beam position inside the laser crystal during the experiments due to changing the input coupling mirror M_1 and thus different gain conditions.

Laser transition	λ_L (nm)	$\gamma_{i,FC}$ (%)	$\gamma_{i,CA}$ (%)	η_Q
YLF				
$^3P_1 \rightarrow {}^3H_5$	522.6	–	–	–
$^3P_0 \rightarrow {}^3H_6$	607.2	1.8	12.0	0.93
$^3P_0 \rightarrow {}^3F_2$	639.5	0.7	0.7	0.53
$^3P_0 \rightarrow {}^3F_4$	720.8	0.7	0.6	0.50
LLF				
$^3P_1 \rightarrow {}^3H_5$	523.9	4.3	4.7	0.81
$^3P_0 \rightarrow {}^3H_6$	607.0	3.3	2.2	0.47
$^3P_0 \rightarrow {}^3F_2$	640.1	3.9	0.3	0.54
$^3P_0 \rightarrow {}^3F_4$	721.4	0.5	0.6	0.57

Table 4.3: Overview of the determined residual internal roundtrip losses γ_i and the limits of the slope efficiency η_Q calculated from the Caird analysis for the Pr^{3+}:YLF- and Pr^{3+}:LLF-laser crystals used in the OPSL-pumping experiments. Loss determination failed for the transitions indicated by lines (–)

The limit of influence of CRPs on the slope efficiency can be estimated by Equation 4.16. Due to differences in σ_e and the initial decay characteristics, different intensity limits I_{lim} were calculated for the Pr^{3+}:YLF and Pr^{3+}:LLF samples used in the laser experiments. The results are given in Table 4.4. If the stimulated lifetime falls below 13 µs in case of YLF or 11 µs in case of LLF, the influence of CRPs should become less important. Corresponding to these time constants, the laser intensity I must exceed the saturation intensity I_S by a factor of 2.6 and 3.1 for YLF and LLF, respectively. For the Pr^{3+}:YLF crystal, this is achieved when the laser output exceeds 0.27 W at 639.5 nm or 4.12 W at 522.6 nm.

Identification of the process influencing laser transition $^3P_0 \rightarrow {}^3H_6$

Loss estimations for the laser transition $^3P_0 \rightarrow {}^3H_6$ resulted in values of more than 10% for Pr^{3+}:YLF with the method of Caird. Due to the reduced doping level of the Pr^{3+}:LLF

λ_L (nm)	T_{OC} (%)	I_S (kW cm^{-2})	I_{lim} (kW cm^{-2})	P_{abs} (W)	P_{out} (W)
Pr^{3+}(0.65 at.%):YLF, $\tau_{eff} = 34\,\mu s$, $\tau_{lim} = 13\,\mu s$					
522.6	3.6	428	1120	9.0	4.12
607.2	7.4	70	184	5.2	1.62
639.5	2.0	42	109	0.6	0.27
720.8	2.7	92	241	2.2	0.92
Pr^{3+}(0.45 at.%):LLF, $\tau_{eff} = 34\,\mu s$, $\tau_{lim} = 11\,\mu s$					
523.9	3.6	474	1460	10.4	5.37
607.0	3.7	81	251	3.2	1.10
640.1	3.8	43	134	1.3	0.63
721.4	5.4	112	347	4.8	2.64

Table 4.4: Saturation intensities I_S, intensity limits for effects of CRPs I_{lim}, and the amount of absorbed power P_{abs} and the resulting laser output power P_{out} for the conditions where τ_S equals the initial decay constant

sample, the corresponding losses were slightly above 2%. A possible reason is an efficient reabsorption process originating from the Stark level at 213 cm^{-1} above the lowest state of the $^3H_4$ level and terminating in one of the Stark levels of the $^1D_2$ energy level. Such absorption could limit the slope efficiency of this laser transition.
To confirm this supposition, emission spectra of Pr^{3+}:YLF were recorded during laser operation in the orange spectral range. By comparing the resulting spectra with the results from regular fluorescence measurements, further information can be gained. Figure 4.15 displays the unpolarized fluorescence spectrum of the Pr^{3+}(0.65at.%):YLF laser crystal obtained under laser oscillation in the spectral region from 450 nm to 750 nm. The spectrum is not corrected for the spectral response of the measurement setup. Thus, an uncorrected emission spectrum is displayed as well. The two spectra show different spectral characteristics at about 607.2 nm and around 594.7 nm. While the former can be assigned to scattered laser photons, the increase in signal in the latter spectral region corresponds to the ground state transition originating from the $^1D_2$ energy level. This increase in luminescence intensity is a direct result of an increased population number of the $^1D_2$ energy state due to the ground state absorption process $^3H_4 \rightarrow {}^1D_2$ occurring at the laser wavelength. Unlike reabsorption processes occurring in 3-level-laser systems, the absorption of laser photons in this system does not increase the population of the upper laser level ($^3P_0$) but effectively removes laser photons from the cavity. The comparably long lifetime of the $^1D_2$ energy level of several hundreds of microseconds results in a reasonable amount of the excitation energy which is lost for the laser oscillation process. The reabsorption process is compensated if the population of the $^1D_2$ energy level equals that of the corresponding Stark level of the $^3H_4$ energy level. This can be achieved by a high intensity pumping process, but with the pump sources available the limit has not been reached so far.

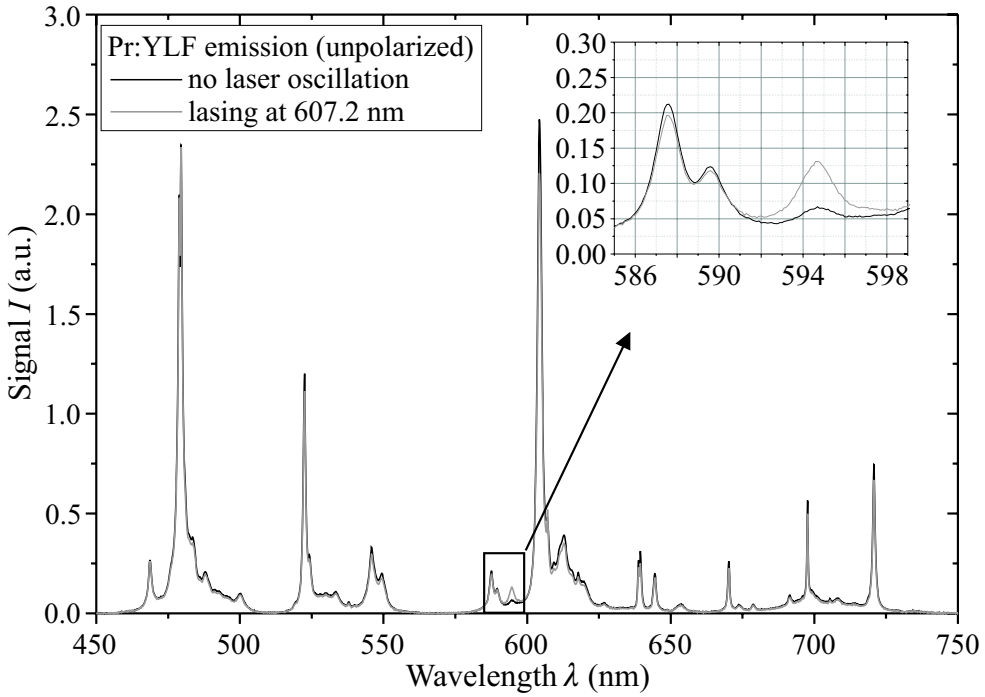

Figure 4.15: Unpolarized emission spectra of Pr^{3+}:YLF under $^3P_0$-excitation. The black line resembles the regular fluorescence curve while the gray line resembles the spectrum recorded under laser oscillation at transition $^3P_0 \rightarrow {}^3H_6$

Beam parameters

The laser radiation has also been investigated regarding the beam quality factor M^2 using the measurement device BeamScope-P7. Table 4.5 displays the results for the different laser transitions at a pumping power level of 300 mW. As expected from longitudinally pumped solid-state lasers, the beam quality factor is below 1.3 with respect to both transversal axes, corresponding to an almost diffraction limited beam featuring a Gaussian intensity profile.

Transition	Beam quality factors	
	M_x^2	M_y^2
${}^3P_1 \rightarrow {}^3H_5$	1.2	1.1
${}^3P_0 \rightarrow {}^3H_6$	1.2	> 1.0
${}^3P_0 \rightarrow {}^3F_2$	1.2	1.1
${}^3P_0 \rightarrow {}^3F_4$	1.2	1.2

Table 4.5: Measured values of the x- and y-components of the beam quality factor M^2 for the realized Pr^{3+}:YLF lasers pumped with $P_{\mathrm{OPSL}} = 300\,\mathrm{mW}$

By reducing the excited crystal volume, gain of higher transversal modes can be suppressed efficiently. Thus, even at increased pump power levels, only the fundamental transversal mode is expected for sufficiently short laser crystals. The lasers realized in the framework of this thesis operate without wavelength-selective components inside the laser cavity. However, due to the narrow linewidth of emission, only a few cavity modes contribute to the laser output. In case of the Pr^{3+}:YLF laser crystal in the nearly concentric cavity, the cavity mode distance due to the etalon introduced by the laser crystal is approximately $\delta\nu = \frac{c}{2l} = 43\,\mathrm{GHz}$. The spectral linewidth of the fluorescence transition at 639.5 nm is $\Delta\lambda = 0.85\,\mathrm{nm}$, which corresponds to a frequency bandwidth of approximately 623 GHz. This enables lasing of approximately 14 cavity modes in the absence of losses.

4.4.2 Second Harmonic Generation Experiments

This section focuses on the SHG generation obtained by intracavity frequency doubling of laser radiation at $\approx 640\,\mathrm{nm}$.

Preliminary Experiments

The SHG experiments can be divided in two stages. In the first stage, the power characteristics of the laser transition at $\lambda_\omega \approx 640\,\mathrm{nm}$ for the investigated laser crystals were recorded for different output coupling transmissions of mirror M_3 (cf. Figure 4.10) without a non-linear crystal. Then, cw UV generation at $\lambda_{2\omega} = 320\,\mathrm{nm}$ was obtained through intracavity SHG by birefringent phase matching. The nonlinear LBO crystals were mounted in the M_2-M_3 arm of the cavity in the second beam waist. In these experiments mirror

M_3 was HR ($T < 0.02\%$) coated for both λ_ω and $\lambda_{2\omega}$. The UV radiation was coupled out through mirror M_2 in case of the primary experiments and through mirrors M_2 and M_3 in case of the power scaled experiments. The temperature of the LBO crystals was not stabilized.
In the preliminary experiments, a 5.7 mm long Pr^{3+}(0.7 at.%):YLF crystal and a 3 mm Pr^{3+}(1.42 at.%):BYF crystal were used as active laser medium. The YLF crystal had a high-reflectivity (HR, transmission $T < 0.1\%$) coating for λ_ω and a high-transmission (HT, $T > 98\%$) coating for the 480 nm pumping wavelength (λ_{OPSL}) on the input side (M_1); the opposite crystal's surface was antireflection coated for λ_ω. In these experiments, the pump radiation was directly focused into the laser crystal without the input coupling mirror M_1 displayed in Figure 4.10. The laser experiments with the uncoated BYF crystal were performed in the cavity geometry shown in Figure 4.10.
At an OPSL-pump power of 217 mW, the maximum output power of 72.4 mW at λ_ω was measured for $T_{\mathrm{OC}} = 2.0\%$ in case of the Pr^{3+}:YLF crystal. The Findlay-Clay analysis resulted in round-trip residual losses of about 1.7%, while the coefficient K_{C} was $\approx 0.50\,\mathrm{W}^{-1}$. The corresponding values for the Pr^{3+}:BYF laser crystal were 51.0 mW at an absorbed pump power of 207 mW for $T_{\mathrm{OC}} = 0.6\%$. The losses were 1.0% and the coefficient K_{C} was evaluated to be $\approx 0.19\,\mathrm{W}^{-1}$.
Figure 4.16(a) shows the UV output power versus the absorbed pump power for the Pr^{3+}:YLF laser. With an LBO crystal of 3 mm thickness the maximum power at $\lambda_{2\omega}$ was 7.8 mW. Utilizing a 5 mm long LBO nonlinear crystal, the UV power was increased to 13.4 mW. The highest cw UV output power of 19 mW was obtained with an 8 mm long LBO crystal. As 216 mW of pump power were absorbed in the laser crystal, the optical-to-optical efficiency with respect to the absorbed power was $\approx 9\%$. Moreover, based on the results at λ_ω, the conversion of the available fundamental power from the visible to the UV, $\eta_{\mathrm{V-UV}}$ (the ratio between the maximum UV power and the red power obtained for $T_{\mathrm{OC}} = 2.0\%$ at the same pumping level) was determined to be 26%.
The UV output power obtained with the Pr^{3+}:BYF laser crystal is shown in Figure 4.16(b). With the 8 mm long LBO crystal, 18.9 mW were achieved at $\lambda_{2\omega} \approx 320$ nm. The overall efficiency with respect to absorbed power was $\approx 9\%$, almost identical with that obtained with the Pr^{3+}:YLF laser, but at an increased $\eta_{\mathrm{V-UV}}$ of 36%. Cw UV radiation of 7.3 mW and 13.9 mW was obtained with the 3 and 5 mm thick LBO crystal, respectively. The operation temperature was ≈ 23°C. The simulations were performed using Equation 4.26. To obtain reasonable results, the internal losses were variied to simulate the frequency conversion process in the non-linear LBO crystals.

Power scaling

Power scaled SHG experiments were performed with the 3.45 mm Pr^{3+}(0.65at.%):YLF and the 3.00 mm Pr^{3+}(0.45at.%):LLF single crystals already introduced in Section 4.4.1. They were mounted in the setup displayed in Figure 4.10, too. The UV radiation was extracted through mirrors M_2 and M_3. The output power at λ_ω was about 597 mW with $T_{\mathrm{OC}} = 3.6\%$ at an absorbed pump power of 1.4 W in case of Pr^{3+}:YLF. Internal losses and the small-signal gain coefficient were determined by Findlay-Clay analysis to be 1.7% and $0.55\,\mathrm{W}^{-1}$, respectively. For Pr^{3+}:LLF, these values were 1.9% and $0.58\,\mathrm{W}^{-1}$. The

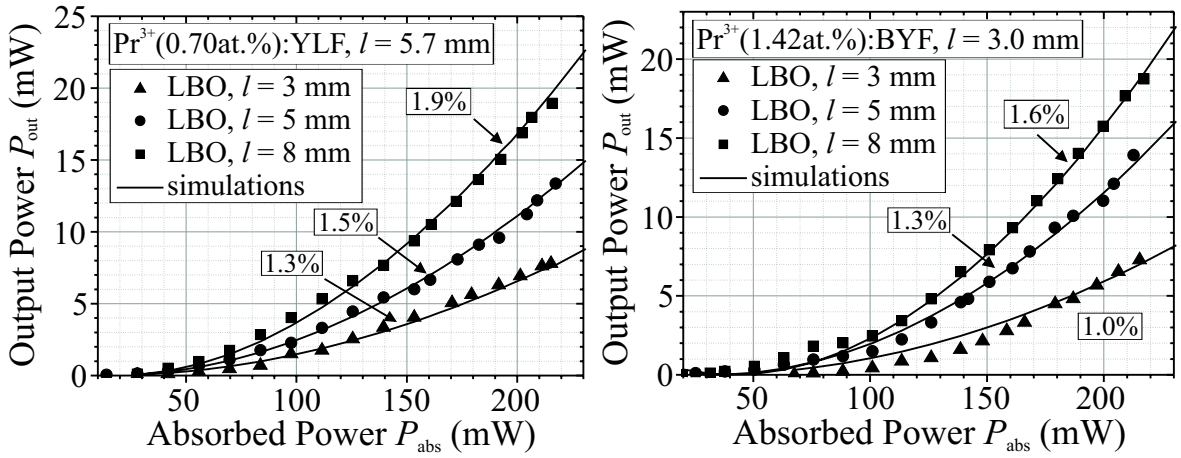

(a) (b)

Figure 4.16: Power characteristics of intracavity SHG of MOPS-pumped (a) Pr^{3+}:YLF and (b) Pr^{3+}:BYF lasers operating at transition ${}^3P_0 \rightarrow {}^3F_2$, the included numbers resemble the internal loss values used in the simulations

maximum output power at λ_ω was obtained with an output coupler transmission of 3.6%. At an absorbed pump power of 1 W, 483 mW were extracted from the Pr^{3+}:LLF crystal. Using an 8 mm long LBO crystal, up to 364 mW and 261 mW of cw UV radiation could be extracted from the Pr^{3+}:YLF and Pr^{3+}:LLF laser cavity, respectively. Regarding the maximum extracted power at the fundamental wave at λ_ω, a conversion efficiency of 61% (Pr^{3+}:YLF) and 54% (Pr^{3+}:LLF) was obtained. The overall optical-to-optical efficiency for the UV output was 22% and 16% for Pr^{3+}:YLF and Pr^{3+}:LLF, respectively. Neglecting thermal effects in the laser crystal under pumping conditions, the SHG output power was simulated using the model developed by Agnesi et al. [Agn02] (see Eqn. 4.26).

The beam quality factor M^2 of the generated UV-radiation was determined for a pump power level of 300 mW, too. Measurements of the UV radiation optimized for output power resulted in values of $M_x^2 = 1.4$ and $M_y^2 = 6.2$ as well as $M_x^2 = 1.8$ and $M_y^2 = 9.9$ for the 3 mm and for the 8 mm LBO crystals, respectively. The reduced beam quality can be explained by the influence of the beam propagation inside the nonlinear medium. Due to the beam walk-off occurring at CPM, the generated beam at $\lambda_{2\omega}$ is composed of multiple Gaussian profiles arranged in the direction corresponding to the Poynting vector component perpendicular to the beam propagation axis. In addition, differences in position and beam waist diameters of the tangential and saggital component of the cavity mode result in an astigmatic beam profile of the SHG radiation.

Power fluctuations of the UV output were measured using a fast silicon diode. Due to the spectral behaviour at the fundamental wavelength, mode coupling by SFG influences the power stability. Chaotic amplitude fluctuations featuring modulation depths of 34%

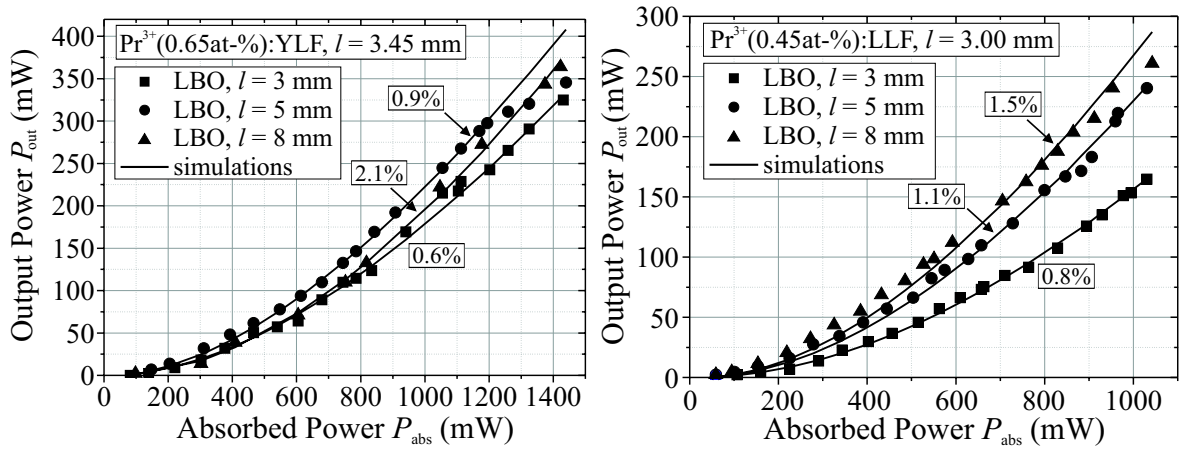

(a) (b)

Figure 4.17: Power characteristics of intracavity SHG of OPSL-pumped (a) Pr^{3+}:YLF and (b) Pr^{3+}:LLF operated at transition $^3P_0 \rightarrow {}^3F_2$, the numbers resemble the values of internal losses estimated for the simulations

at several MHz were recorded, similar to the well-known "green problem" [Bae86].

4.4.3 Active Q-Switching Experiments

First results of pulsed Pr^{3+}-lasers were reported in 1995 and 1996 [Rua95, Ton96]. The Pr^{3+}:YLF lasers were emitting in the visible spectral range and pulsing was obtained by Kerr-Lens mode locking. Ruan et al. demonstrated modelocking of the 607 nm and 639.5 nm visible laser transition with pulsewidths of 8-10 ps as well as parasitic Q-switching with pulsewidths of about 20 µs. However, no experimental results regarding active Q-switching of Pr^{3+}:YLF and Pr^{3+}:LLF lasers have been reported so far, to the best of the authors knowledge. Thus, the data presented in this section represents results of the first investigations of Q-switched Pr^{3+}-based laser systems.

Q-switching experiments were performed in a single folded cavity shown in Figure 4.13. The pump source for these experiments was the miniG. It provided radiation at a wavelength of ≈ 479.5 nm with up to 4.5 W power with moderate beam quality factors of $M_x^2 = 1.9$ and $M_y^2 = 4.5$. Due to the high pump powers available, the laser crystals were mounted in a water-cooled holder to remove the generated heat during the laser experiments. To obtain a more homogeneous heat distribution inside the laser crystals and a small non-radiative decay rate, reduced Pr^{3+}-doping levels and longer crystals were used in the experiments with Pr^{3+}:YLF. Here, the whole pump power available of 4.5 W was focused into the samples. Even so, the obtained beam quality starts to decrease above a pumping level of around 2 W. Due to a higher Pr^{3+}-concentration in the available LLF

crystals and an inappropriate sample geometry for water cooling, the pump power level was reduced to 3.5 W.
Q-switching experiments were performed with three different crystals: a 11.5 mm long Pr^{3+}(0.3 at.%):YLF, a Pr^{3+}(0.4 at.%):YLF ($d = 8.0$ mm), and a Pr^{3+}(0.45 at.%):LLF crystal with a thickness of 5.0 mm. Prior to pulse experiments, the power characteristics in cw mode were recorded. The results are listed in Table 4.6. At an absorbed power of 3.5 W and 3.4 W, laser radiation at 639.5 nm with output powers of 1.5 W and 1.4 W were obtained from the 0.3 at.% and 0.4 at.% Pr^{3+}-doped YLF-crystals, respectively. The corresponding slope efficiencies η_S for these crystals were 0.50 and 0.47 for an output coupling transmission of $T_{OC} = 5.68\%$. The Pr^{3+}:LLF laser emitting up to 0.75 W at an absorbed pump power of 2.4 W and a slope efficiency of $\eta_S = 0.43$ was recorded for $T_{OC} = 3.8\%$.

	Pr^{3+}(0.3 at.%):YLF	Pr^{3+}(0.4 at.%):YLF	Pr^{3+}(0.45 at.%):LLF
material parameters and cw laser parameters			
l (mm)	11.5	8.0	5.0
τ_{eff} (µs)	47	44	38
P_{abs} (W)	3.5	3.4	2.4
$P_{max,cw}$ (W)	1.5	1.4	0.75
η_S	0.50	0.47	0.43
T_{OC} (%)	5.68	5.68	3.8
pulse parameters at $f_Q = 200$ Hz, $T_{OC} = 5.68\%$			
Δt (ns)	124	108	138
t_B (µs)	1.88	1.74	2.01
P_P (W)	530	560	252
E_P (µJ)	62	59	35
η_P	0.88	0.96	

Table 4.6: Material properties and laser parameters in cw and Q-switch mode

Table 4.6 gives the experimental pulse parameters for the three samples. At an absorbed pump power of about 3.4 W and a repetition rate of 200 Hz, pulse energies E_P of 62 µJ and pulse peak powers P_P of 530 W were obtained from the Pr^{3+}(0.3 at.%):YLF sample. The pulsewidth Δt was determined to be 124 ns and the pulse efficiency η_P (see Eqn. 4.37) was about 0.88. Figure 4.18 shows the typical pulse shape obtained in the Q-switching experiments. The results of the YLF sample with the higher doping level of 0.4 at.% were 59 µJ pulse energy and 560 W of peak power at a pulse width of 108 ns. Here, η_P was about 0.96 and the pulse buildup time t_B was about 1.8 µs. Due to the reduced pump power in case of Pr^{3+}(0.45 at%):LLF, the pulses featured an energy of 35 µJ, a pulse power of 252 W and a pulsewidth of 138 ns. In the Pr^{3+}:LLF experiments, t_B was about 2.0 µs. These results were obtained for $T_{OC} = 5.68\%$. In case of higher output coupler transmissions, parasitic laser oscillation at a wavelength of 721 nm or 607 nm due to the transmission

characteristics of the mirrors was initiated.

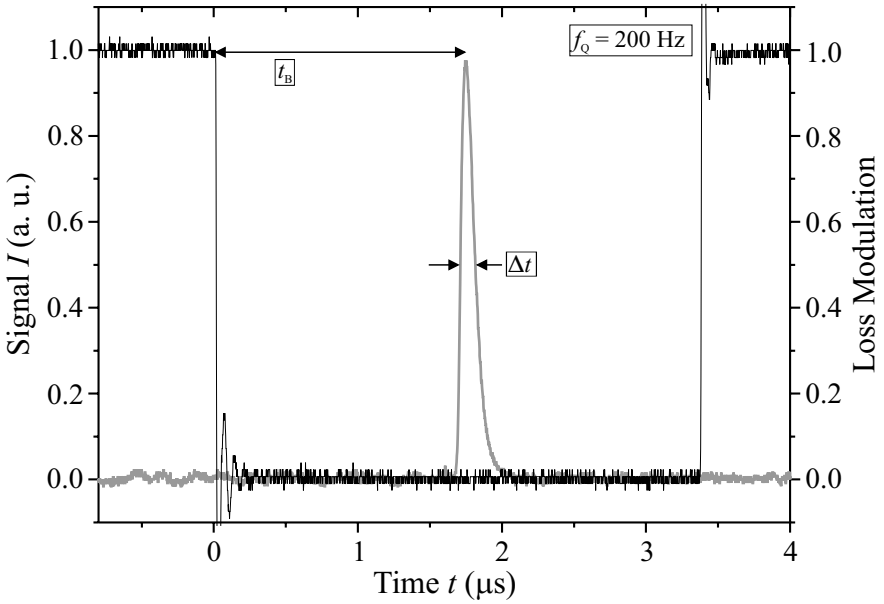

Figure 4.18: Typical pulse shape of the Q-switched laser obtained with Pr^{3+}(0.4 at.%):YLF at a repetition rate $f_Q = 200$ Hz

Using Equations 4.33, 4.34, and 4.35, the pulse parameters of the Pr^{3+}(0.3 at.%):YLF crystal have been estimated to be $P_P = 4$ kW, $E_P = 86$ µJ and $\Delta t = 21$ ns. The values of the peak pulse power and the pulse duration differ significantly from the experimental results. A possible explanation might be the reduction of the radiative lifetime due to CRPs leading to an effectively smaller amount of storable energy. Furthermore, thermal stress can result in increased value of the internal losses.

4.5 Results of Laser Diode pumped Pr-lasers

GaN-LD pumped Pr^{3+}-lasers were reported by our group in 2004 for the first time [Ric04b]. Due to the low pump power of 25 mW, laser oscillation could be realized at the transition ${}^3P_0 \rightarrow {}^3F_2$ only. Using a highly reflective cavity, about 1.8 mW of output power could be demonstrated. Due to progress in GaN-LD fabrication, higher pump powers became available and higher output powers on this transition could be achieved [Has07a, Ric07]. Additionally, demonstration of a diode laser pumped Pr^{3+}:KYF laser was reported recently [Cam07]. Application of laser diodes as pump source is a necessary step for realizing compact laser systems.

4.5.1 Fundamental Wave Experiments

GaN-LD-pumped laser experiments were performed in the setup shown schematically in Figure 4.7. By applying two LDs, pump powers of up to 1 W were available for the laser experiments. The pumping wavelength was around 444 nm, matching the GSA peak to the ${}^3P_2$ energy level for the systems Pr^{3+}:YLF, Pr^{3+}:LLF and Pr^{3+}:BYF. In case of Pr^{3+}:KYF, this wavelength corresponds to the minimum of absorption between the peaks at 442.1 nm and 446.2 nm. Both pump beams were focused into the laser medium individually in order to achieve reasonable overlap efficiencies. The YLF and LLF crystals were oriented for $\vec{E} \| \vec{c}$ polarization exploiting the large peak absorption cross-section of about $0.9 \times 10^{-19}\,\mathrm{cm}^2$, while the Pr^{3+}:BYF crystals were matched for $\vec{E} \| \vec{b}$ polarization. Due to the strong polarization dependence of the absorption cross-sections, polarization coupling of the LD beams was not an option for the performed experiments.
The shorter pump wavelength of 444 nm in contrast to 479 nm results in a larger quantum defect η_Q and thus to reduced slope efficiencies η_S. Table 4.7 gives the corresponding values for the realized laser transitions for each crystal system. The reader should keep in mind that along with an increased η_Q the heat generation in these materials is increased. Table 4.7 provides information about the overlap efficiencies η_O and the maximum observable slope efficiencies $\eta_\mathrm{S,max}$ due to geometrical limitations. The total overlap efficiency was estimated to be 10% higher thean the overlap efficiency realized with LD_2 only.

The resulting power characteristics of the laser transition ${}^3P_0 \rightarrow {}^3F_2$ are displayed in Figure 4.19 (a) for a selection of the investigated laser crystals. The highest output power of 208 mW was achieved with a 9.15 mm long Pr^{3+}(0.45 at.%):LLF crystal, while the highest slope efficiency shown in this figure was 0.41 for the Pr^{3+}(0.65 at.%):YLF crystal. The YLF and LLF crystals show comparable results, while the output powers obtained from the Pr^{3+}:BYF and Pr^{3+}:KYF laser crystals were significantly lower. Table 4.8 gives a detailed overview of the key parameters for each crystal under investigation. The round-trip losses were determined by Findlay-Clay analysis and the method of Caird. They are in the range of 0.5% to 1.8%. It should be noted that the loss determination is not very accurate in case of the Pr^{3+}:BYF samples because only two different output coupling

Laser transition	λ_L (nm)	η_Q	η_O	$\eta_{S,max}$
YLF, $l = 3.00\,\mathrm{mm}$				
$^3P_1 \rightarrow {}^3H_4$	522.6	0.85	0.78	0.66
$^3P_0 \rightarrow {}^3H_6$	607.2	0.73	0.78	0.57
$^3P_0 \rightarrow {}^3F_2$	639.5	0.69	0.78	0.54
$^3P_0 \rightarrow {}^3F_4$	720.8	0.62	0.78	0.48
LLF, $l = 4.45\,\mathrm{mm}$				
$^3P_1 \rightarrow {}^3H_4$	523.9	0.85	0.68	0.58
$^3P_0 \rightarrow {}^3H_6$	607.0	0.73	0.68	0.50
$^3P_0 \rightarrow {}^3F_2$	640.1	0.69	0.68	0.46
$^3P_0 \rightarrow {}^3F_4$	721.4	0.62	0.68	0.42
BYF, $l = 3.00\,\mathrm{mm}$				
$^3P_0 \rightarrow {}^3H_6$	607.6	0.73	0.78	0.57
$^3P_0 \rightarrow {}^3F_2$	642.7	0.69	0.78	0.54
$^3P_0 \rightarrow {}^3F_4$	719.7	0.62	0.78	0.48
KYF, $l = 12.10\,\mathrm{mm}$				
$^3P_0 \rightarrow {}^3F_2$	644.9	0.69	0.42	0.29

Table 4.7: Overview of the general parameters of the realized laser transitions under GaN-LD-pumping

mirrors resulted in laser oscillation.
In general, the losses obtained by the method of Caird are lower than by Findlay-Clay analysis. Due to slope efficiency limitations occurring at a certain level of output coupling transmission (see Table 4.9), the obtained values from the Caird plot are less accurate. The marginal differences of the slope efficiency at a certain output coupling transmission indicates very small internal losses.

The laser performance of the Pr^{3+}:BYF crystals is poor because of the high doping concentration, which enhances the nonradiative decay rate of the upper laser level. An improvement in efficiency is expected for lower Pr^{3+} concentrations. The results obtained with Pr^{3+}:KYF are quite reasonable taking into account the reduced peak cross-sections of absorption and emission. The results obtained by Camy et *al.*[Cam07] are comparable to those presented herein.

4.5.2 Second Harmonic Generation Experiments

First intracavity SHG experiments of the 640 nm laser transition were performed with the 9.15 mm thick Pr^{3+}(0.45 at.%):LLF crystal using an 8 mm long LBO crystal in the setup shown schematically in Figure 4.12. 42 mW of UV power were obtained resulting in a conversion efficiency η_{V-UV} of 20% and an optical-to-optical efficiency of 6% taking

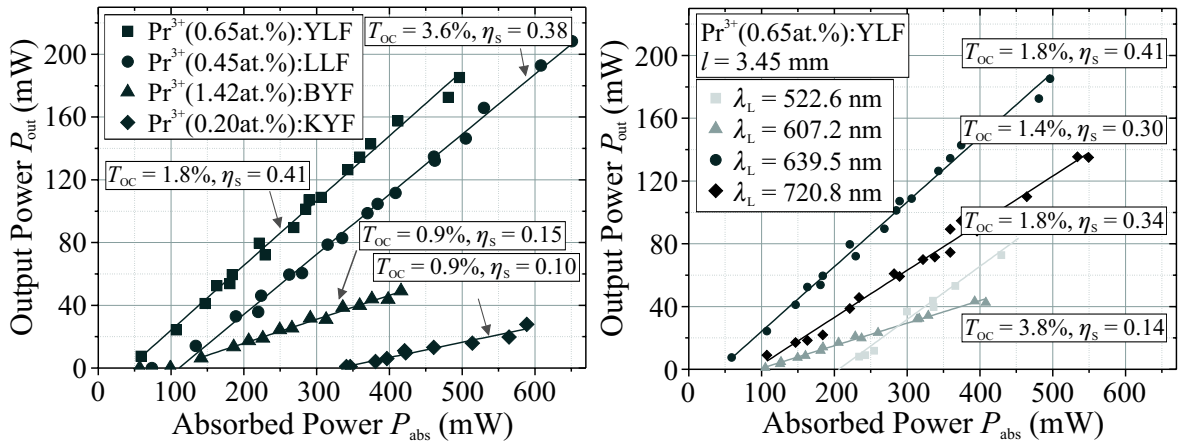

(a) (b)

Figure 4.19: Power characteristics of GaN-LD-pumped (a) different Pr^{3+}-doped fluorides operated at transition ${}^3P_0 \rightarrow {}^3F_2$ and (b) Pr^{3+}:YLF operated at different transitions

c_{Pr} (at.%)	d (mm)	T_{OC} (%)	P_{thr} (mW)	η_S	P_{abs} (mW)	P_{max} (mW)	$\gamma_{i,FC}$	$\gamma_{i,CA}$
YLF								
0.23	17.10	5.7	227	0.38	570	135	0.018	0.008
0.65	3.45	1.8	42	0.41	496	185	0.005	0.003
LLF								
0.15	7.70	3.6	94	0.41	366	107	0.018	0.006
0.20	4.05	3.6	57	0.46	237	86	0.015	0.005
0.45	3.00	3.6	75	0.43	408	144	0.018	0.005
0.45	4.45	1.8	55	0.45	480	184	0.011	0.005
0.45	9.15	3.6	111	0.38	651	208	0.055	0.009
BYF								
1.42	2.20	0.9	97	0.15	416	49	0.001	0.006
1.42	4.70	0.9	176	0.08	753	45	0.006	0.002
KYF								
0.20	12.10	1.8	490	0.16	618	22	0.018	0.007

Table 4.8: Overview of the laser parameters of the investigated samples in case of the laser transition ${}^3P_0 \rightarrow {}^3F_2$

T_{OC} (%)	η_S	P_{thr} (mW)
0.47	0.24	31
0.90	0.32	33
1.83	0.41	50
3.56	0.43	75
5.68	0.42	99

Table 4.9: Laser parameters obtained for the 3 mm Pr^{3+}(0.45 at.%):LLF crystal for different output coupling transmissions. The investigated laser transition was $^3P_0 \rightarrow {}^3F_2$

into account the incident pump power of 657 mW. Figure 4.20 shows the measured power characteristics and the corresponding simulation results.

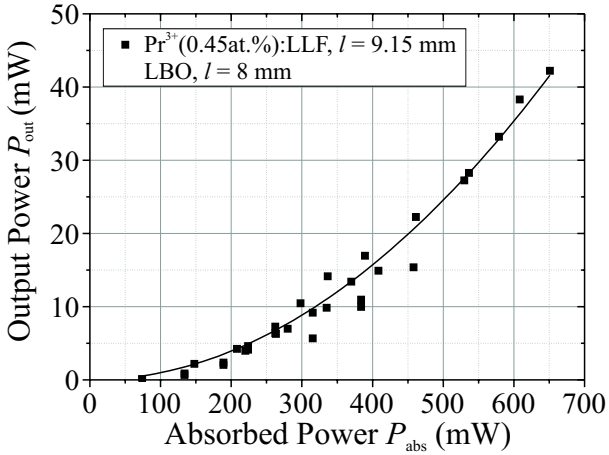

Figure 4.20: Power characteristics of intracavity frequency doubled laser radiation at 640.2 nm of a GaN-LD-pumped Pr^{3+}:LLF crystal

4.6 Summary

OPSL- and GaN-LD-pumped Pr^{3+}-laser experiments were performed in continuous wave operation. Different laser transitions in the visible spectral range were investigated focusing on their power characteristics. The slope efficiencies of 0.46 and 0.56 were obtained from longitudinally pumped Pr^{3+}-doped YLF and LLF crystals under OPSL-pumping. These are the highest efficiencies reported so far. The quantum limit could not be reached because of an overlap efficiency of ≈ 0.75 and the influence of CRPs. Output powers of 600 mW were obtained in the green and red spectral region at an absorbed pump power of 1.4 W, while in the orange spectral region about 350 mW were measured at a reduced efficiency. Spectral investigations revealed that the radiation of this laser transition ${}^3P_0 \rightarrow {}^3H_6$ is partially reabsorbed by the GSA transition ${}^3H_4 \rightarrow {}^1D_2$. The corresponding emission spectra show an increased ${}^1D_2$ fluorescence during laser operation. The beam quality factor of the realized lasers were determined to be below $M^2 = 1.3$.
Intracavity SHG of the visible laser radiation at ≈ 640 nm using LBO nonlinear crystals resulted in demonstration of continuous wave radiation generation at 320 nm in the UV for the first time. Under OPSL-pumping, up to 360 mW of UV radiation could be achieved with a conversion efficiency of 0.61 and an overall optical-to-optical efficiency of 0.22. Due to the Poynting vector beam walk-off, the beam quality factor decreased to $M_x^2 \times M_y^2 = 1.8 \times 9.9$.
Pulsed laser operation at ≈ 640 nm via active Q-switching using an AOM resulted in pulse peak powers of 560 W with a pulse energy of ≈ 60 µJ and a pulsewidth of 108 ns. These results were obtained at a repetition rate of 200 Hz and at an OPSL pump power of 4.5 W. They represent the first reported data of an actively Q-switched Pr^{3+}-laser operated on a visible laser transition. Although the laser crystals were water cooled, stress induced by the high pump powers resulted in thermal lensing affecting the transversal beam profile at pump powers above 2.0 W.
GaN-LD-pumping of Pr^{3+}-doped laser crystals resulted in efficient lasing, too. In comparison to the OPSL-pumped systems, GaN-LD-pumped Pr^{3+}-lasers feature a slightly reduced efficiency due to the reduced beam quality factor of the pump beam. The overlap efficiency was determined to be in the same range as for OPSL-pumping. Using two LDs as pump source, up to 208 mW at 640 nm, could be demonstrated so far. In this setup, slope efficiencies of 0.46 could be demonstrated. In case of Pr^{3+}:YLF, about 70 mW in the green, 40 mW in the orange, 185 mW in the red, and 135 mW in the near infrared spectral region could be realized. The results obtained with the laser host materials LLF, BYF, and KYF are promising, too. Regarding intracavity SHG of the 640 nm radiation, more than 42 mW could be obtained from a GaN-LD-pumped system so far.

5 Summary and Outlook

In the framework of this thesis, the highest slope efficiencies of directly pumped Pr^{3+}-lasers under OPSL- and GaN-LD-pumping as well as the generation of continuous wave UV radiation at 320 nm has been demonstrated for the first time. Furthermore, different rare earth ion sites in the laser host materials $LiYF_4$ and $LiLuF_4$ have been investigated in case of Pr^{3+}-doping.

The crystal growth of Pr^{3+}-doped fluoride single crystals of $LiYF_4$, $LiLuF_4$, and KY_3F_{10} resulted in an optical quality sufficient for laser oscillation. The carbon-based growth setup was not optimized and thus the crystals suffered from inclusions, cracking and polycrystalinity to some extent.
Improvements in crystal quality should be obtained by reducing the carbon contaminations, introducing an additional heating process during the evacuation process and applying a reduced rotation rate. Furthermore, slight modifications of the axial temperature gradient should reduce the effect of constitutional supercooling.

For evaluation of the incorporation behaviour of praseodymium ions in the fluoride crystalline materials, investigations using optical spectroscopy were performed. Time resolved luminescence measurements revealed effective cross-relaxation processes with nonradiative decay rates in the range of $100 - 40000\,s^{-1}$ with a quadratic concentration dependence. The coupling mechanism of the interaction between Pr^{3+}-ions at room temperature results from a mixture of (super-)exchange and dipole-dipole interaction. Typical distances of interaction are about 9 Å in case of (super-)exchange and about 70 Å in case of dipole-dipole induced interactions. A more detailed low temperature study on the most promising crystal structures for efficient laser action, $LiYF_4$ and $LiLuF_4$, revealed more than 5 ion classes which correspond to different sites in the host lattice. By considering absorption, emission, excitation, and decay characteristics, 3 of them could be identified. Besides the Pr^{3+}-ions on regular Y^{3+}/Lu^{3+}-sites, another ion class which is not influenced by excitation energy transfer has been found. However, this class most likely corresponds to an irregular lattice site. An increase in the ion concentration revealed a tendency to cluster even at Pr^{3+}-concentrations of 0.22 at.%. This is not surprising considering the ionic radii of the host ion and the dopant ion. By incorporation of large dopant ions, local stress is induced in the host matrix. This can be compensated by voids, for example. Another type of Pr^{3+}-ions found in the spectroscopic investigations performs efficient energy transfer even at low temperatures. These ions are located at irregular sites, too. They contribute quite strongly to the population of the $^1D_2$ energy level.
The nature of the irregular lattice sites could not be determined in the context of this work. Investigations regarding colour centre formation in these fluoride crystals by elec-

tron beam irradiation might result in relevant information.
Furthermore, the strong emission of the transition ${}^3P_0 \rightarrow {}^3H_6$ could be confirmed during the low temperature measurements in the Pr^{3+}:$LiYF_4$ and Pr^{3+}:$LiLuF_4$. The mechanism responsible for the high emission intensity is still not understood in detail and needs further investigations.
To reduce the influence of nonradiative decay by cross-relaxation processes, crystalline host materials with suitable lattice sites are necessary. In such materials, lattice distortions and clustering would most likely not occur with incorporated Pr^{3+}-ions. For example, Pr^{3+}-ions incorporated in the host material $LiGdF_4$, which is isostructural to $LiYF_4$, would generate lower stress levels than in $LiYF_4$ or $LiLuF_4$. However, first investigations of this system resulted in nonexponential decay characteristics of the upper laser level, too. This is a clear indication for cross-relaxation processes. Because of the suitable ionic radii of Pr^{3+} and La^{3+}, clustering effects in Pr^{3+}-doped LaF_3 single crystals should be reduced. Alternatively, oxides with low phonon energies like for example perovskite-type or sesquioxide-type crystals look promising as well.

OPSL- and GaN-LD-pumped Pr^{3+}-laser experiments were performed in continuous wave operation. Different laser transitions in the visible spectral range were investigated focusing on their power characteristics. Slope efficiencies of 0.46 and 0.56 were obtained from longitudinally pumped Pr^{3+}-doped $LiYF_4$ and $LiLuF_4$ crystals under OPSL-pumping. These are the highest efficiencies reported so far. The quantum limit could not be reached due to the overlap efficiency of ≈ 0.75 and the influence of cross-relaxation processes. Output powers of 600 mW were obtained in the green and red spectral region at an absorbed pump power of 1.4 W, while in the orange spectral range about 350 mW were measured at a reduced efficiency. Spectral investigations revealed that the radiation of this laser transition (${}^3P_0 \rightarrow {}^3H_6$) is partially reabsorbed by the ground state absorption transition ${}^3H_4 \rightarrow {}^1D_2$. The corresponding emission spectra show an increased ${}^1D_2$ fluorescence during laser operation. The beam quality factor of the realized lasers were determined to be below $M^2 = 1.3$.
Intracavity second harmonic generation of the visible laser radiation at ≈ 640 nm using LBO nonlinear crystals resulted in demonstration of continuous wave radiation generation at 320 nm in the UV for the first time. Under OPSL-pumping, up to 360 mW of UV radiation could be achieved with a conversion efficiency of 0.61 and an overall optical-to-optical efficiency of 0.22. Due to the Poynting vector beam walk-off, the beam quality factor decreased to $M_x^2 \times M_y^2 = 1.8 \times 9.9$.
Pulsed laser operation at ≈ 640 nm via active Q-switching using an acoustooptical modulator resulted in pulse peak powers of 560 W with a pulse energy of ≈ 60 µJ and a pulsewidth of 108 ns. These results were obtained at a repetition rate of 200 Hz and at an OPSL pump power of 4.5 W. They represent the first reported data of an actively Q-switched Pr^{3+}-laser operated on a visible laser transition. Although the laser crystals were water cooled, pump powers above 2.0 W resulted in thermal lensing.
In comparison to the OPSL-pumped systems, GaN-LD-pumped Pr^{3+}-lasers feature a slightly reduced efficiency due to the reduced beam quality factor of the pump beam. The overlap efficiency was estimated to be in the same range as for OPSL-pumping. Us-

ing two LDs as pump source, up to 208 mW at 640 nm could be demonstrated with slope efficiencies of 0.46. In case of Pr^{3+}:$LiYF_4$, about 70 mW in the green, 40 mW in the orange, 185 mW in the red, and 135 mW in the near IR spectral region could be realized. The results obtained with the laser host materials $LiLuF_4$, BaY_2F_8, and KY_3F_{10} are promising, too. Regarding intracavity second harmonic generation of the 640 nm radiation, more than 42 mW could be obtained from a GaN-LD-pumped system so far. Application of GaN-LDs as pump source are beneficial for realizing compact and efficient Pr^{3+}-lasers for several applications such as projection displays.

Improvements in laser performance can be obtained by modifying the pump geometry to achieve a higher geometrical overlap efficiency. To realize compact LD-pumped Pr^{3+}-lasers, gradient index optics might be a suitable approach.

Bibliography

[Abd87] R. Y. Abdulsabirov, M. A. Dubinski, B. N. Kazakov, N. I. Silkin and S. I. Yagudin. *New fluoride laser matrix*. Sovjet Physics - Crystallography **34** (1987).

[Ada85] J. L. Adam, W. A. Sibley and D. R. Gabbe. *Optical absorption and emission of $LiYF_4$:Pr^{3+}*. Journal of Luminescence **33**, 391 (1985).

[Agn02] A. Agnesi, A. Guandalini and G. Reali. *Efficient 671-nm pump source by intracavity doubling of a diode-pumped Nd:YVO_4 laser*. J. Opt. Soc. Am. B **19**, 1078 (2002).

[Bae86] T. Baer. *Large-amplitude fluctuations due to longitudinal mode coupling in diode-pumped intracavity-doubled Nd:YAG lasers*. Journal of the Optical Society of America B **3**, 1175 (1986).

[Bar86] R. B. Barthem, R. Buisson, J. C. Vial and H. Harmand. *Optical properties of Nd^{3+} pairs in $LiYF_4$ - Existence of a short range interaction*. Journal of Luminescence **34** (1986).

[Ben04] A. Bensalah, Y. Guyot, M. Ito, A. Brenier, H. Sato, T. Fukuda and G. Boulon. *Growth of Yb^{3+}-doped $YLiF_4$ laser crystal by the Czochralski method. Attempt of Yb^{3+} energy level assignment and estimation of the laser potentiality*. Optical Materials **26** (2004).

[Blu80] A. Blumen. *On the direct energy tranfer via exchange to randomly distributed acceptors*. Journal of Chemical Physics **72** (4), 2632 (1980).

[Blu81] A. Blumen and J. Manz. *On the anisotropic energy transfer to random acceptors*. Journal of Chemical Physics **74**, 6926 (1981).

[Bol01] A. Bolz. *Energietransfer in Yb-dotierten Sesquioxiden* (Universität Hamburg, 2001). Diplomarbeit.

[Boy95] R. W. Boyd. *Nonlinear Optics* (Academic Press, 1995).

[Bra91] N. B. Brandt, L. I. Devyatkova and E. V. Ralko. Mosc. Univ. Phys. Bull. **46** (1991).

[Bra07] C. Braun. *Spektroskopische Charakterisierung und erste Lasertätigkeit von Pr^{3+}:KY_3F_{10}* (Universität Hamburg, 2007). Diplomarbeit.

[Bur62] G. Burns. *Shielding and Crystal Fields at Rare-Earth Ions*. Physical Review **128** (5), 2121 (1962).

[Bur72] A. I. Burshtein. *A hopping mechanism of energy transfer*. Sovjet Physics JETP **35** (1972).

[Bur78] A. I. Burshtein. *Quasiresonance transfer. Part II*. Zh. Avtometriya **5**, 65 (1978).

[Bur85] A. I. Burshtein. *Energy Transfer Kinetics in Disordered Systems*. Journal of Luminescence **34**, 167 (1985).

[Bur01] R. Burkhalter, I. Dohnke and J. Hullinger. *Growing of Bulk Crystals and Structuring Waveguides of Fluoride Materials for Laser Applications*. Progress in Crystal Growth and Characterization of Materials **42** (2001).

[Cai88] J. A. Caird, S. A. Payne, P. R. Staver, A. J. Ramponi, L. L. Chase and W. F. Krupke. *Quantum electronic properties of the $Na_2Ga_2Li_3F_{12}$:Cr^{3+} laser*. IEEE Journal of Quantum Electronics **24** (6) (1988).

[Cam07] P. Camy, J. L. Doualan, R. Moncorgé, J. Bengoechea and U. Weichmann. *Diode-pumped Pr^{3+}:KY_3F_10 red laser*. Optics Letters **32**, 1462 (2007).

[Cha93] B. T. H. Chai, J. Lefaucheur, A.-T. Pham, G. B. Loutts and J. F. Nicholls. *Growth of high-quality single crystals of KYF4 by TSSG method*. Proceedings of SPIE **1863** (1993).

[Chi96] S. Chichibu, T. Azuhata, T. Sota and S. Nakamura. *Spontaneous emission of localized excitons in InGaN single and multi quantum well structures*. Applied Physics Letters **69**, 4188 (1996).

[Chi04] J. L. A. Chilla, S. D. Butterworth, A. Zeitschel, J. P. Charles, A. L. Caprara, M. K. Reed and L. Spinelli. *High-power optically pumped semiconductor lasers*. Proceedings of SPIE **5332**, 143 (2004).

[Cor07] F. Cornacchia, A. Richter, E. Heumann, G. Huber, D. Parisi and M. Tonelli. *Visible laser emission of solid-state pumped $LiLuF_4$ Pr^{3+}*. Optics Express **15**, 992 (2007).

[Cou07] L. C. Courrol, I. M. Ranieri, S. L. Baldochi, R. E. Samad, A. Z. de Freitas, L. Gomes and N. D. V. Jr. *Study of color centers produced in thulium doped YLF crystals irradiated by electron beam and femtosecond laser pulses*. Optics Communications **270**, 340 (2007).

[Dan76] H. G. Danielmeyer. *Lasers: A series of advances*, Volume 4, chapter Progress in Nd:YAG lasers, 1 – 71 (Marcel Dekker Inc., New York, 1976).

[Deg89] J. J. Degnan. *Theory of the Optimally Coupled Q-Switched Laser*. IEEE Journal of Quantum Electronics **25**, 214 (1989).

[Der03] P. J. Deren, A. Bernarkiewicz, R. Maihou and W. Strek. *On spectroscopic properties of the $KYb(WO_4)_2$:Pr^{3+} crystal*. Molecular Physics **101** (7), 951 (2003).

[DeS00] L. G. DeShazer, S. C. . Rand and B. A. Wechsler. *Laser crystals, Handbook of Laser Science and Technology Vol. V: Optical Materials* (CRC Press, 2000).

[Dex53] D. L. Dexter. *A Theory of Sensitized Luminescence in Solids*. Journal of Chemical Physics **21** (5), 836 (1953).

[Dok81] A. B. Doktorov, R. F. Khairutdinov and K. I. Zamaraev. *Analysis of kinetic models for the tunnel electron transfer reactions. Reaction kinetics for various radial and angular dependences of the tunneling probability*. Chemical Physics **61**, 351 (1981).

[DT98] L. Diaz-Torres, O. Barbosa-Garcia, J. Hernandez, V. Pinto-Robledo and D. Sumida. *Evidence of energy transfer among Nd ions in Nd:YAG driven by a mixture of exchange and multipolar interactions*. Optical Materials **10**, 319 (1998).

[ECTI] C. compiled by Eddy Current Technology Incorporated. *Electrical Conductivity & Resistivity for Miscellaneous Metals & Alloys*. NDT: Resource Center.

[Ehr79] D. J. Ehrlich, P. F. Moulton and R. M. O. jr. *Ultraviolet solid-state Ce:YLF laser at 325 nm*. Optics Letters **4**, 184 (1979).

[Ein16] A. Einstein. *Strahlungs-Emission und -Absorption nach der Quantentheorie*. Verhandlungen der Deutschen Physikalischen Gesellschaft **13/14**, 318 (1916).

[Erd72] P. Erdös and H. Kang. *Electronic Shielding of Pr^{3+} and Tm^{3+} in crystals*. Physical Review B **6** (9), 3393 (1972).

[Est77] L. Esterowitz, R. Allen, M. Kruer, F. Bartoli, L. S. Goldberg, H. P. Jenssen, A. Linz and V. O. Nicolai. *Blue light emission by a Pr:$LiYF_4$-laser operated at room temperature*. Journal of Applied Physics **48** (2), 650 (1977).

[Est79] L. Esterowitz, F. J. Bartoli and R. E. Allen. *Energy levels and line intensities of Pr^{3+} in $LiYF_4$*. Physical Review B **19** (12) (1979).

[Fee07] D. F. Feezell, R. M. Farrell, M. C. Schmidt, H. Yamada, M. Ishida, S. P. DenBaars, D. A. Cohen and S. Nakamura. *Thin metal intracavity contact and lateral current-distribution scheme for GaN-based vertical-cavity lasers*. Applied Physics Letters **90**, 181128 (2007).

[Fin66] D. Findlay and R. A. Clay. *The measurement of internal losses in 4-level lasers*. Phys. Lett. **20** (3), 277 (1966).

[För48] T. Förster. *Zwischenmolekulare Energiewanderung und Fluoreszenz*. Annalen der Physik **437** (1), 55 (1948).

[För49] T. Förster. *Experimentelle und theoretische Untersuchung des zwischenmolekularen Übergangs von Elektronenanregungsenergie*. Zeitschrift für Naturforschung **4a** (5), 321 (1949).

[Gra93] T. Graf and J. E. Balmer. *High-power Nd:YLF laser end pumped by a diode-laser bar*. Optics Letters **18**, 1317 (1993).

[Gui93] L. H. Guilbert, J. Y. Gesland, A. Bulou and R. Retoux. *Structure and Raman spectroscopy of Czochralski-grown barium yttrium and barium ytterbium fluorides crystals*. Materials Research Bulletin **28** (1993).

[GW96] C. Görller-Walrand and K. Binnemans. *Handbook on the Physics and Chemistry of Rare Earths*, Volume 23 (Elsevier Science B.V., 1996).

[Had99] C. Z. Hadad and S. O. Vasquez. *Energy-transfer processes induced by exchange interactions*. Physical Review B **60**, 8586 (1999).

[Har83] I. R. Harris, H. Safi, N. A. Smith, M. Altunbas, B. Cockayne and J. G. Plant. *The relationship between crystal growth behaviour and constitution in the systems LiF-LuF_3 , LiF-ErF_3 and LiF-YF_3*. Journal of Materials Science **18** (1983).

[Has07a] K. Hashimoto and F. Kannari. *High-power GaN diode-pumped continuous wave Pr^{3+}-doped $LiYF_4$ laser*. Optics Letters **32**, 2493 (2007).

[Has07b] K. Hashimoto and F. Kannari. *Stimulated Emission at an Orange Wavelength from Cryogenically Cooled Pr^{3+}-Doped $LiYF_4$ and $Y_3Al_5O_{12}$*. Japanese Journal of Applied Physics **46**, 589 (2007).

[Heg82] J. Hegarty, D. L. Huber and W. M. Yen. *Fluoresence quenching by cross relaxation in LaF_3:Pr^{3+}*. Phys. Rev. B **25** (9), 5638 (1982).

[Hen89] B. Henderson and G. F. Imbusch. *Optical Spectroscioy of Inorganic Solids* (Clarendon Press, Oxford, 1989).

[Hen01] M. Henke. *Interkonfigurale Übergänge Lanthanid-dotierter Kristalle* (Shaker Verlag, Aachen, 2001). Dissertation.

[Heu99] E. Heumann, C. Czeranowsky and T. Kellner. *An efficient all-solid-state Pr^{3+}:$LiYF_4$ laser in the visible spectral range*. In: *CLEO 1999, Technical Digest* (1999).

[Ino65] M. Inokuti and F. Hirayama. *Influence of energy transfer by the exchange mechanism on donor luminescence*. Journal of Chemical Physics **43** (6), 1978 (1965).

[Jen96] T. Jensen, A. Diening, G. Huber and B. H. T. Chai. *Investigation of diode-pumped 2.8-µm Er:$LiYF_4$ lasers with various doping levels*. Optics Letters **21**, 585 (1996).

[Joh74] L. F. Johnsson and H. J. Guggenheim. *Electronic- and phonon-terminated laser emission from Ho^{3+} in BaY_2F_8*. IEEE Journal of Quantum Electronics **10** (1974).

[Jør77] C. K. Jørgensen and R. Reisfeld. *Lasers and Excited States of Rare Earths* (Springer Verlag, 1977).

[Jud62] B. R. Judd. *Optical absorption intensities of rare-earth-ions*. Physical Review **127**, 750 (1962).

[Kam86] A. A. Kaminskii and S. E. Sarkisov. *Stimulated-emission spectroscopy of Pr^{3+} ions in monoclinic BaY_2F_8 fluoride*. Phys. Status Solidi (a) **97** (1986).

[Kam90] A. A. Kaminskii. *Laser Crystals. Their Physics and Properties* (Springer Verlag, 1990), 2 edition.

[Kam93a] A. A. Kaminskii, H. J. Eichler, B. Liu and P. Meindl. *$LiYF_4$:Pr^{3+} laser at 639.5 nm with 30 J flashlamp pumping and 87 mJ output energy*. Physica Status Solidi (a) **138**, K 45 (1993).

[Kam93b] A. A. Kaminskii, K.-I. Ueda and N. Uehara. *New Laser-Diode-Pumped CW Laser Based on Nd3+-Ion-Doped Tetragonal $LiLuF_4$ Crystal*. Jap. Journal of Applied Physics **32**, L 586 (1993).

[Kam98] A. A. Kaminskii, A. I. Lyashenko, N. P. Isaev, V. N. Karlov, V. L. Pavlovich, S. N. Bagayev, A. V. Butashin and L. E. Li. *Quasi-cw Pr^{3+} : $LiYF_4$ laser with λ = 0.6395 μm and an average output power of 2.3 W*. Quantum Electronics **28**, 187 (1998).

[Kli00] D. Klimm, G. Lacayo and P. Reiche. *Growth of Cr:$LiCaAlF_6$ and Cr:$LiSrAlF_6$ by the Czochralski method*. Journal of Crystal Growth **210** (2000).

[Kob73] H. Kobashi and T. Morita. *Influence of triplet-triplet excitation transfer on the decay function of donor luminescence*. Chemical Physics Letters **20** (1973).

[Koc90] M. E. Koch, A. W. Kueny and W. E. Case. *Photon avalanche upconversion laser at 644 nm*. Applied Physics Letters **56** (12), 1083 (1990).

[Koe95] J. Koetke and G. Huber. *Infrared excited state absorption and stimulated emission cross sections of Er^{3+}-doped crystals*. Applied Physics B **61**, 151 (1995).

[Koe99] W. Koechner. *Solid-state laser engineering* (Springer Verlag, 1999), 4 edition.

[Kog66] H. Kogelnik and T. Li. *Laser Beams and Resonators*. Applied Optics **5**, 1550 (1966).

[Lar99] M. Laroche, A. Braud, S. Girard, J. L. Doualan, R. Moncorge, M. Thuau and L. D. Merkle. *Spectroscopic investigations of the $4f5d$ energy levels of Pr^{3+} in fluoride crystals by excited-state absorption and two-step excitation measurements*. Journal of the Optical Society of America B **16**, 2269 (1999).

[Lar00] M. Laroche, J.-L. Doualan, J. M. S. Girard and R. Moncorge. *Experimental and theoretical investigations of the $4f^2 \rightarrow 4f5d$ ground-state and excited state absorption spectra of Pr^{3+} in $LiYF_4$*. Journal of the Optical Society of America B **17** (7), 1291 (2000).

[Les95] S. D. Lester, F. A. Ponce, M. G. Craford and D. A. Steigerwald. *High dislocation densities in high efficiency GaN-based light-emitting diodes*. Applied Physics Letters **66**, 1249 (1995).

[Lev69] P. M. Levy. *Anisotropy in Two-Center Exchange Interactions*. Physical Review **177**, 509 (1969).

[Loh65] E. Loh. *$^1S_0$ Level of Pr^{3+} in Crystals of Fluorides*. Phys. Rev. **140** (5A), A1463 (1965).

[Lup00] V. Lupei and A. Lupei. *Emission dynamics of the $4F_{3/2}$ level of Nd^{3+} in YAG at low pump intensities*. Physical Review B **61**, 8087 (2000).

[Mai60] T. Maiman. *Stimulated optical radiation in ruby*. Nature **27**, 2319 (1960).

[Mal93] M. Malinowski, P. Szczepanski, W. Wolski and Z. Frukacz. *Inhomogeneity studies of Pr^{3+}-doped yttrium aluminium garnet using time-resolved spectroscopy*. J. Phys: Condensed Matter **5** (1993).

[Mes90] A. Messiah. *Quantenmechanik*, Volume 2 (Verlag de Gruyter, 1990), 3 edition.

[Mil81] D. C. Miller and T. L. Pernell. *The temperature distribution in a simulated garnet Czochralski melt*. Journal of Crystal Growth **53**, 523 (1981).

[Mil82] D. C. Miller and T. L. Pernell. *Fluid flow patterns in a simulated garnet melt*. Journal of Crystal Growth **58**, 253 (1982).

[Mir96] V. S. Mironov. *Superexchange interaction between lanthanide f^1 ions. Spin-Hamiltonian calculations for the 90° and 180° f^1-f^1 superexchange*. Journal of Physics: Condensed Matter **8**, 10551 (1996).

[MK85] T. Mayer-Kuckuk. *Atomphysik* (B. G. Teubner, 1985), 3 edition.

[Moo60] H. W. Moos. *Spectroscopic relaxation processes of rare earth ions in crystals*. Journal of Luminescence **1, 2**, 106 (1960).

[Mor65] A. H. Morrish. *The Physical Principles of Magnetism* (John Wiley & Sons Inc., 1965).

[Mor82] C. A. Morrison and R. P. Leavitt. *Spectroscopic properties of triply ionized Lanthanides in transparent host crystals*, chapter 46 (1982). In: K. A. Gschneidner, Handbook on the Physics and Chemistry of Rare Earth.

[Mue02] M. Mueller, N. Linder, C. Karnutsch, W. Schmid, K. P. Streubel, J. Luft, S. Beyertt, A. Giesen and G. H. Doehler. *Optically pumped semiconductor thin-disk laser with external cavity operating at 660 nm*. In: *Proceedings of SPIE*, Volume 4649, 265 – 271 (2002).

[Nag01] S. Nagahama, N. Iwasa, M. Senoh, T. Matsushita, Y. Sugimoto, H. Kiyoku, T. Kozaki, M. Sano, H. Matsumura, H. Umemoto, K. Chocho, T. Yanamoto and T. Mukai. *GaN-Based Light-Emitting Diodes and Laser Diodes, and Their Recent Progress*. physica status solidi (a) **188**, 1 (2001).

[Nak97] S. Nakamura and G. Fasol. *The blue laser diode* (Springer Verlag, 1997).

[Nak99] S. Nakamura, M. Senoh, I. S. Nagahama, T. Matsushita, H. Kiyoku, Y. Sugimoto, T. Kozaki, H. Umemoto, M. Sano and T. Mukai. *Violet InGaN/GaN/AlGaN-Based Laser Diodes Operable at 50 Degrees C with a Fundamental Transverse Mode*. Japanese Journal of Applied Physics **38**, L226 (1999).

[Nam97] O. H. Nam, M. D. Bremser, T. S. Zheleva and R. F. Davis. *Lateral epitaxy of low defect density GaN layers via organometallic vapor phase epitaxy*. Applied Physics Letters **71**, 2638 (1997).

[Nic01] S. Nicolas, E. Descroix, Y. Guyot, M.-F. Joubert, R. Y. Abdulsabirov, S. L. Korableva, A. K. Naumov and V. V. Semashko. *$4f^2$ to $4f5d$ excited state absorption in Pr^{3+}-doped crystals*. Optical Materials **16**, 233 (2001).

[Ofe62] G. S. Ofelt. *Intensities of crystal spectra of rare-earth-ions*. Journal of Chemical Physics **37**, 511 (1962).

[Osi03a] E. Osiac. *Energy transfer upconversion and avalanche mechanisms in systems doped with Ho^{3+}, Pr^{3+} and Yb^{3+} ions* (Shaker Verlag, Aachen, 2003). Dissertation.

[Osi03b] E. Osiac, E. Heumann, S. K. G. Huber, E. Sani, A. Toncelli and M. Tonelli. *Orange and red upconversion laser pumped by an avalanche mechanism in Pr^{3+}, Yb^{3+}:BaY_2F_8*. Applied Physics Letters **82** (22), 3832 (2003).

[Osi04] E. Osiac, E. Heumann, A. Richter, G. Huber, A. Diening and W. Seelert. *Red Pr^{3+}:$YLiF_4$ laser excited by 480 nm optically pumped semiconductor laser*. In: *CLEO 2004, Technical Digest* (2004).

[Ost07a] V. Ostroumov, W. Seelert, L. Hunziker and C. Ihli. *522/261 nm cw generation of Pr:YLF laser pumped by OPS laser*. Proceedings of SPIE **6451**, 645104 (2007).

[Ost07b] V. Ostroumov, W. Seelert, L. Hunziker, C. Ihli, A. Richter, E. Heumann and G. Huber. *UV generation by intracavity frequency doubling of an OPS-pumped Pr:YLF laser with 500 mW of cw power at 360 nm*. Proceedings of SPIE **6451**, 645103 (2007).

[Pam75] B. R. Pamplin (editor). *Crystal Growth*, chapter 6 (Pergamon Press, Oxford, 1975). P. 144.

[Par03] S. H. Park, J. Kim, H. Jeon, T. Sakong, S. N. Lee, S. Chae, Y. Park, C. H. Jeong, G. Y. Yeom and Y. H. Cho. *Evidence of higher-order mechanisms than dipole-dipole interaction in Tm^{3+} Tm^{3+} energy transfer in fluoroindogallate glasses*. Applied Physics Letters **83**, 2121 (2003).

[Pie74] J. W. Pierce and H. Y.-P. Hong. *Structural studies in the system potassium fluoride - yttrium trifluoride*. Materials Research Bulletin **9** (1974).

[Ray63] D. K. Ray. *Investigations into the Origin of the Crystalline Electric Field Effects on Rare Earth Ions: II. Contributions from the Rare Earth Orbitals*. Proceedings of the Physical Society **82**, 47 (1963).

[Ric04a] A. Richter. *Direktes Pumpen von Pr^{3+}:$LiYF_4$-Lasern auf der Basis von Halbleiterlasern* (Universität Hamburg, 2004). Diplomarbeit.

[Ric04b] A. Richter, E. Heumann, E. Osiac and G. Huber. *Diode pumping of a continuous-wave Pr^{3+}-doped $LiYF_4$ laser*. Optics Letters **29** (22), 2638 (2004).

[Ric07] A. Richter, E. Heumann, G. Huber, V. Ostroumov and W. Seelert. *Power scaling of semiconductor laser pumped Praseodymium-lasers*. Optics Express **15**, 5172 (2007).

[Ris68] L. A. Riseberg and H. W. Moos. *Multiphonon orbit-lattice relaxation of excited states of rare earth ions in crystals*. Physical Review **174** (2), 429 (1968).

[Ris88] H. Risk. *Modeling of longitudinally pumped solid-state lasers exhibiting reabsorption losses*. Journal of the Optical Society of America B **5**, 1412 (1988).

[Rua95] S. Ruan, J. M. Sutherland, P. M. W. French, J. R. Taylor and B. H. T. Chai. *Kerr-Lens mode-locked visible transitions of a Pr:YLF laser*. Optics Letters **20**, 1041 (1995).

[Rut53] J. W. Rutter and B. Chalmers. *A prismatic substructure formed during solidification of metals*. Canadian Journal of Physics **31** (1953).

[San94a] T. Sandrock. *Spektroskopie und Lasereigenschaften Pr^{3+}-dotierter Fluoride* (Universität Hamburg, 1994). Diplomarbeit.

[San94b] T. Sandrock, T. Danger, E. Heumann, G. Huber and B. H. T. Chai. *Efficient Continuous Wave-laser emission of Pr^{3+}-doped fluorides at room temperature*. Applied Physics B **58** (1994).

[Sar94] E. Sarantopoulou, A. C. Cefalas, M. A. Dubinskii, C. A. Nicolaides, R. Y. Abdulsabirov, S. L. Korableva, A. K. Naumov and V. V. Semashko. *VUV and UV fluorescence and absorption studies of Pr^{3+}-doped $LiLuF_4$ single crystals*. Optics Letters **19**, 499 (1994).

[Sch02] H. Scheife. *Faseroptischer Verstärker in Selten-Erd-dotiertem Fluoridglas für den sichtbaren Spektralbereich* (Shaker Verlag, 2002). Dissertation.

[Sie86] A. E. Siegmann. *Lasers* (University Science Books, Mill Valley, California, 1986).

[Sil97] F. R. G. de Silva and O. L. Malta. *Calculation of the ligand-lanthanide ion energy transfer rate in coordination compounds: contributions of exchange interactions*. Journal of Alloys and Compounds **250**, 427 (1997).

[Sob82] B. P. Sobolev and N. L. Tkachenko. *Phase diagrams of BaF_2-(Y, Ln)F_3 systems*. J. Less-Common Met. **85** (1982).

[Sou02a] D. F. de Sousa, R. Lebullenger, A. C. Hernandes and L. A. O. Nunes. *Evidence of higher-order mechanisms than dipole-dipole interaction in Tm^{3+} Tm^{3+} energy transfer in fluoroindogallate glasses*. Physical Review B **65**, 094204 (2002).

[Sou02b] D. F. de Sousa and L. A. O. Nunes. *Microscopic and macroscopic parameters of energy transfer between Tm^{3+} ions in fluoroindogallate glasses*. Physical Review B **66**, 024207 (2002).

[Ste66] R. M. Sternheimer. *Shielding and Antishielding Effects for Various Ions and Atomic Systems*. Physical Review **146** (1), 140 (1966).

[Sut96] R. L. Sutherland. *Handbook of nonlinear optics* (Marcel Dekker Inc., 1996).

[Sve88] E. B. Sveshnikova, A. A. Stroganov and N. T. Timofeev. *Role of quasilocalizable vibrations in the deactivation of rare-earth ions in fluoride bases*. Optics and Spectroscopy **64**, 73 (1988).

[Sve89] O. Svelto. *Principles of Lasers* (Plenum Press, 1989), 3 edition.

[Tho61] R. E. Thoma, C. F. Weaver, H. A. Friedman, H. Insley, L. A. Harris and H. A. Y. jr. *Phase equilibria in the system LiF-YF_3*. Journal of Physical Chemistry **65** (1961).

[Ton96] Y. P. Tong, J. M. Sutherland, P. M. W. French, J. R. Taylor, A. V. Shestakov and B. H. T. Chai. *Self-starting Kerr-lens mode-locked femtosecond Cr^{4+}:YAG and picosecond Pr^{3+}:YLF solid-state lasers*. Optics Letters **21**, 644 (1996).

[Ton99] A. Toncelli, M. Tonelli, A. Cassanho and H. P. Jenssen. *Spectroscopy and dynamic measurements of a Tm,Dy:BaY_2F_8 crystal*. Journal of Luminescence **82** (1999).

[Usu97] A. Usui, H. Sunakawa, A. Sakai and A. A. Yamaguchi. *Thick GaN Epitaxial Growth with Low Dislocation Density by Hydride Vapor Phase Epitaxy*. Japanese Journal of Applied Physics **36**, L899 (1997).

[Vor76] Y. K. Voron'ko, T. G. Mamedov, V. V. Osiko, A. M. Prokhorov, V. P. Sakun and I. A. Shcherbakov. *Nature of nonradiative excitation-energy relaxation in condensed media with high activator concentrations*. Sovjet Physics JETP **44** (2), 251 (1976).

[Vor82] Y. K. Voron'ko, V. V. Osiko and I. A. Shcherbakov. *Luminescence of Laser Crystals*. Izvestiya Akademii Nauk SSSR, Seriya Fizicheskaya **45** (5), 970 (1982).

[Wal98] B. M. Walsh, N. P. Barnes and B. D. Bartolo. *Branching ratios, cross sections, and radiative lifetimes of rare earth ions in solids. Application to Tm^{3+} and Ho^{3+} ions in $LiYF_4$*. Journal of Applied Physics **83** (5) (1998).

[Wat75] R. K. Watts. *Optical Properties of Ions in Solids* (Plenum Press, 1975).

[Web03] M. J. Weber. *Handbook of optical materials* (CRC Press, 2003).

[Wil88] K. T. Wilke and J. Bohm. *Kristallzüchtung* (VEB Deutscher Verlag der Wissenschaften, Berlin, 1988), 2 edition.

[Xio05] F.-B. Xiong, Z.-D. Luo and Y.-D. Huang. *Spectroscopic properties of Pr^{3+} in anisotropic $PbWO_4$ crystal*. Applied Physics B **80**, 321 (2005).

[Yar62] A. Yariv, S. P. S. Porto and K. Nassau. *Optical maser emission from trivalent praseodymium in calcium tungstate*. Journal of Applied Physics **38** (8), 2519 (1962).

[Yok67] M. Yokota and O. Tanimoto. *Effects of diffusion on energy transfer by resonance*. Journal of the Physical Society of Japan **22** (1967).

[Zha94] X. X. Zhang, A. Schulte, B. H. T. Chai, H. Weidner, R. I. Ramotar and R. E. Peale. *Raman spectroscopic evidence for isomorphous structure of $GdLiF_4$ and $YLiF_4$ laser crystals*. Solid State Communications **89** (2), 181 (1994).

6 List of Publications

Journal Publications

1. A. Richter, E. Heumann, E. Osiac, G. Huber, W. Seelert, and A. Diening, *"Diode pumping of a continuous wave Pr^{3+} doped $LiYF_4$ laser"*, Optics Letters, **29** (22), pp. 2638-2640 (2004)

2. A. Richter, H. Scheife, E. Heumann, G. Huber, W. Seelert, and A. Diening, *"Semiconductor laser pumping of a continuous-wave Pr^{3+}-doped ZBLAN fibre laser"*, Electronics Letters **41** (14), pp. 794-795 (2005)

3. A. Richter, N. Pavel, E. Heumann, G. Huber, D. Parisi, A. Toncelli, M. Tonelli, A. Diening, and W. Seelert, *"Continuous-wave ultraviolet generation at 320 nm by intracavity frequency doubling of red-emitting Praseodymium lasers"*, Optics Express **14** (8), pp. 3282-3287 (2006)

4. F. Cornacchia, A. Richter, E. Heumann, G. Huber, D. Parisi, and M. Tonelli, *"Visible laser emission of solid state pumped $LiLuF_4$:Pr^{3+}"*, Optics Express **15** (6), pp. 992-1002 (2007)

5. A. Richter, E. Heumann, G. Huber, V. Ostroumov, and W. Seelert, *"Power scaling of semiconductor laser pumped Praseodymium-lasers"*, Optics Express **15** (8), pp. 5172-5178 (2007)

International Conference Contributions

1. E. Osiac, E. Heumann, A. Richter, G. Huber, W. Seelert, and A. Diening, *"Red Pr^{3+}:$LiYF_4$ laser excited by 480 nm optically pumped semiconductor laser"*, CLEO/IQEC 2004, Talk CFE2, (San Francisco, 2004)

2. A. Richter, E. Heumann, E. Osiac, G. Huber, W. Seelert, and A. Diening, *"Direct diode pumping of a continuous wave Pr^{3+} doped YLF laser"*, EPS/QEOD Europhoton Conference 2004, Talk PD1, (Lausanne, 2004)

3. H. Scheife, A. Richter, E. Heumann, and G. Huber, *"Praseodymium-Doped Solid-State Lasers in the Visible Spectral Range"*, ICONO/LAT 2005, Invited Talk, (St. Petersburg, 2005)

4. S. Kück, A. Richter, Y. Kuzminykh, I. Sokolska, and E. Osiac, *"Quantum Efficiency of the Cascade Emission Process in Pr^{3+} Doped YF_3"*, CLEO/IQEC 2005, Talk CMR1, (Baltimore, 2005)

5. A. Richter, E. Osiac, H. Scheife, E. Heumann, G. Huber, W. Seelert, and A. Diening, *"Semiconductor Laser Pumping of a Continuous-Wave Pr^{3+}:$LiYF_4$ Laser Emitting at Several Wavelengths"*, CLEO/IQEC 2005, Talk CMAA4, (Baltimore, 2005)
6. A. Richter, H. Scheife, E. Heumann, G. Huber, W. Seelert, and A. Diening, *"Resonant pumping of praseodymium-doped crystals and fibres by semiconductor lasers"*, CLEO/EQEC Europe 2005, Talk CA8-4-TUE, (München, 2005)
7. A. Richter, H. Scheife, E. Heumann, and G. Huber, *"Praseodymium-doped solid-state lasers in the visible spectral region with direct semiconductor laser pumping"*, RGLS 2005 Technical Digest "Russian-German Laser Symposium", Editors S. Bagayev, G. Leuchs, E. Khazanov, Nizhny Novgorod, Russian Academy of Sciences **38** (2005)
8. A. Richter, E. Heumann, N. Pavel, and G. Huber, *"Ultraviolet generation by intracavity frequency doubling of a Pr^{3+}:$LiYF_4$ laser operating at 640 nm"*, CLEO/IQEC 2006, Talk CFB1, (Long Beach, 2006)
9. E. Heumann, A. Richter, and G. Huber, *"Semiconductor laser pumped Pr-doped solid state lasers and their frequency doubling"*, Conference on Laser Optics 2006, (St. Petersburg, 2006)
10. A. Richter, E. Heumann, N. Pavel, G. Huber, D. Parisi, A. Toncelli, A. Diening, and W. Seelert, *"Intracavity frequency-doubling of praseodymium lasers emitting at 640 nm and 320 nm in continuous wave and Q-switched mode"*, EPS/QEOD Europhoton Conference 2006, Talk WeE2, (Pisa, 2006)
11. G. Huber, A. Richter, and E. Heumann, *"Continuous wave Praseodymium solid-state lasers"*, Photonics West 2007, Talk 6451-01 (invited), (San Jose 2007)
12. V. Ostroumov, W. Seelert, L. Hunziker, C. Ihli, A. Richter, E. Heumann, G. Huber, *"UV generation by intracavity frequency doubling of an OPS-pumped Pr:YLF laser with 500 mW of cw power at 360 nm"*, Photonics West 2007, Talk 6451-02, (San Jose 2007)
13. A. Richter, E. Heumann, G. Huber, V. Ostroumov, and W. Seelert, *"Powerful Pr^{3+}:$LiLuF_4$ Lasers in the Visible and UV Spectral Range"*, CLEO/IQEC2007, Talk CTuD3, (Baltimore, 2007)
14. A. Richter, V. Ostroumov, E. Heumann, W. Seelert, and G. Huber, *"Frequency doubling of visible Pr-laser radiation in continuous wave and pulsed mode"*, CLEO/ EQEC Europe 2007, Poster CA-36-MON, (München, 2007)
15. G. Huber, A. Richter, K. Petermann, and E. Heumann, *"Growth, spectroscopy and lasing of Pr-doped materials"*, ICCG 2007, Invited Talk, (Salt Lake City, 2007)
16. A. Richter, E. Heumann, G. Huber, D. Parisi, A. Toncelli, and M. Tonelli, *"Power scaling of GaN laser diode pumped Pr-lasers"*, ASSP 2008, Talk MB2, (Nara, 2008)
17. A. Richter, E. Heumann, G. Huber, D. Parisi, A. Toncelli, and M. Tonelli, *"Low temperature measurements and laser performance of Pr^{3+}-doped fluoridic laser crys-*

tals under diode laser pumping", Russian-German Laser Symposium 2008, Poster PS-3, (Lübeck, 2008)

National Conference Contributions

1. A. Richter, E. Osiac, E. Heumann, and G. Huber, *"Pr^{3+}:$LiYF_4$-Laser bei 639,5 nm angeregt durch eine optisch gepumpte Laserdiode"*, Poster, 14. Norddeutscher Lasertag (Braunschweig, 2003)
2. A. Richter, E. Osiac, E. Heumann, and G. Huber, *"OPS-gepumpter Pr:YLF-Laser"*, DPG-Frühjahrstagung 2004, Talk Q4.6, (München, 2004)
3. A. Richter, E. Osiac, E. Heumann, and G. Huber, *"Halbleiterlaser–gepumpte Praseodym–dotierte Festkörperlaser im sichtbaren Spektralbereich"*, Poster, 15. Norddeutscher Lasertag (Hamburg, 2004)
4. A. Richter, E. Heumann, and G. Huber, *"OPS-gepumpter Praseodym-Faserlaser"*, DPG-Frühjahrstagung 2005, Talk Q56.7, (Berlin, 2005)
5. A. Richter, E. Heumann, and G. Huber, *"Resonatorinterne Frequenzverdopplung von Dauerstrich-Pr:$LiYF_4$-Lasern"*, DPG-Frühjahrstagung 2006, Talk Q11.6, (Frankfurt, 2006)
6. C. Braun, A. Richter, E. Heumann, and G. Huber, *"Spektroskopische Untersuchungen und erste Lasertätigkeit von Pr^{3+}:KY_3F_{10}"*, DPG-Frühjahrstagung 2007, Talk Q3.3, (Düsseldorf, 2007)
7. N.-O. Hansen, A. Richter, N. Thilmann, E. Heumann, and G. Huber, *"Resonatorinterne Frequenzverdopplung von GaN-laserdiodengepumpten cw-Pr:$LiLuF_4$-Lasern"*, DPG-Frühjahrstagung 2008, Talk Q4.8, (Darmstadt, 2008)

7 Acknowledgments

This work was performed from 2005 to 2008 in the "Festkörperlaser" workgroup of Professor Dr. Günter Huber at the Institut für Laser-Physik at the Universität Hamburg. During these three years, I came into contact with several excellent scientists and teammates. Although I guess the list will not be complete, I want to thank the following persons for helping me with my work:

First of all, I would like to thank Prof. Dr. Günter Huber for the interesting research subject and the possibility to prepare my Ph.D. thesis in his workgroup as well as the fruitful suggestions and discussions related to my research subject.
Next, I like to thank Prof. Mauro Tonelli and Prof. Dr. Klaus Sengstock for taking over the evaluation of my Ph.D. thesis and the oral defence of my thesis.
My gratitude is among Prof. Dr. Ernst Heumann and Dr. Klaus Petermann for their interesting laser- and crystal growth-related discussions and their expertise in optimization of optical cavities.
I also want to thank the whole workgroup "Festkörperlaser" for the extraordinary work atmosphere during these three years. I enjoyed working at the institute very much.
A big "thank you" goes to the technical and administrative staff of the workgroup: Without the help of Friedjof Tellkamp, Robert Fischer, Stefan Garbers, and Silke Frömmig several electronical, mechanical and administrative challenges would not have been solved in a convenient way.
I also want to thank my colleagues Sebastian Bär, Karsten Scholle, Lutz Rabisch, Henning Kühn, Jörg Siebenmorgen, and Nils-Owe Hansen for the interesting work and non-work related discussions and the good atmosphere in our office.
Special thanks go to my diploma students Christina Braun, Malte Posewang, and Nicky Thilmann as well as the staff members Dr. Nicolaie Pavel, Nils-Owe Hansen, and Matthias Fechner for performing additional experiments and helpful suggestions.
Big thanks goes to my proofreaders Teoman Gün, Dr. Sebastian Bär, Dr. Klaus Petermann, Dr. Eugen Osiac, Dr. Nicolaie Pavel, and Prof. Dr. Ernst Heumann for their excellent suggestions improving several aspects of this work.
Another very important "Thank you!" goes to the staff from Coherent in Lübeck, especially Dr. Vasiliy Ostroumov and Dr. Wolf Seelert for the opportunity to perform the high power laser experiments and their help in laser-related questions. I really appreciated working in Lübeck several times during my time as a Ph.D student.
Next, I want to thank the staff members of the workgroups of Prof. Mauro Tonelli and Prof. Alberto di Lieto from the University of Pisa, especially Dr. Francesco Cornacchia,

Dr. Alessandra Toncelli, and Dr. Daniela Parisi for supplying me with fluoride single crystals, fruitful discussions and helpful knowledge in the field of crystal growth and spectroscopy.
With the help of Sabine Kölling from the Technische Universität Hamburg-Harburg and Dr. Rainer Bertram from the Institut für Kristallzüchtung in Berlin the dopant concentration inside the investigated samples could be determined accurately. Thank you very much!
Last but not least I would like to thank my family and my friends for supporting me during the last years.